Study on aggregation states and physical properties of bioinert poly(2-oxazoline)-based alloy interfaces

洪, 振赫

Study on aggregation states and physical properties of bioinert poly(2-oxazoline)-based alloy interfaces

Tanaka Laboratory, Department of Materials Physics and Chemistry, Graduate School of Engineering

HONG JINHYEOK

Contents

Chapter 6. Conclusions

Chapter 1. Introduction

1.1. Background

1.1.1 Biomedical application of polymeric materials

With the trend of increased human life, disease, accident, etc. in the modern society, the human body rehabilitation business is now becoming an essential field of our lives. Following the changes, the demand for the rehabilitation/biomedical devices has gradually increased. On the other hand, supply through organ transplantation, which is a conventional rehabilitation method, has not been able to keep up with increasing demand. Accordingly, interest and use for the artificial organs and bio-scaffolds continues to increase. In reality, markets for the biomedical devices, such as artificial organs, bio-scaffolds, have rapidly increased at an annual average of 10 % as shown in the below graph. Among the prospect, if it is limited to a polymeric material, the market volume for the polymeric biomaterials is anticipated from 1.3 billion in 2018 to 39.1 billion dollars in 2024, which annual growth average is 20 %. This outlook is expected to show significant growth compared to that of another major material, metal/ceramic biomaterials of around 10 %.[1-1,2)]

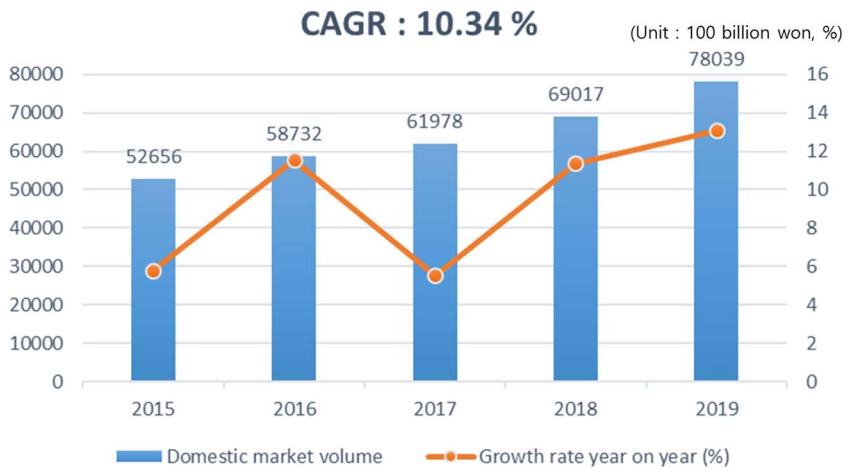

Fig. 1-1. Current status of the market volume and growth rate for the medical devices domestic in Korea (2015-2019) [1-1)]

Since poly(methyl methacrylate) (PMMA) firstly used as a substitute for human tissues in 1940s, polymer materials have been receiving great demands for the various biomedical application, such as artificial organ, bio-adhesive, scaffolds, etc.[1-3)] While metal or ceramic materials are generally applied to specific parts which are required to outstanding mechanical properties like artificial bones/joints and implant, polymeric materials have some advantages of light weight, excellent processability, and introducing functionality, such as like adhesive properties, so they used as composite with the above metal/ceramic materials, or has more diversely applied to our bodies such as bio-adhesive, biodegradation, and drug delivery. Table 1-1 summarizes various practical applications of the polymeric materials to biomedical devices.[1-4)]

Table 1-1. Representative synthetic polymers and their biomedical applications.[1-3~7)]

Synthetic polymers	Application
Poly(olefin) (PE, PP)	Hip arthroplasty, artificial joint
Poly(tetrafluoroethylene) (PTFE)	Artificial vessal
Poly(methyl methacrylate) (PMMA)	Intraocular lens
Poly(siloxane)	Intra-articular implant
Poly(amide)	Dialysis membrane
Poly(ester)	Biodegradable suture

1.1.2. Biocompatible polymers

The aforementioned properties of polymers such as light weight, processability, adhesion, and biodegradability are advantages in the use of biomedical application. However, the most important one among the properties is the biocompatibility.[1-3] The biocompatible properties are the crucial importance to sustain safety and efficacy of the biomedical devices.

Fouling is a phenomenon which unwanted substance such as in/organic materials to surfaces by a certain attraction and then impair their functions. Especially the term of biofouling refers to the interfacial phenomenon that encompasses the accumulation against the surfaces from biological systems (e.g. blood, cell, or protein). Once the biomedical devices are fouled with unspecific components of near cells or protein, it leads to lose the initial functionality and causes serious disease. To solve the problem, the ingredients of the devices could be replaced by biocompatible structure, but more efficient methods is to tune the surfaces into feature of inhibiting biofouling.

Surface coating with biocompatible polymers is an effective method to accomplish surface bio-antifouling properties. For decades of effort to enhance the bio-antifouling properties using diverse polymeric structure, it has been revealed that there are 3 distinct structural characteristics of the polymer components showing outstanding antifouling properties; [1-8~11]

1. Hydrophilic polymer structure
2. Hydrogen bonding acceptor, not donor
3. No net charge

These structural characteristics are called Whitesides' rules, which pursue the relationship of structure-protein resistance properties. [1-8, 9] Fig. 1-2 shows representative antifouling polymer structures, which meet the described rules.

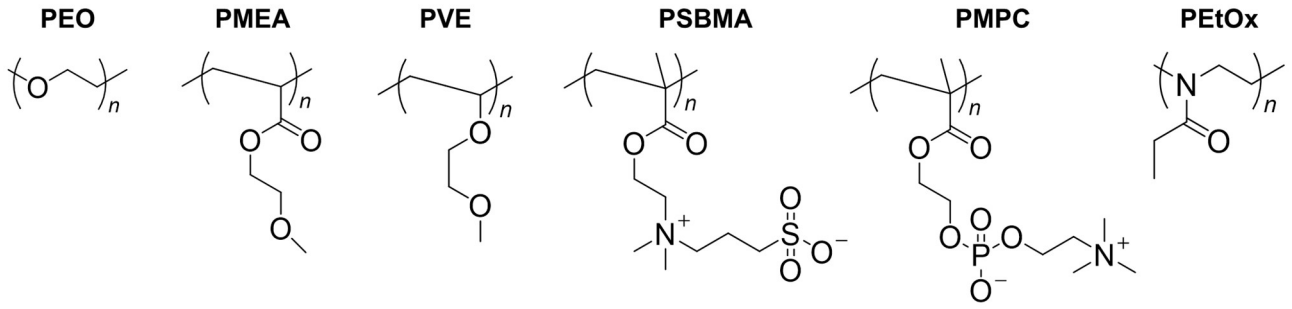

Fig. 1-2. Representative polymers showing outstanding antifouling properties.; PEO : poly(ethylene oxide)[1-12~15)] PMEA : poly(2-methoxyethyl acrylate);[1-16,17)] PVE : poly(vinyl ether);[1-18,19)] PSBMA : poly(2-sulfobetaine methacrylate);[1-20)] PMPC : poly((2-(methacryloyloxy) ethyl) phosphorylcoline);[1-20)] PEtOx : poly(2-ethyl-2-oxazoline).[1-13,21~23)]

1.1.2.1. Poly(ethylene oxide) (PEO)

PEO is a representative bio antifouling polymer structure that has been widely used not only in academia but also in industry for several decades, as it called a gold standard material for bio-application.[1-12~15)] PEO is composed of hydrophilic ethylene oxide chain, and it also have hydrogen bonding acceptor, which is easy to from hydrogen bonding with water. That is, the structure can cause strong hydration behavior when in contact with water. Also, it is known that the strong hydration behavior and its excellent chain flexibility are good at preventing adhesion of the bioorganic due to exclusion volume effects.[1-12,15)] In addition, the PEO chain has excellent solubility in most organic solvents, so it has excellent industrial value as it can be applied to various reactions and processing. Accordingly, numerous methods have been reported to modify the device surfaces through the chemical fixation at some media which called PEGylation[1-24,25)] or physical adsorption.[1-26,27)]

Recently, however, there have been appeared some reports about two drawbacks of PEO *in vivo* with mid-term or long-term usage. One is antibody formation surrounding the structure,[1-28,29)]. In an instance, G. Garratty *et al.* reports that anti-poly(ethylene glycol) (PEG) were detected in the blood of 9 out of 15 people who were treated with PEG-conjugation drugs, and the immune responses resulted in the clearance of the PEG-conjugation. And, they also reveal that the anti-PEG response has been founded in 20 ~ 25 % of healthy blood. The other drawback is oxidative degradation of the polymer chain.[1-30,31)]

S. Han *et al.* shows that PEO easily reacted with oxygen and formed PEO peroxide, which finally makes the PEO backbone decomposed by chain scission process.[1-31] As described, disadvantages of long term use of the PEO such as the interference of the immune response and decomposition reaction in bio environment make it difficult to maintain the sustainable biocompatibility of the PEO, which suggests the alternative biocompatible materials is start to be required.

1.1.2.2. Poly(2-oxazoline) (POx)

POxs are the structures in which tertiary amide groups are continuously linked and classified as pseudo-peptides because of their structural similarity with the natural peptides.[1-13] So far, it has been revealed that the POxs have several advantages of stabilities in bio environments. First, because of their peptide-like structures, the immune responses are well suppressed *in vivo*.[1-28] Second, main chain of the POxs is consisted of an ethylene linkage with a heteroatom like PEO. Difference is the heteroatom in its main chain is nitrogen, relatively non-polar than oxygen atom. This chemical composition of the main chain leads stabilities against oxidative degradation than main chain of PEO. [1-13] Considering current situation that stability problems of PEO have been emerged, the POxs have newly been to get attention as a promising type of the biocompatible materials.

Despite several advantages described above, POxs were hard to be used in industry because there were technical problems in synthesis. From the 1960s, it became possible to synthesize POx by cationic polymerization, however, it was difficult to apply widely to industry because of requirement for long time for the synthesis, and limited kinds of monomers.[1-32,33] In last two decades, on the other hand, driven by continuous development of the controlled polymerization methods such as usage of microwave reactors, POxs now can be rapidly obtained with narrow molecular weight distribution and it also became possible to fine-tune the primary structure using various types of oxazoline monomers, initiators, and terminators.[1-13,34] Fig. 1-3 shows typical alkyl substituted POx structures and a trends of their water soluble and thermos-responsive properties. In the series of the alky substituted POx structures, especially,

POxs with methyl and ethyl side chain are well known to have good affinities with water molecules.[1-34,35] From the high water soluble properties, many researchers have continued their effort to construct antifouling surface using the POxs in order to apply the POxs as an alternative for the described synthetic antifouling polymers.[1-21~23] As results, for example, E. M. Benetti *et al.* prepared poly(2-methyl-2-oxazoline) (PMeOx), poly(2-ethyl-2-oxazoline) (PEtOx), and PEO brush and they reported that the PMeOx and PEtOx brush strongly restricted the protein adsorption in human serum, which are more powerful or comparable with the PEO brush.[1-35]

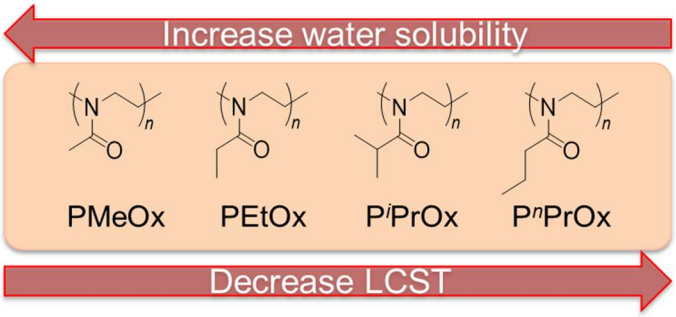

Fig. 1-3. Tendency of the water solubility and lower critical solution temperature (LCST) of a series of alkyl substituted POxs.[1-13] P^{i}PrOx : poly(2-isopropyl-2-oxazoline), P^{n}PrOx : poly(2-normalpropyl-2-oxazoline).

1.1.3. Aggregation states and physical properties of polymers at surfaces

Polymer interface is boundary between two different phases such as gas-polymer, liquid-polymer, and solid-polymer. At the interface, typically, various physical properties appear differently from those of bulk due to the influence of the properties of molecules on both sides and the interstitial force between them. In some previous studies conducted in 1990s, K. Tanaka *et al.* demonstrated that the glass transition temperature (T_g) and storage modulus of the monodisperse polystyrene (PS) at the polymer/air interface were reduced comparing with that in bulk.[1-36,37] In addition, the phenomenon was explained by showing the different physical properties at the interface, and the differences were driven by the structural changes which were induced by localization of the chain-end groups at the polymer/air interfaces.[1-38,39] That is, the aggregation states of the polymers at the interface are different from that in

the bulk. Therefore, understanding the aggregation states at the interface are important factor to understand the physical properties at the polymer interface.

In order to express surface selective functionality, such as surfaced wettability, adhesion properties, biocompatibility, inducing the surface segregation behaviors are the effective method to construct the functional and thermodynamically stable surfaces. Since 1980s, surface aggregation states in multi-component systems (e.g. block copolymers / polymer blends) have been studied, and it has been found that a polymer component selectively aggregated at the surface in a direction of minimizing interfacial free energy.[1-40,41] Also, there are much efforts to control the surface aggregation states in terms of the polymer structure, and, several rules were identified.

First, polymer chain with lower surface free energy value are preferentially aggregated at the surface.[1-42~47] This was shown in a previous study as follows. S. A. Schwarz *et al.* prepared the blend film using non-labeled PS (hPS) and the deuterated PS (dPS) as model for homogeneous mixture. Even though the two components have small difference in surface free energy of 0.06 ~ 0.08 mJ, it has been found that dPS, having lower surface free energy, was concentrated at the surface region and gradually changed to bulk region.[1-42] As such the difference in surface free energy value is a driving force for the surface aggregation. In particular, fluoropolymers[1-44,45] and poly(siloxane)s[1-46,47] are the representative structure which have lower surface free energy. Therefore, as an effective strategy for surface aggregation, a method of introducing the following fluorine-based and siloxane-based structures is also widely used.[1-44~47]

Second is the effect of chain end groups. The chain end groups of the polymer are also known to localize at the stop surface if the surface free energy of the end groups is lower than that for main chain, whereas chain end groups with higher surface free energy hide inside its bulk region.[1-48,49] On the other hand, there are the cases that small molecular weight of polymer structures is preferentially aggregated at the surface region even though they have higher surface free energy value. These behaviors are explained by the entropic effects of the chain end groups.[1-50,51] In a previous study, K. Tanaka *et al.*

prepared poly(methyl methacrylate) (PMMA)/PS blend film with different number average molecular weight (M_n) of monodisperse PMMA in range of 1.2k to 387k whereas M_n of monodisperse PS was fixed by 1450k. Although the PMMAs having higher surface free energy than PS, smaller M_n of the PMMA under 144k were enriched at the surface in the mixture with the PS. Whereas PMMA 387k was depleted at the surface. The trend is explained by the entropic effects at the chain end. At the surface, molecular chain localized in a normal direction. And, the surface polymer structure was reorganized to minimize penalty in conformational entropy of the structure.[1-50)] Unlike the main chain, which connected in both direction, chain end groups are neighboring free volume. That is, the localization of the chain end at the surface can forms entropy stable surface rather than a case of main chain localized at the surface. Also, the number density of the chain-end increases with decreasing the M_n, then, small molecular weight of the polymer easily aggregated toward the surface to decrease the penalty of the conformational entropy.

1.1.4. Effect of polymer architectures on surface aggregation states

Many polymers having outstanding surface functionality like antifouling properties, such as PEO and PEtOx, usually have higher surface free energy than typical glassy polymers.[1-52,53)] Therefore, there are some demands to localize polymer having high surface free energy at the surface. A strategy for enriching the hydrophilic polymers at the surface is using branch type structure. Shortly, branch polymers preferentially aggregated at the surface comparing with the linear polymers by the entropic consideration.[1-19,54,55)] In a study, D. G. Walton *et al.* demonstrated the surface aggregation states of the linear PEO and branch type PEO-grafted copolymer in the mixture with PMMA. In the study, using neutron reflectivity (NR), it was revealed that the branch copolymer was aggregated at the outermost surface region after thermal annealing procedure while the linear PEO moved away from the surface region.[1-54)] This is explained by the influence of the entropy contribution of the structural feature that branched polymers have a higher proportion of chain end groups than linear polymers.

Fig. 1-4 shows schematic images for basic polymer structures of (a) linear polymers and (b) branch polymers, and a series of branch polymers: (c) hyperbranch polymers (HBP), (d) bottlebrush polymers (BBP). In recent years, there have been much efforts to improve the segregation of the surface of functional materials especially having high surface energy through designing branch polymer architectures such as hyper-branch polymers (HBP) and bottlebrush polymers (BBP). In the case of HBP, it has several structural features; Chain dimension of the structure is smaller comparing the same molecular weight of its linear structure. Also, the large number of chain-end groups at the HBP lead to surface segregation.[1-56,57)]

Another promising polymer architecture is bottlebrush structure. BBP, which is a class of a branch polymer, have densely connected polymeric side chain.[1-57,59)] The high density of side-chain lead to have large number of chain-end groups like HBP. Also, unlike strongly restricted its main chain, polymeric side chain is partially stretched and have enhanced flexibility than its linear structure.[1-59,60)] That is, by controlling the composition or length of the polymeric side chain, the entropic interaction with surrounding chains or interfaces are simply tuned. In a previous study, G. E. Stein *et al.* demonstrated the surface segregation of the various side chain length of bottlebrush PS in linear dPS matrix with fixed molecular weight, using secondary ion mass spectroscopy (SIMS) measurement. And, it was shown that bottlebrush PS strongly segregated at the surface if the number ratios of repeating units of the linear dPS and bottlebrush PS side chains were bigger than 8.[1-57)]

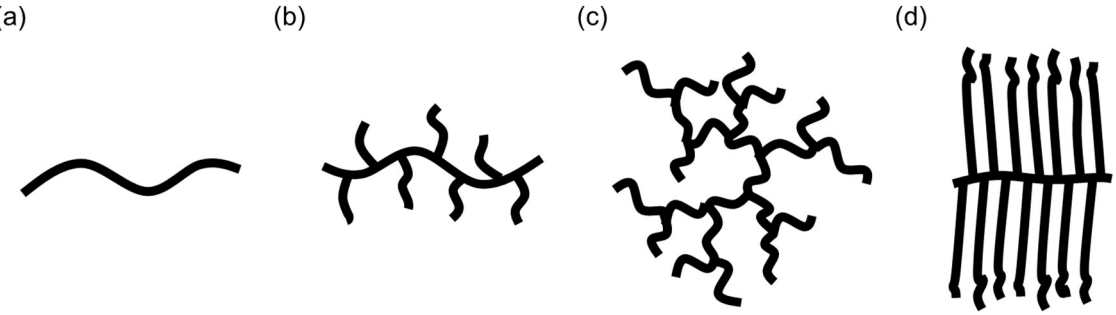

Fig. 1-4. Schematic illustration of the typical polymer structures of (a) linear polymer, (b) branch polymer, and the various structure form of the branch architecture of (c) hyperbranch polymer, and (d) bottlebrush polymer.

1.1.5. Aggregation states of polymers at water interface

Many of polymeric materials are widely used in aqueous environment for membrane, adhesive, and bio-medical devices. For such applications, the polymeric surfaces inevitably attached to water phase, that is, understanding of the interfacial aggregation states of the polymers at water interface are in a pivotal importance. In present, however, it is still hard to make clear answers from questions such as what polymer structure was formed at the water interface. This is because usual characterizations for the interfacial composition and aggregation states has been performed through surface-sensitive analysis using X-ray photoelectron spectroscopy (XPS),[1-61)] secondary-ion mass spectroscopy (SIMS),[1-62)] or scanning electron microscope (SEM),[1-63)] which are carried out under high vacuum condition. In particularly, such the characterizations have been mainly focused on the polymer/air interface. That is because, the surface aggregation states of the polymers tend to organize in the direction of forming low surface energy under vacuum condition, which is same as air interface.

Generally, polymeric materials tend to organize at the interface to minimize interfacial energy after contact with other media.[1-63,65)] Water molecules have high surface free energies of 72.8 $mN \cdot m^{-1}$,[1-66)] that is, polymer structures are reorganized at the surface after contacting with water, which are different under air and vacuum condition. The difference make difficulty to apply the surface sensitive analysis methods, which require the high vacuum, to deal the polymer/water interfaces. To overcome the difficulty, there are much effort to understand the surface aggregation states at the water interface. Such

an effort, A. Takahara *et al*. evaluated the surface aggregation states of the hydrated polymer by applying freeze drying methods to the XPS.[1-67)]

In recent years, development in analysis methods, such as sum frequency generation (SFG)[1-68~70)] and NR,[1-71)] have allowed the *in-situ* evaluation of the local conformation of polymer chains and its aggregation states in an aqueous condition. So far, K. Tanaka *et al.* have evaluated that local conformation of the PMMA chain at the water interface was changed by hydrogen bonding interaction between water molecules and the polymer segments using SFG.[1-68)] Also, it also has been demonstrated that the local conformations at the water interface changed by fine-tune of the polymer structure, such as molecular weight or side chain structure.[1-69,70)] For a large scale of the molecular aggregation states at water interface, it have become possible to be evaluated by NR measurement. For example, Tanaka et al. confirmed that water molecules penetrated from a PMMA film surface and the film surface was diffused as water molecules and was formed diffused layer coexisting the mater molecules with the polymer chains.[1-71)]

1.1.6. Physical properties of polymers at water interface

Understanding the physical properties of the polymer/water interface is one of the key factors for the surface functionalities. So far, it has been founded that the polymer chains such as PMMA dissolve in water in certain levels and form a diffuse layer when the polymer surface comes into contact with water. And, it also founded that physical properties of the diffused layer are different from the bulk state as acting the water molecules as a plasticizer in the diffused layer. In a previous study, K. Tanaka *et al.* evaluated thermal molecular motion of the PMMA chain at the water interface using lateral force microscopy (LFM). And, it is reported that T_g of PMMA in the depth of 4.5 nm from the water interface determined to be 294.5 K, whereas T_g in bulk region was around 383 K. And, it is explained by contents of the water molecules. If water contents increased, the relaxation temperature decreased and following the chain mobility was enhanced by water molecules.[1-72)] At the same time, mechanical properties also

revealed to decrease following the contents of the water molecules. [1-71,72)]

1.1.7. Relationship between the physical properties and the bio-inert functionality

The typical bio-inert polymers, represented by PEO, are known to strongly suppressed adsorption of proteins at the polymer/water interfaces. The outstanding bio-inert properties have been explained by exclusion volume effect, which acts as a repulsive force against the protein absorption, based on strong hydration of the chains, forming densely diffusion layers, and remarkable chain mobility.[1-12,73)] Therefore, understanding physical properties, such as chain mobility and mechanical properties, at the water interface is a crucial importance to effectively control the inhibition of the proteins at the polymer surfaces.[1-74,75)] In a previous report, K. Tanaka *et al.* prepared network structure consisting of poly(2-metoxyethyl vinyl ether) with different crosslinking density. Then, it is reported that the platelet adhesion was strongly suppressed at the softer and more diffused polymer interfaces even though all the network structures have almost identical aggregation states at water interfaces.[1-74)] The results denote the physical property at the water interface plays a key factor to manifest bio-inert properties.

1.2. Purpose of this study

Bio-inert polymers, such as PEO, PMEA, and poly(vinyl ether) (PVE) derivatives, are considered as a pivotal material for the efficacy and safety of the bio-application. And recently, the precise mechanisms about the excellent anti-biofouling properties of the bio-inert polymer structure have been revealed in terms of interfacial aggregation states and the physical properties in aqueous environments. However, nowadays, there have been reported that antibody response occurs against the synthetic polymers if the described synthetic polymers are used *in vivo* for the long-term periods. One of methods to overcome the disadvantage is to use protein-like structure. PEtOx is a kind of pseudo-peptide structure, and it have been attracted as a novel class of the bio-inert structure. However, even now, it is unclear why the PEtOx exhibit excellent bio-inert properties.

The purpose of this study is to understand aggregation behaviors of PEtOx and its physical properties at the water interface in terms of polymeric structure to enhance bio-inert properties. For the purpose, I proceeded my researches as follows.

- In chapter 2, well-defined structure of PEtOx derivatives, which are stable in water, plan to be synthesized by controlled polymerization.
- In chapter 3, aggregation behaviors of thin film of the poly(2-ethyl-2-oxazoline) derivative at the water interface are going to be understood and estimated the bio-inert properties.
- In chapter 4, the influence of the PEtOx structure factor to its aggregation behaviors is planned to be evaluated and surface functionality and physical properties were going to evaluate.
- In chapter 5, various film annealing processes are planned to be demonstrated to enhance the surface aggregation state of PEtOx and diffuse layer at the water interface.
- In chapter 6, results in each chapter and comprehensive conclusion will be summarized.

1.3. References

1-1) Korea Health Industry Development Institute (KHIDI), Current Status of the Domestic Medical Device Market Size (2015 ~ 2019)
https://www.khidi.or.kr/board?menuId=MENU01507&siteId=SITE00004

1-2) Korea Institute of Science and Technology (KIST), Efforts to Find Biocompatible Materials, Expanding the Biomaterials Market, Biomaterials Market, Markets and Markets (2019.06)
http://tepri.kist.re.kr/?p=3415

1-3) Kang, I. K.; Lee, J. H.; Park, K. D.; Kim, S. H.; Nah, J. W.; Han, D. K.; Noh, I. S. Present and Future of Biomedical Polymers. *Polym. Sci. Technol.*, **2016**, *27*, 544.

1-4) Jung, G. I.; Kim, J. S.; Choi, J. H.; Jun, J. H. The Trend and Prospect of Biomaterials in the Biomedical Engineering Field. *KIC news*, **2010**, *13*, 18.

1-5) Maitz, M. F. Applications of Synthetic Polymers in Clinical Medicine. *Biosurface and Biotribology*, **2015**, *1*, 161.

1-6) Teo, A. J. T.; Mishra, A.; Park, I. K.; Kim, Y. J.; Park, W. T.; Yoon, Y. J. Polymeric Biomaterials for Medical Implants and Devices. *ACS Biomater. Sci. Eng.*, **2016**, *2*, 454.

1-7) Pruitt, L.; Furmanski, J. Polymeric Biomaterials for Load-Bearing Medical Devices. *J. Min. Met. Mater. Soc.*, **2009**, *61*, 14.

1-8) Ostuni, E.; Chapman, R. G.; Holmlin, R. E.; Takayama, S.; Whitesides, G. M. A Survey of Structure-Property Relationships of Surfaces that Resist the Adsorption of Protein. *Langmuir*, **2001**, *17*, 5605.

1-9) Chapman, R. G.; Ostuni, E.; Takayama, S.; Holmlin, R. E.; Yan, L.; Whitesides, G. M. Surveying for Surfaces that Resist the Adsorption of Proteins. *J. Am. Chem. Soc.*, **2000**, *122*, 8303.

1-10) Banerjee, I.; Pangule, R. C.; Kane, R. S.; Antifouling Coatings: Recent Developments in the Design of Surfaces That Prevent Fouling by Proteins, Bacteria, and Marine Organisms. *Adv.*

Mater., **2011**, *23*, 690.

1-11) Nurioglu, A. G.; Esteves, A. C. C.; With, G. D. Non-Toxic, Non-Biocide-Release Antifouling Coating Based on Molecular Structure Design for Marine Applications. *J. Mater. Chem. B*, **2015**, *3*, 6547.

1-12) Lee, B. S. Anti-Biofouling Polyethylene Glycol-based Study and Its Industrial Application. *Polym. Sci. Technol.*, **2017**, *28*, 371.

1-13) Rosa, V. R. Poly(2-oxazoline)s as Materials for Biomedical Applications. *J. Mater. Sci. Mater. Med.*, **2014**, *25*, 1211.

1-14) Vermette, P.; Meagher, L. Interactions of Phospholipid- and Poly(ethylene glycol)-Modified Surfaces with Biological Systems: Relation to Physico-Chemical Properties and Mechanisms. *Colloids Surf. B*, **2003**, *28*, 153.

1-15) Knoll, D.; Hermans, J. Polymer-Protein Interactions. *J. Biol. Chem.*, **1982**, *258*, 5710.

1-16) Hirata, T.; Matsuno, H.; Kawaguchi, D.; Yamada, N. L.; Tanaka, M.; Tanaka, K. Construction of a Blood-Compatible Interface Based on Surface Segregation in a Polymer Blend. *Polymer*, **2015**, *78*, 219.

1-17) Jankova, K.; Javakhishvili, I.; Kobayashi, S.; Koguchi, R.; Murakami, D.; Sonoda, T.; Tanaka, M. Hydration States and Blood Compatibility of Hydrogen-Bonded Supramolecular Poly(2-Methoxyethyl acrylate). *ACS Appl. Bio Mater.*, **2019**, *2*, 4154.

1-18) Oda, Y.; Zhang, C.; Kawaguchi, D.; Matsuno, H.; Kanaoka, S.; Aoshima, S.; Tanaka, K. Design of Blood-Compatible Interfaces with Poly(vinyl ether)s. *Adv. Mater. Interface*, **2016**, *3*, 1600034.

1-19) Sugimoto, S.; Oda, Y.; Hirata, T.; Matsuyama, R.; Matsuno, H.; Tanaka, K. Surface Segregation of a Branched Polymer with Hydrophilic Poly[2-(2-ethoxy)ethoxyethyl vinyl ether] Side Chains. *Polym. Chem.*, **2017**, *8*, 505.

1-20) Inoue, Y.; Ishihara, K. Reduction of Protein Adsorption on Well-Characterized Polymer Brush Layers with Varying Chemical Structure. *Coll. Surf. B Biointerfaces*, **2010**, *81*, 350.

1-21) Tauhardt, L.; Kempe, K.; Gottschaldt, M.; Schubert, U. S. Poly(2-oxazoline) Functionalized Surfaces: from Modification to Application. *Chem. Soc. Rev.*, **2013**, *42*, 7998.

1-22) Ulbricht, J.; Jordan, R.; Luxenhofer, R. On the Biodegradability of Polyethylene Glycol, Polypeptoids and Poly(2-oxazoline)s. *Biomaterials*, **2014**, *35*, 4848.

1-23) Hong, J. H.; Totani, M.; Kawaguchi, D.; Masunaga, H.; Yamada, N. L.; Matsuno, H.; Tanaka, K. Design of a Bioinert Interface Using an Amphiphilic Block Copolymer Containing a Bottlebrush Unit of Oligo(oxazoline). *ACS Appl. Bio Mater.*, **2020**, *3*, 7363.

1-24) Chang, Y.; Shih, Y. J.; Ko, C. Y.; Jhong, J. F.; Liu, Y. L.; Wei, T. C. Hemocompatibility of Poly(vinylidene fluoride) Membrane Grafted with Network-Like and Brush-Like Antifouling Layer Controlled via Plasma-Induced Surface PEGylation. *Langmuir*, **2011**, *27*, 5445.

1-25) Chang, Y.; Ko, C. Y.; Shih, Y. J.; Quemener, D.; Deratani, A.; Wei, T. C.; Wang, D. M.; Lai, J. Y. Surface Grafting Control of PEGylated Poly(vinylidene fluoride) Antifouling Membrane via Surface-Initiated Radical Graft Copolymer. *J. Membr. Sci.*, **2009**, *345*, 160.

1-26) Kim, S.; Gim, T.; Kang, S. M. Versatile, Tannic Acid-Mediated Surface PEGylation for Marine Antifouling Applications. *ACS Appl. Mater. Interfaces*, **2015**, *7*, 6412.

1-27) Hirata, T.; Taneda, H.; Nishio, K.; Inutsuka, M.; Yamada, N. L.; Nemoto, F.; Minagawa, Y.; Matsuno, H.; Tanaka, K. A Facile Surface Functionalization Method for Polymers Using a Nonsolvent. *ACS Appl. Bio Mater.*, **2020**, *3(4)*, 2176.

1-28) Yang, W.; Liu, S.; Bai, T.; Keefe, A. J.; Zhang, L.; Ella-Menye, J. R.; Li, Y.; Jiang, S. Poly(carboxybetaine) Nanomaterials Enable Long Circulation and Prevent Polymer-Specific Antibody Production. *Nano today*, **2014**, *9*, 10.

1-29) Armstrong, J. K.; Hempel, G.; Koling, S.; Chan, L. S.; Fisher, T.; Meiselman, H. J.; Garratty, G. Antibody Against Poly(ethylene glycol) Adversely Affects PEG-Asparaginase Therapy in Acute Lymphoblastic Leukemia Patients. *Cancer*, **2007**, *110(1)*, 103.

1-30) Han, S.; Kim, C.; Kown, D. Thermal/Oxidative Degradation and Stabilization of Polyethylene

Glycol. *Polymer*, **1997**, *38(2)*, 317.

1-31) Tauhardt, L.; Kempe, K.; Gottschaldt, M.; Schubert, U. S. Poly(2-oxazoline) Functionalized Surfaces: from Modification to Application. *Chem. Soc. Rev.*, **2013**, *42*, 7998.

1-32) Kagiya, T.; Narisawa, S.; Maeda, T.; Fukui, K. Ring-Opening Polymerization of 2-Substituted 2-Oxazolines. *J. Polym. Sci., Part B: Polym. Lett.*, **1966**, *4*, 441.

1-33) Dargaville, R.T.; Lava, K.; Verbraeken, B.; Hoogenboom, R. Unexpected Switching of the Photogelation Chemistry When CrossLinking Poly(2-oxazoline) Copolymers. *Macromolecules*, **2016**, *49*, 4774.

1-34) Glassner, M.; Vergaelen, M.; Hoogenboom, R. Poly(2-oxazoline)s: A Comprehensive Overview of Polymer Structures and Their Physical Properties. *Polym. Int.*, **2018**, *67*, 32.

1-35) Morgese, G.; Gombert, Y.; Ramakrishna, S. N.; Benetti, E. M. Mixing Poly(ethylene glycol) and Poly(2-alkyl-2-oxazoline)s Enhances Hydration and Viscoelasticity of Polymer Brushes and Determines Their Nanotribological and Antifouling Properties. *ACS Appl. Mater. Interfaces*, **2018**, *10*, 41839.

1-36) Tanaka, K.; Taura, A.; Ge, S. R.; Takahara, A.; Kajiyama, T. Molecular Weight Dependence of Surface Dynamic Viscoelastic Properties for the Monodisperse Polystyrene Film. *Macromolecules*, **1996**, *29*, 3040.

1-37) Kajiyama, T.; Tanaka, K.; Takahara, A. Surface Molecular Motion of the Monodisperse Polystyrene Films. *Macromolecules*, **1997**, *30*, 280.

1-38) Mayes, A. M. Glass Transition of Amorphous Polymer Surfaces. *Macromolecules*, **1994**, *27*, 3114.

1-39) Kawaguchi, D.; Tanaka, K.; Takahara, A.; Tasaki, S.; Kajiyama, T. Surface Composition Control via Chain End Segregation in Blend Films of Polystyrene and Poly(vinyl methyl ether), *Macromolecules*, **2003**, *36*, 6824.

1-40) Mansky, P.; Russell, T. P.; Hawker, C. J.; Mays, J.; Cook, D. C.; Satija, S. K. Interfacial

Segregation in Disordered Block Copolymers: Effect of Tunable Surface Potentials. *Phys. Rev. Lett.*, **1997**, *79*, 237.

1-41) Koberstein, J. T. Molecular Design of Functional Polymer Surfaces. *J. Polym. Sci. Part B: Polym. Phys.*, **2004**, *42*, 2942.

1-42) Jones, R. A. L.; Kramer, E. J.; Rafailovich, M. H.; Sokolov, J.; Schwarz, S. A. Surface Enrichment in an Isotopic Polymer Blend. *Phys. Rev. Lett.*, **1989**, *62*, 280.

1-43) Compostto, R. J.; Stein, R. S.; Karmer, E. J.; Jones, R. A. L.; Mansour, A.; Karim, A.; Felcher, G. P. Surface Enrichent in Polymer Blends – A Neutron Reflection Test. *Phys. B Condens Matter*, **1989**, *156*, 434.

1-44) Takahara, A.; Higashi, N.; Kunitake, T., Kajiyama, T. State of Aggregation and Surface Chemical Composition of Composite Thin Films Composed of Poly(vinyl alcohol) and Fluorocarbon Amphiphile. *Macromolecules*, **1988**, *21*, 2443.

1-45) Hikita, M.; Tanaka, K.; Nakamura, T.; Kajiyama, T.; Takahara, A. Aggregation States and Surface Wettability in Films of Poly(styrene-*block*-2-perfluorooctyl ethyl acrylate) Diblock Copolymers Synthesized by Atom Transfer Radical Polymerization. *Langmuir*, **2004**, *20*, 5304.

1-46) Yamamoto, K.; Hirai, T.; Oda, Y.; Kawaguchi, D.; Matsuno, H.; Tanaka, K. A Polymer Interfacial Modifier Synthesized by Living Anionic Polymerization Incorporation of Inorganic Blocks to Chain Ends. *Macromol. Chem. Phys.*, **2017**, *218(12)*, 1600473.

1-47) Seki, A.; Ishizone, T.; Oyane, A.; Yokoyama, H. A Segregation and Deprotection Approach for Hydrophilic Surfaces Using Amphiphilic Block Copolymers Possessing Polystyrene and Poly[(tri(ethylene glycol) methacrylate)] segments. *Macromol. Chem. Phys.*, **2017**, *218*, 1700048.

1-48) Kawaguchi, D.; Tanaka, K.; Torikai, N.; Takahara, A.; Kajiyama, T. Surface and Interfacial Segregation in Blends of Polystyrene with Functional End Groups and Deuterated Polystyrene. *Langmuir*, **2007,** *23,* 7269.

1-49) Kawaguchi, D.; Tanaka, K.; Takahara, A.; Tasaki, S.; Kajiyama, T. Surface Composition Control

via Chain End Segregation in Blend Films of Polystyrene and Poly(vinyl methyl ether). *Macromolecules*, **2003,** *36,* 6824.

1-50) Tanaka, K.; Takahara, A.; Kajiyama, T. Surface Molecular Aggregation Structure and Surface Molecular Motions of High-Molecular-Weight Polystyrene/Low-Molecular-Weight Poly(methyl methacrylate) Blend Films. *Macromolecules*, **1998,** *31,* 863.

1-51) Tanaka, K.; Takahara, A.; Kajiyama, T. Effect of Polydispersity on Surface Molecular Motion of Polystyrene Films. *Macromolecules*, **1997,** *30,* 6626.

1-52) Owens, D. K.; Wendt, R. C. Estimation of the Surface Free Energy of Polymers. *J. Appl. Polym. Sci.*, **1969,** *13,* 1741.

1-53) Popelka, A.; Kronek, J.; Novak, I.; Kleinova, A.; Micusik, M.; Spirkova, M.; Omastova, M. Surface Modification of Low-density Polyethylene with Poly(2-ethyl-2-oxazoline) Using a Low-pressure Plasma Treatment. *Vacuum*, **2014,** *100,* 53.

1-54) Walton, D. G.; Soo, P. P.; Sofia Allgor, S. J.; Fujii, J. T.; Griffith, L. G.; Ankner, J. F.; Kaiser, H.; Johansson, J.; Smith, G. D.; Barker, J. G.; Satija, S. K.; Mayes, A. M. Creation of Stable Poly(ethylene oxide) Surfaces on Poly(methyl methacrylate) Using Blends of Branched and Linear Polymers. *Macromolecules*, **1997,** *30,* 6947.

1-55) Yethiraj, A. Entropic and Enthalpic Surface Segregation from Blends of Branched and Linear Polymers. *Phys. Rev. Lett.*, **1995,** *74,* 2018.

1-56) Hirai, T.; Huan, L.; Ohta, Y.; Yokozawa, T.; Tanaka, K. Surface Segregation of Well-defied N-Substituted Hyperbranched Polyamides in Linear Polymer Matrix. *Chem. Lett.*, **2011,** *40,* 366.

1-57) Atarashi, H.; Ariura, F.; Akabri, K.; Ozawa, M.; Tanaka, K.; Nagamura, T. Interfacial Segregation of Hyper-branched Polystyrene in Mixtures of Linear Component. *Trans. Mater. Res. Soc. Jpn.*, **2007**, *32*, 231.

1-57) Mitra, I.; Li, X.; Pesek, S. L.; Makarenko, B.; Lokitz, B. S.; Uhrig, D.; Ankner, J. F.; Verduzco, R.; Stein, G. E. Thin Film Phase Behavior of Bottlebrush/Linear Polymer Blends.

Macromolecules, **2014,** *47,* 5269.

1-59) Verduzco, R.; Li, X.; Pesek, S. L.; Stein, G. E. Structure, Function, Self-assembly, and Application of Bottlebrush Copolymers. *Chem. Soc. Rev.*, **2015,** *44,* 2405.

1-60) Li, X.; ShamsiJazeyi, H.; Pesek, S. L.; Agrawal, A.; Hammoud, B.; Verduzco, R. Thermoresponsive PNIPAAM Bottlebrush Polymers with Tailored Side-chain Length and End-group Structure. *Soft Matter*, **2014,** *10,* 2008.

1-61) Takahara, A.; Morotomi, N.; Hiraoka, S.; Higashi, N.; Kunitake, T.; Kajiyama, T. Analysis of the Surface Structure of a Built-Up Film of Fluorocarbon Amphiphile and Polymer/(Fluorocarbon Amphiphile) Composite Thin Film by Means of X-ray Photoelectron Spectroscopy. *Macromolecules*, **1989**, *22*, 617.

1-62) Zhao, X.; Zhao, W.; Sokolov, J.; Rafailovich, M. H.; Schwarz, S. A.; Wilkens, B. J.; Jones, R. A. L.; Kramer, E. J. Determination of the Concentration Profile at the Surface of d-PS/h-PS Blends Using High-resolution Ion Scattering Techniques. *Macromolecules*, **1991**, *24*, 5991.

1-63) Ishihara, K.; Aragaki, R.; Ueda, T.; Watenabe, A.; Nakabayashi, N. Reduced Thrombogenicity of Polymers having Phospholipid Polar Groups. *J. Biomed. Mater. Res.*, **1990**, *24*, 1069.

1-64) Inutsuka, M.; Ito, K.; Yamada, N. L.; Yokoyama, H. High Density Polymer Brush Spontaneously Formed by the Segregation of Amphiphilic Diblock Copolymers to Polymer/water Interface. *ACS Macro Lett.*, **2013**, *2*, 265.

1-65) Matsuno, H.; Tsukamoto, R.; Shimomura, S.; Hirai, T.; Oda, Y.; Tanaka, K. Platelet-adhesion Behavior Synchromized with Surface Rearrangement in a Film of Poly(methyl methacrylate) terminated with elemental blocks. *Polym. J.*, **2016**, *48*, 419.

1-66) Kobayashi, M.; Terayama, Y.; Yamaguchi, H.; Terada, M.; Murakami, D.; Ishihara, K.; Takahara, A. Wettability and Antifouling Behavior on the Surfaces of Superhydrophilic Polymer Brushes. *Langumuir*, **2012**, *28*, 7212.

1-67) Takahara, A.; Jo, N. J.; Kajiyama, T. Surface Molecular Mobility and Platelet Reactivity of

Segmented Poly(etherurethaneureas) with Hydrophilic and Hydrophobic Soft Segment Components. *J. Biomater. Sci. Polymer Edn.*, **1989**, *1*, 17.

1-68) Tateishi, Y.; Kai, N.; Noguchi, H.; Uosaki, K.; Nagamura, T.; Tanaka, K. Local Conformation of Poly(methyl methacrylate) at Nitrogen and Water Interfaces. *Polym. Chem.*, **2010**, *1*, 303.

1-69) Oda, Y.; Horinouchi, A.; Kawaguchi, D.; Matsuno, H.; Kanaoka, S.; Aoshima, S.; Tanaka, K. Effect of Side-Chain Carbonyl Groups on the Interface of Vinyl Polymers with Water. *Langmuir*, **2014**, *30*, 1215.

1-70) Hirata, T.; Matsuno, H.; Kawaguchi, D.; Hirai, T.; Yamada, N. L.; Tanaka, M.; Tanaka, K. Effect of Local Chain Dynamics on a Bio-inert Interface. *Langmuir*, **2015**, *31*, 3661.

1-71) Tanaka, K.; Fujii, Y.; Atarashi, H.; Akabori, K.; Hino, M.; Nagamura, T. Nonsolvents Cause Swelling at the Interface with Poly(methyl methacrylate) Films. *Langmuir*, **2008**, *24*, 296.

1-72) Fujii, Y.; Nagamura, T.; Tanaka, K. Relaxation Behavior of Poly(methyl methacrylate) at a Water Interface. *J. Phys. Chem. B*, **2010**, *114*, 3457.

1-73) Gombotz, W. R.; Guanghui, W.; Horbett, T. A.; Hoffman, A. S. Protein Adsorption to Poly(ethylene oxide) Surfaces. *J. Biomed. Mater. Res.*, **1991**, *25*, 1547.

1-74) Itagaki, N.; Oda, Y.; Hirata, T.; Nguyen, H. K.; Kawaguchi, D.; Matsuno, H.; Tanaka, K. Surface Characterization and Platelet Adhesion on Thin Hydrogel Films of Poly(vinyl ether). *Langmuir*, **2017**, *33*, 14332.

1-75) Liu D.; Guo, J.; Zhang, J. H. Chain Mobility and Film Softness Mediated Protein Antifouling at the Solid-liquid Interface. *J. Mater. Chem. B*, **2016**, *4*, 6134.

Chapter 2 Synthesis of well-defined poly(2-ethyl-2-oxazoline) derivatives

2.1. Background

Structure and physical properties of polymers at surface is a pivotal importance for the surface functionality such as adhesive and antifouling properties. In order to express desirable surface functionality, it is required to control surface structures and their physical properties. An effective method to control the surface properties is to introduce well-defined polymer structure.[2-1,2)] In an early study, Tanaka *et al.* reported that monodisperse PS with a number average molecular weight (M_n) of 19.7k, referred to as PS 19.7k, was localized on the binary PS the film, which was blended with higher M_n of PS, and surface chain mobility was activated, showing the characteristics of the glass-rubber transition state, even at 293 K even though the bulk T_g of the PS 19.7k was 365 K. However, if polydisperse PS was added in the binary PS film instead of the monodisperse PS 19.7k, such the chain mobility at the glass-rubber transition state did not appear even though small molecular weight of PS was also contained in polydisperse PS.[2-1)] The results imply that the introduction of precisely controlled polymer structure is necessary to possess desirable physical properties[2-1)] and functionality at the interface.[2-2)]

PEtOxs are prepared by living cationic ring-opening polymerization (LCROP) of 2-ethyl-2-oxazoline with highly controlled degree of polymerization and low molecular weight distribution. Also, the use of functionalized initiators or livingness of LCROP makes easy to introduce broad structural diversity at the chain end group.[2-3)] However, LCROP has a disadvantage of using nucleophiles or protection process in the reaction mechanism as a side reaction of unexpected termination.[2-4)] That is, it is difficult to use common vinyl monomers like living radical polymerization.[2-5)] However, recently, introducing the functional end group, such as methacrylate group, it becomes possible to combine the LCROP with

common living radical polymerization methods, like reversible addition-fragmentation chain-transfer polymerization (RAFT)[2-6,7] or atom transfer radical polymerization (ATRP).[2-8,9] That means that diverse vinyl monomers now become accessible to the PEtOx structure overcoming the synthetic drawback. These collaborations give diverse chance to construct well-defined and unique block copolymer structure by combining vinyl/ or methacrylate monomer group in a living manner. In practice, U.S. Schubert *et al*. successfully synthesized well-defined poly(2-ethyl-2-oxazoline)-*b*-poly(styrene) by combining LCROP and ATRP with dual initiator.[2-8] R. Jordan. *et al.* successfully synthesized chain end functionalized with methacrylate by end capping methods, then, prepared a graft polymer via ATRP. [2-9]

In this chapter, amphiphilic-type block copolymer containing PEtOx was planned to be synthesized to construct a stable bio-inert PEtOx surfaces. To increase the stability and the film formability of PEtOx based block copolymer, poly(methyl methacrylate) (PMMA), which is a common hydrophobic structure and well-known for the film forming, was chose for the counter block. Then, following two synthetic strategies were planned to apply to covalently connect the PEtOx with PMMA. (1) Using bromide end-group functionalized PEtOx as a macroinitiator, methyl methacrylate was polymerized by ATRP. (2) Using bromide end-group functionalized PMMA as a macroinitiator, methyl methacrylate terminated PEtOx was polymerized by ATRP.

2.2. Experimental

Scheme 2-1 shows two synthetic routes for (a) poly(2-ethyl-2-oxazoline)-*block*-poly(methyl methacrylate) (PEtOx-*b*-PMMA) and (b) poly(methyl methacrylate)-*block*-poly[oligo(2-ethyl-2-oxazoline) methacrylate] (PMMA-*b*-P[O(Ox)$_n$MA]. .

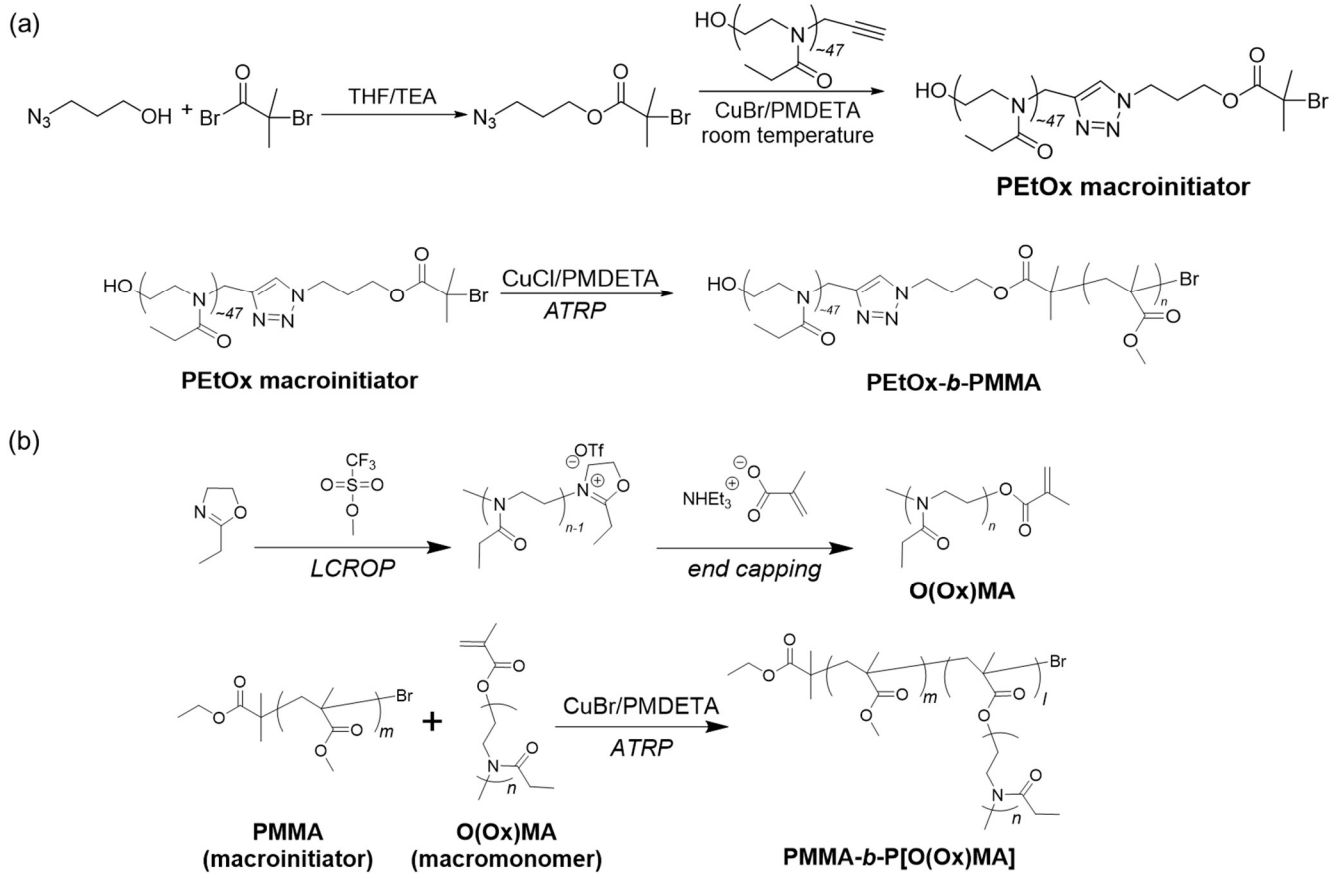

Scheme 2-1. Synthesis routes for block copolymers. (a) Linear PEtOx-*b*-PMMA was prepared combination of click reaction and ATRP. (b) Comb-*like* PMMA-*b*-P[O(Ox)$_n$MA] was synthesized by LCROP and ATRP.

2.2.1. Materials

α-bromoisobutyryl bromide (purity > 98.0 %), 2,2′-bipyridine (bpy, purity > 98.0 %), 2-ethyl-2-oxazoline (purity > 98.0 %), ethyl α-bromoisobutyrate (EBiB, purity > 98.0 %), triethylamine (TEA, purity > 99.0 %), potassium carbonate (K_2CO_3, > 99.5 %), and lithium bromide (LiBr, purity > 99.0 %) were purchased from Tokyo Chemical Industry Co., Tokyo, Japan (TCI). Tetrahydrofuran (THF, purity

> 99.5 %), methyl methacrylate (MMA, purity > 98.0 %), methyl trifluoromethanesulfonate (MeOTf, purity > 95.0 %), acetonitrile (purity > 99.8 %), *N,N*-dimethylformamide (DMF, purity > 99.5 %), diethyl ether (purity > 99.5 %), anisole (purity > 99 %), and basic alumina (particle size of approximately 75 μm) were purchased from FUJIFILM Wako Pure Chemical FUJIFILM Wako Pure Chemical Corp., Osaka, Japan. Calcium hydride (CaH_2, purity > 90.0 %) was purchased from NACALAI TESQUE, INC., Kyoto, Japan. 3-azido-1-propanol (purity ≥ 96.0 %), alkyne terminated PEtOx (M_n = 5000, M_w/M_n < 1.2), methacrylic acid (MAA, purity > 99.0%) was purchased from Merck, KGaA, Darmstadt, Germany. *N*,*N*,*N*′,*N*″,*N*″-pentamethyldiethylenetriamine (PMDETA, purity > 99.0 %) and chloroform-*d* ($CDCl_3$, purity > 99 %, 99.8 % atom D) containing tetramethylsilane (TMS, 0.03 % (v/v)) were purchased from Merck. Copper(I) bromide (CuBr, purity > 95 %), copper(II) bromide ($CuBr_2$ > 95 %), copper(I) chloride (CuCl, purity > 95 %) and methanol (purity > 99.5 %) were purchased from Kishida Chemical Co. Ltd., Osaka, Japan. Toluene (purity > 99.0 %), chloroform (purity > 99.0 %), and hexane (purity > 96.0 %) were purchased from Kanto Chemical Co., Tokyo, Japan.

2-ethyl-2-oxazoline, TEA, MeOTf, and acetonitrile were distilled with CaH_2. MAA was distilled under vacuum condition to remove inhibitors. MMA was purified by passing through a column filled with basic alumina to remove inhibitors. Chemicals other than stated were used as received.

2.2.2. Chemical Structure Characterizations

Chemical structures of products were characterized by ^{1}H-nuclear magnetic resonance (^{1}H NMR) spectroscopy using an ECZ-400S spectrometer (JEOL Ltd., Akishima, Tokyo, Japan) at 298 K. As a solvent, $CDCl_3$ containing 0.03 v/v% TMS was used. M_n and the molecular weight distribution (M_w/M_n) of the obtained polymers, where M_w is the weight-average molecular weight (M_w), were determined by using size exclusion chromatography (SEC) on HLC-8120GPC (TOSOH Corp., Tokyo, Japan) set with TSKgel Super AW5000 and AW4000 columns which are packed with a micro-particulate gel based on hydrophilic vinyl polymer (6.0 mm internal diameter × 150 mm length for each column, TOSOH Corp.).

Refractive index (RI) detector were used for detection. As an eluent, DMF mixed with 10 mM of LiBr and 30 mM of TEA was used, and flow rate and the temperature were set as 0.5 mL·min^{-1} and 313 K, respectively. For a calibration, five kinds of monodisperse PMMA (Merck) were used.

2.2.3. Bulk Characterizations

T_g of the products was estimated by differential scanning calorimetry (DSC, EXSTAR6000 DSC6220, Hitachi High-Tech Science Corp., Tokyo, Japan). Measuring temperature was in the range of 213 to 433 K for the block copolymers. The heating and cooling rates were 10 K·min^{-1}. Polymer samples were placed in an aluminum pan and an empty aluminum pan was used as a reference. Aggregation structure in the bulk state of the block copolymers was estimated by small angle X-ray scattering (SAXS) measurement. For the measurement, self-standing film of PMMA-*b*-P[O(Ox)$_n$MA] were prepared by a solvent casting method, then, the films were annealed at ($T_{g,u}$+20) K under vacuum for 24 h, where $T_{g,u}$ is the upper T_g of each block copolymers. The SAXS measurements were carried out at the BL03XU beamline of Japan Synchrotron Radiation Research Institute (SPring-8, Hyogo, Japan). The X-ray wavelength and the camera distance from the detector was 0.1 nm and 2,310 mm, respectively. Silver behenate was used for the calibration of the camera distance. PILATUS3 S 1M (DECTRIS Ltd., Baden-Däettwil, Switzerland) was used to record two-dimensional SAXS patterns.

2.2.4. Synthesis of a PEtOx macroinitiator by click reaction

Synthesis of a 3-azidopropyl 2-bromoisobutyrate. 3-azidopropyl 2-bromoisobutyrate was synthesized as follows.[2-10] α-bromoisobutyryl bromide (1.30 mL, 10.4 mmol) dissolved in 10.0 mL of THF. The solution was dropwise added to a solution of 3-azido-1-propanol (0.460 mL, 10.0 mmol) and TEA (1.80 mL, 12.9 mmol) that dissolved 10.0 mL of THF at 273K. The reaction mixture was stirred at room temperature (RT) for 24 h. After the reaction, excess amounts of α-bromoisobutyryl bromide was

quenched by charging 5.00 mL of degassed methanol. Triethylammonium bromide salt was filtered and the remaining solution was evaporated. The crude product dissolved in CH_2Cl_2 and washed 5 times with distilled water. The organic layer was collected with drying over sodium sulfate (Na_2SO_4) for 2 h. The solution was filtered and concentrated. The unreacted 3-azido-1-propanol was separated using SiO_2 column with ethyl acetate: hexane (7:3) mixture as an eluent. The yellow liquid product was collected. ^{1}H NMR (400 MHz, $CDCl_3$): δ = 1.95 ppm (m, 9H, CH_2–CH_2–CH_2, C– (CH_3)$_2$), δ = 3.43 ppm (t, 2H, CH_2–CH_2–N_3), δ = 4.28 ppm (t, 2H, CH_2–CH_2–O–C(=O)).

Synthesis of a PEtOx Macroinitiator via click reaction. A Schlenk tube was dried and filled with Ar gas. 3-azidopropyl 2-bromoisobutyrate (38.0 mg, 0.150 mmol), alkyne terminated PEtOx (0.500 g, 0.100 mmol), bpy (57.8 mg, 0.370 mmol), and 2.40 mL of DMF were charged into the reaction tube. CuBr (43.6 mg, 0.300 mmol) was added into the reaction tube after bubbling the solution with Ar gas for 2 min. Reaction was proceeded at RT for 24 h. After the reaction, CuBr/bpy catalytic complex was removed passing through alumina column and the macroinitiator was recovered by evaporation. The white power of the PEtOx macroinitiator was obtained. ^{1}H NMR (400 MHz, $CDCl_3$): δ = 1.13 ppm (br, 218H, CH_2–CH_3), δ = 1.95 ppm (br, N–CH_2–CH_2–CH_2, C– (CH_3)$_2$), δ = 2.34 ppm (br, 167H, C(=O) – CH_2–CH_3), δ = 3.46 ppm (br, 284H, –N–CH_2–CH_2–), δ = 4.18 ppm (br, 2H, N-CH_2-CH_2), δ = 4.47 ppm (m, 2H, CH_2-CH_2-O-C(=O)), δ = 4.60 ppm (s, 2H, O–CH_2–C(=C) –N), δ = 7.67 ppm (br, 1H, C(=C) – CH–N, triazole).

2.2.5. ATRP of MMA using the PEtOx macroinitiator

Poly(2-ethyl-2-oxazoline)-*block*-poly(methyl methacrylate) (PEtOx-*b*-PMMA) was polymerized through ATRP. The detail procedures are as follows. First, a Schlenk tube was baked for 5 min and was filled with Ar gas. MMA monomer, PEtOx macroinitiator, PMDETA ligand, anisole solvent, and an internal standard of 1,2,3-trimethoxy benzene (TMB) were added to the reaction tube. The solution was

deoxygenated by bubbling with Ar gas for 2 min. Copper catalyst was added into the tube, and the reaction mixture was bubbled again with Ar gas for additional 2 min. The polymerization was proceeded at 353K. The monomer conversion was confirmed by ^{1}H NMR spectroscopy by comparing the residual monomer concentration in the reaction mixture against TMB as an internal standard.

2.2.6. Synthesis of methacrylate-terminated oligo(2-ethyl-2-oxazoline) (O(Ox)nMA)s

Methacrylate-terminated macromonomers, oligo(2-ethyl-2-oxazoline) methacrylate with degree of oligomerization of 9 referred to as O(Ox)$_9$MA, was synthesized by living cationic ring-opening polymerization (LCROP) of 2-ethyl-2-oxazoline. A synthesis procedure was as follows.[2-9)] Methyl trifluoromethanesulfonate (MeOTf; 4.26 mL, 38.9 mmol) was dissolved in 76.0 mL of acetonitrile in a 300 mL round flask. 2-ethyl-2-oxazoline (25.3 mL, 250 mmol) was slowly added to the mixture at RT. The mixture was bubbled with Ar gas for 3 min, and then, the reaction mixture was kept at 363 K for 2 h. Then, the mixture was cooled down to RT after the reaction. For the end-capping of the oligo(2-ethyl-2-oxazoline) in a living manner, MAA (8.24 mL, 97.3 mmol) and TEA (13.5 mL, 97.3 mmol) were added to the mixture, and then, stirred at 343 K for 12 h. After cooling down to the RT, saturated amount of K_2CO_3 was added accompanying with stirring the mixture for additional 24 h. Resulting precipitation was obtained after passing through a polytetrafluoroethylene (PTFE) syringe filter with pore-size of 0.2 μm. The solvent was evaporated and the obtained solid was dissolved again into methanol following by precipitation in 10-fold excess of cold diethyl ether. The obtained precipitation was dried under vacuum for 2 days. A yellow-like powder of O(Ox)$_9$MA was obtained. ^{1}H NMR (400 MHz, $CDCl_3$): δ = 1.12 ppm (br, 27H, C*H*$_3$–CH$_2$–C(=O)–), 1.91 ppm (s, 3H, C*H*$_3$–C(=CH$_2$)–), 2.27 ~2.38 ppm (br, 18H, CH$_3$–C*H*$_2$–C(=O)–), 2.95 ~ 3.02 ppm (m, 3H, C*H*$_3$–N(–C=O)–), 3.50 (br, 34H, –N–C*H*$_2$–C*H*$_2$–), 4.26 (t, 2H, –CH$_2$–C*H*$_2$–O–C(=O)–), 5.58 ppm (s, 1H, –C=C*H*$_2$) and 6.06 ppm (s, 1H, –C=C*H*$_2$).

O(Ox)$_{13}$MA was synthesized in a same procedure described above. And, MeOTf (4.55 g, 3.03 mL, 27.7 mmol), 2-ethyl-2-oxazoline (25.3 mL, 250 mmol), MAA (5.87 mL, 69.3 mmol), TEA (9.63 mL,

69.3 mmol) were used for the reaction. A white power was obtained after purification. ^{1}H NMR (400 MHz, $CDCl_3$): δ = 1.12 ppm (br, 40H, C*H*$_3$–CH_2–C(=O)–), 1.91 ppm (s, 3H, C*H*$_3$–C(=CH_2)–), 2.27 ~2.38 ppm (br, 26H, CH_3–C*H*$_2$–C(=O)–), 2.95 ~ 3.02 ppm (m, 3H, C*H*$_3$–N(–C=O)–), 3.50 (br, 52H, –N–C*H*$_2$–C*H*$_2$–), 4.26 (t, 2H, –CH_2–C*H*$_2$–O–C(=O)–), 5.58 ppm (s, 1H, –C=C*H*$_2$) and 6.06 ppm (s, 1H, –C=C*H*$_2$).

2.2.7. ATRP of MMA using an ethyl α-bromoisobutyrate (EBiB)

A bromide-terminated PMMA macroinitiator was synthesized by ATRP.[2-11] For the detail procedure, a Schlenk tube was baked for 5 min and was filled with Ar gas. EBiB (0.200 mL, 1.38 mmol) and MMA (29.5 mL, 277 mmol), and PMDETA (0.290 mL, 1.38 mmol) were dissolved in anisole (29.7 mL) in the reaction tube. The mixture was deoxygenated by bubbling with Ar gas for 2 min. The reaction mixture was bubbled again for 2 min after adding CuBr (198 mg, 1.38 mmol) in the reaction tube. The reaction tube was placed in an oil bath, and it was kept at 353 K for 2 h. After the reaction, the solution was diluted, and then, it was passed through an alumina column to remove the catalyst complex. The solution was then precipitated into hexane 3 times. A white powder of the PMMA macroinitiator was obtained. ^{1}H NMR (400 MHz, $CDCl_3$): δ = 0.81 ~ 1.26 ppm (br, 625H, C*H*$_3$–CH_2–O–(C=O)–, –C(C*H*$_3$)$_2$–, –CH_2–C(C*H*$_3$)–), 1.43 ~ 2.10 ppm (br, 381H, –C*H*$_2$–C(CH_3)–), 3.53 ppm (s, 624H, –C(C=O)–O–C*H*$_3$), 4.01 ppm (m, 2H, CH_3–C*H*$_2$–O–(C=O)–).

2.2.8. ATRP of O(Ox)nMA using the PMMA macroinitiator

A block copolymer, PMMA-*b*-P[O(Ox)$_9$MA], was synthesized by ATRP of O(Ox)$_9$MA using an PMMA macroinitiator. A typical method was as follows. A Schlenk tube was baked for 5 min and then the tube was filled with Ar gas. PMMA macroinitiator (1.27 g, 0.0600 mmol) and O(Ox)$_9$MA (2.97 g, 3.00 mmol), PMDETA (0.120 mL, 0.0600 mmol), and 4.61 mL of DMF were added into the Schlenk tube. The mixture was deoxygenated by bubbling with Ar gas for 2 min. The reaction mixture was

bubbled for additional 2 min after adding CuBr (8.60 mg, 0.0600 mmol) to the reaction mixture. The reaction was proceeded at 353 K for 30 min. After the reaction, the mixture was precipitated into hexane several times to remove unreacted macromonomer. A solid product was obtained after dried under vacuum over 12 h. The dried solid was dissolved in methanol, and subsequently, the solution was dialyzed for 2 days by methanol. After checking the blue like color was totally removed, the solution was concentrated by evaporation and precipitated again in hexane. The white power of the block copolymers was obtained. ^{1}H NMR (400 MHz, $CDCl_3$): δ = 0.81 ~ 1.26 ppm (br, 137H, C*H*$_3$–CH_2–O–(C=O)–, –C(C*H*$_3$)$_2$–,–CH_2–C(C*H*$_3$)–, C*H*$_3$–CH_2–C(=O)–N–), 1.43 ~ 2.10 ppm (br, 49H, –C*H*$_2$–C(CH_3)–), 2.27 ~2.38 ppm (br, 16H, CH_3–C*H*$_2$–C(=O)–N–), 2.95 ~3.05 ppm (m, 3H, C*H*$_3$–N(–C=O)–), 3.44 ppm (s, 26H, –N(–C(=O))–C*H*$_2$–C*H*$_2$–), 3.59 ppm (s, 81H, C(C=O) –O–C*H*$_3$), 3.74 ~ 4.09 ppm (br, 2H, CH_3–C*H*$_2$–O–(C=O)–, C(C=O)–O–C*H*$_2$–CH_2–N–).

PMMA-*b*-P[O(Ox)$_{13}$MA] was synthesized in a same manner. And, PMMA macroinitiator (1.27 g, 0.0600 mmol), O(Ox)$_{13}$MA (4.16 g, 3.00 mmol), PMDETA (0.120 mL, 0.0600 mmol), and CuBr (8.60 mg, 0.0600 mmol) were used for the reaction. ^{1}H NMR (400 MHz, $CDCl_3$): δ = 0.81 ~ 1.26 ppm (br, 106H, C*H*$_3$–CH_2–O–(C=O)–, –C(C*H*$_3$)$_2$–, –CH_2–C(C*H*$_3$)–, C*H*$_3$–CH_2–C(=O)–N–), 1.43 ~ 2.10 ppm (br, 36H, –C*H*$_2$–C(CH_3)–), 2.27 ~2.38 ppm (br, 24H, CH_3–C*H*$_2$–C(=O)–N–), 2.95 ~3.05 ppm (m, 3H, C*H*$_3$–N(–C=O)–), 3.44 ppm (s, 66H, –N(–C(=O))–C*H*$_2$–C*H*$_2$–), 3.59 ppm (s, 55H, C(C=O) –O–C*H*$_3$), 3.74 ~ 4.09 ppm (br, 2H, CH_3–C*H*$_2$–O–(C=O)–, C(C=O)–O–C*H*$_2$–CH_2–N–).

2.2.9. Synthesis of a 2-hydroxyethyl 2-bromoisobutyrate (HEBiB) initiator

To prepare an ATRP initiator used in aqueous solution, a water soluble ATRP initiator of HEBiB was synthesized.[2-12] First, TEA and THF were dried with molecular sieve. 1000 mL size of a reaction flask was baked using heating gun under vacuum. Anhydrous ethylene glycol (55.7 mL, 1000 mmol), TEA (21.8 mL, 150 mmol), THF (700 mL) was charged into the reaction flask, following the tube was purged the mixture with N_2. 2-Bromoisobutyryl bromide (12.3 mL, 100 mmol) which was dissolved in THF

(200 mL), subsequently, dropwise added to the mixture which was kept the temperature below 273 K with ice bath. The reaction was proceeded at RT overnight. After removing the side product of salt by filtration, the solution was concentrated. 80.0 mL of deionized water was mixed with the solution, subsequently, the mixed solution was extracted with chloroform. The chloroform phase was separately collected and dried with anhydrous magnesium sulfate ($MgSO_4$). The yellow oil was obtained after removing solvent. ^{1}H NMR (400 MHz, $CDCl_3$): δ = ppm (s, 6H, –C(C*H*$_3$)$_2$–Br), ppm (s, 1H, –O*H*), ppm (m, 2H, –C*H*$_2$–OH), and ppm (m, 2H, –C*H*$_2$–C*H*$_2$).

2.2.10. ATRP of O(Ox)nMA using the HEBiB initiator

For the synthesis of bottlebrush P[O(Ox)$_n$MA], O(Ox)$_n$MA with degrees of oligomerization of 7 and 19 were prepared in the same manner described above. Scheme 2-2 shows ATRP synthetic route for P[O(Ox)$_7$MA] using O(Ox)$_7$MA macromonomer and HEBiB initiator.[2-9] First, ultrapure water was degassed under nitrogen flow for 30 min. O(Ox)$_7$MA macromonomer (2.14 g, 2.88 mmol), 0.5 M HEBiB/DMF solution (0.360 mL, 0.180 mmol), were added into a Schlenk tube. CuBr (25.8 mg, 0.180 mmol), $CuBr_2$ (0.360 g, 1.62 mmol) and bpy (0.620 g, 3.96 mmol) were added into another tube. Both tubes were evacuated, following by purging with dried Ar gas for 3 times. Then, the degassed water (15.5 ml) was charged into the both tubes. After checking the macromonomer totally dissolved in water, the macromonomer/initiator solution was transfer to the other tube. The reaction mixture was stirred at RT for 30 min. Then, the reaction was stopped by injected the air, subsequently, subsequently, the reaction mixture was diluted with additional water. The catalyst complex was removed through dialysis for 2 days with excess of water. The polymer solution was freeze-dried overnight and dissolved in chloroform. The yellow like powder was precipitated by adding hexane, and the precipitation was repeated for 3 times to completely remove unreacted macromonomers. Finally, the slightly yellow power was obtained after the purification. ^{1}H NMR (400 MHz, $CDCl_3$): δ = 0.77 ~ 1.25 ppm (br, 26H, C*H*$_3$–CH_2–C(=O)– and –CH_2–C(C*H*$_3$)–), 1.85 ppm (br, 10H, –C*H*$_2$–C(CH_3)– and water), 2.28 ~ 2.39 ppm (br,

14H, CH_3–C*H*$_2$–C(=O)–), 2.95 ~ 3.06 ppm (m, 3H, C*H*$_3$–N(–C=O)–), 3.44~ 3.74 ppm (br, 27H, –N–C*H*$_2$–C*H*$_2$–), 4.02 ppm (br, 2H, –CH_2–C*H*$_2$–O–C(=O)–).

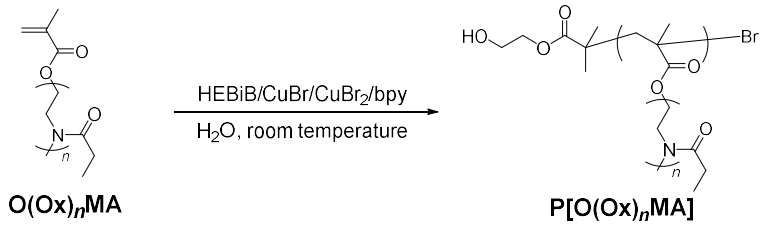

Scheme 2-2. A synthesis route for bottlebrush P[O(Ox)$_n$MA] by ATRP.

P[O(Ox)$_{19}$MA] was synthesized in a same manner. O(Ox)$_{19}$MA (1.81 g, 0.960 mmol), 0.5 M of HEBiB/DMF solution (0.120 mL, 0.0600 mmol), CuBr (8.60 mg, 0.0600 mmol), $CuBr_2$ (0.120 g, 0.540 mmol) and bpy (0.210 g, 1.32 mmol) were used for the reaction. ^{1}H NMR (400 MHz, $CDCl_3$): δ =0.77 ~ 1.24 ppm (br, 64H, C*H*$_3$–CH_2–C(=O)– and –CH_2–C(C*H*$_3$)–), 1.84 ppm (br, 22H, –C*H*$_2$–C(CH_3)– and water), 2.28 ~ 2.40 ppm (br, 38H, CH_3–C*H*$_2$–C(=O)–), 2.95 ~ 3.06 ppm (m, 3H, C*H*$_3$–N(–C=O)–), 3.44~ 3.72 ppm (br, 74H, –N–C*H*$_2$–C*H*$_2$–), 4.03 ppm (br, 2H, –CH_2–C*H*$_2$–O–C(=O)–).

2.3. Results and discussion

2.3.1. Synthesis of the PEtOx macroinitiator via click reaction

To introduce bromoisobutyrate functionality at PEtOx end group, azide-alkyne click reaction between alkyne-terminated PEtOx and 3-azidopropyl 2-bromoisobutyrate was conducted. Panels (a, b) of Fig. 2-1 show ^{1}H NMR spectra of the 3-azidopropyl 2-bromoisobutyrate and the commercial available alkyne-terminated PEtOx. All signals in the spectrum of the 3-azidopropyl 2-bromoisobutyrate were well corresponding with the chemical structures. However, in the spectrum for the alkyne-terminated PEtOx, a NMR signal denoted for alkyne proton was not observed and it was shielded by signals of methyl group of oxazoline side chain around 2.5 ppm, that is, it is impossible to quantify the alkyne functionality at the chain-end of PEtOx by NMR measurement. However, considering synthesis process for alkyne-terminated PEtOx which is polymerized from alkyne functionalized initiator, it is assumed to have alkyne moiety at all the chain-end.

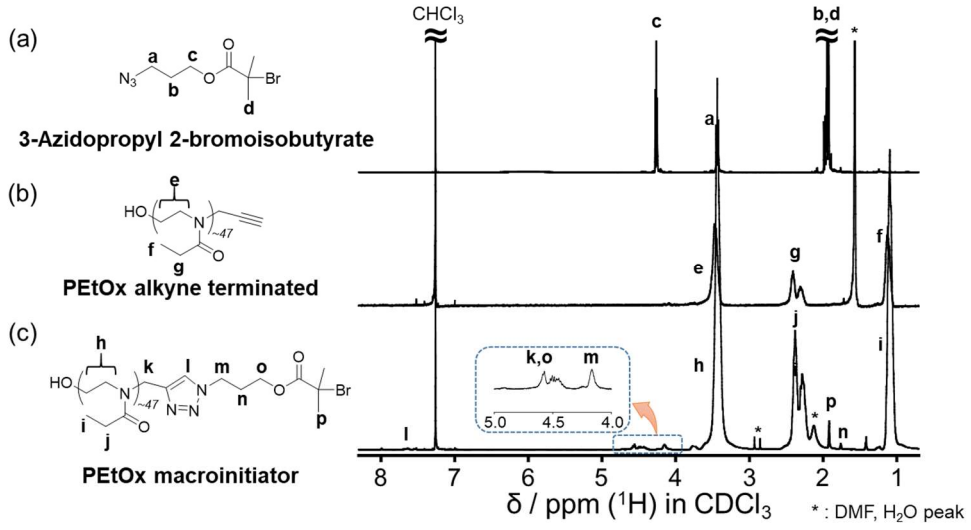

Fig. 2-1. ^{1}H NMR spectra measured in $CDCl_3$ with $CHCl_3$ as an internal standard. (a) 3-azidopropyl 2-bromoisobutyrate, (b) PEtOx alkyne terminated, and (c) PEtOx macroinitiators.

Panel (c) of Fig. 2-1 is the ^{1}H NMR spectrum of the obtained PEtOx macroinitiator. NMR signals corresponding with end group functionality especially the signal, which denoted newly formed triazole, were observed. The results indicated that bromoisobutyrate-functionalized PEtOx macroinitiator was successfully synthesized. The conversion to bromoisobutyrate end group was to be approximately 66% on the basis of signals **m** and **i** corresponding to end group and oxazoline repeating units, respectively. Because it is difficult to separate the PEtOx macroinitiator with unreacted PEtOx, and also the unreacted PEtOx is considered to do not interfere further polymerization process, next step of ATRP was persisted using the PEtOx macroinitiator mixing with unreacted PEtOx.

2.3.2. ATRP of MMA using the PEtOx macroinitiator

PEtOx-*b*-PMMA was polymerized through ATRP using the PEtOx macroinitiator. Table 2-1 summarizes the various polymerization conditions of copper halide/PMDETA complex and monomer concentration.

Table 2-1. Experimental conditions for the ATRP of MMA using PEtOx macroinitiator with different monomer concentration and different copper halide catalyst.

Entry	Copper halide	$[MMA]_0$ / M	$[MMA]_0$: $[PEtOx\ macroinitiator]_0$: $[Copper\ halide]_0$: $[PMDETA]_0$
1	CuBr	0.962	200 : 1 : 4 : 4
2	CuBr	3.00	200 : 1 : 4 : 4
3	CuCl	3.00	200 : 1 : 4 : 4

First, ATRP using CuBr/PMDETA complex catalyst at initial monomer concentration of 0.962 M was conducted. Panel (a) of Fig. 2-2 shows MMA monomer conversion and remaining monomer concentration in the reaction mixture. In the plot, the monomer conversion was gradually increased with polymerization time, and especially, the $\ln([M]_0/[M]_t)$ was increased with linearly, meaning that, the concentration of active radical was kept constant. Panel (b) of Fig. 2-2 shows SEC curves of obtained polymers at the polymerization time. Comparing with the SEC curve for the starting PEtOx

macroinitiator, the SEC curves started to increase at lower molecular weight region and then slightly shifted to higher molecular weight region. This result indicated that the monomer was polymerized, but not from the PEtOx macroinitiator. One of the reasons for the results is lower monomer concentration in the mixture. The lower monomer concentration could make the active radical site of the macroinitiator difficult to meet with the surrounding monomer, and then, the active radical easily migrates to the surrounding solvent molecule. Therefore, in the next reaction, the concentration of the monomer was increased to 3.00 M and the reaction proceeded.

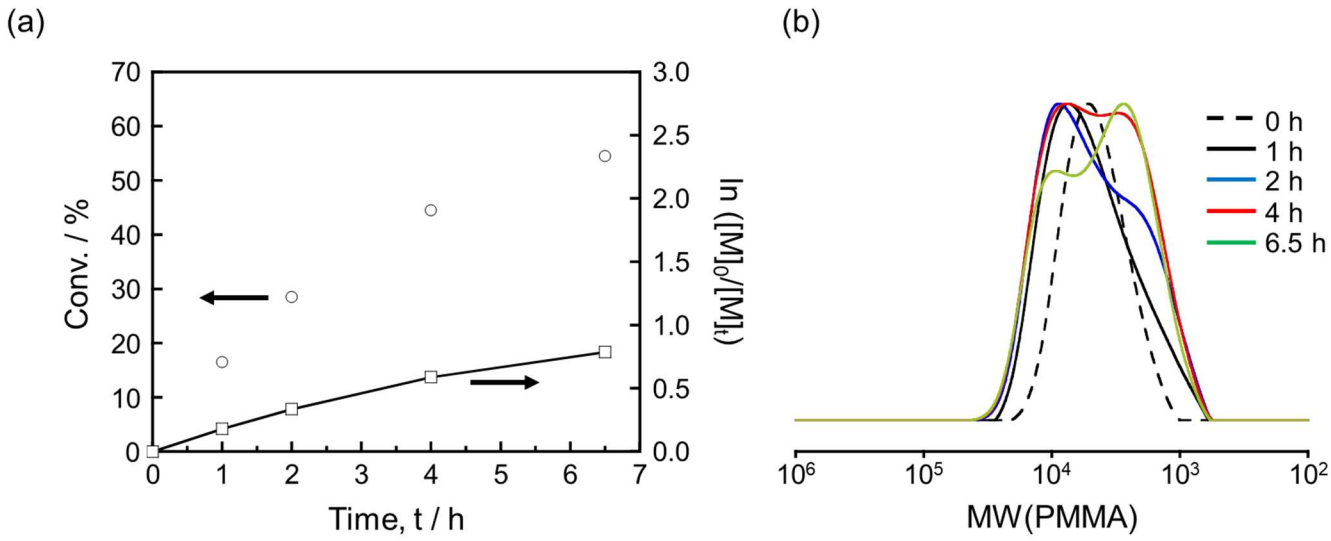

Fig. 2-2. (a) Kinetic study of ATRP using PEtOx macroinitiator with CuBr/PMDETA complex catalyst. Round shape denotes MMA conversion and rectangular shape is the remaining monomer concentration, and (b) SEC curves for PEtOx-*b*-PMMA on polymerization time. The polymerization time of 1 h, 2 h, 4 h, and 6.5 h was collected.; $[MMA]_0 = 0.962$ M; $[MMA]_0 : [PEtOx\ macroinitiator]_0 : [CuBr]_0 : [PMDETA]_0 = 200 : 1 : 4 : 4$; Reaction was proceeded in anisole at 353 K.

Panel (a) of Fig. 2-3 shows SEC trace with increasing polymerization time obtained in reaction mixture of MMA, PEtOx macroinitiator, and CuBr/PMDETA complex catalyst, and its monomer concentration of 3.00 M. Unlike previous condition, the SEC curves was not increased in lower molecular weight region. However, the curves drastically increased in higher molecular region. The result shows that chain transfer reaction to small molecules such as solvent was successfully suppressed, however, the

propagation reaction strongly activated, and it was failed to control. To improve the control, CuCl, which is less active than CuBr, was used as the catalyst, and the polymerization results were shown in panel (b) of Fig. 2-3.

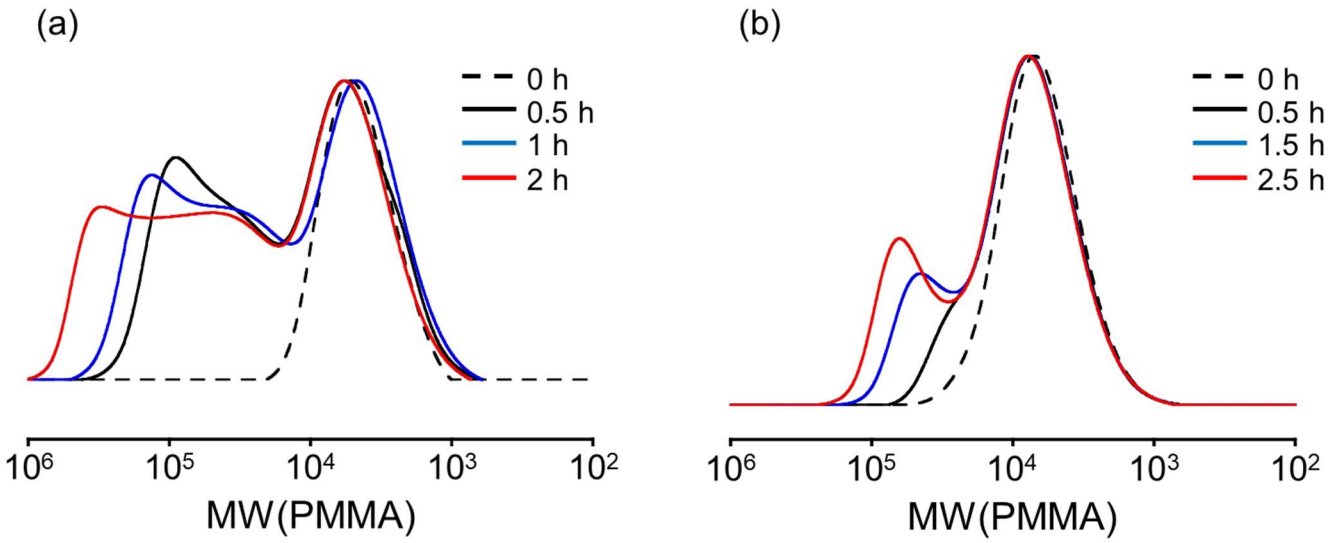

Fig. 2-3. SEC curves for the PEtOx-*b*-PMMA on polymerization time obtained in (a) $[MMA]_0$: $[PEtOx\ macroinitiator]_0$: $[CuBr]_0$: $[PMDETA]_0$ = 200 : 1: 4 : 4, (b) $[MMA]_0$: $[PEtOx\ macroinitiator]_0$: $[CuCl]_0$: $[PMDETA]_0$ = 200 : 1: 4 : 4. $[MMA]_0$ = 3.00 M. The reactions were proceeded in anisole at 353 K.

Panel (b) of Fig. 2-3 shows SEC traces obtained in the reaction mixture containing CuCl/PMDETA complex catalyst. As increasing polymerization time, the SEC curve corresponding with propagating chain was gradually increased in the diagonal direction. That means, initiation was not occurred at the same time and the living polymerization did not precisely be controlled under the polymerization condition. This is because halogen exchange between the PEtOx macroinitiators and copper complex is not occurred simultaneously. Also, the biggest component consisted of the bimodal peak was remained unchangeable. That means, a bunch number of initiators was remained deactivated including 34 % of alkyne terminated PEtOx. Dashed and solid line shown in Fig. 2-4 show SEC curves for the obtained mixture of PEtOx-*b*-PMMA/unreacted PEtOx macroinitiator, and the separated block copolymer, respectively. For the separation, PLC761 HPLC (GL Sciences, Inc., Tokyo, Japan) equipped with CROWNPAK CR column (4 mm internal diameter × 150 mm length, and the column packed with 5 μm

silica coated with chiral crown ether, Daicel Corporation, Tokyo, Japan). A 1 mg·mL^{-1} of polymer mixture/chloroform solution was injected into the instrument, and then, mixture solution corresponding with the RI signals appeared on relatively shorter eluent time was collected. As the results, the PEtOx-*b*-PMMA could be separated from unreacted PEtOx, however, the M_w/M_n of the block copolymer is 2.55 and the obtained amounts of the PEtOx-*b*-PMMA too small under 20 % than the expectation. Therefore, the use of PEtOx macroinitiator was in difficulty to precisely controlled the block copolymer structure and it also limited to low yield.

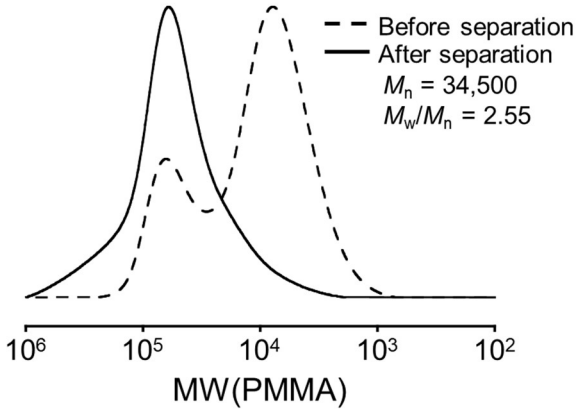

Fig. 2-4. SEC curves of before and after separation process. Dashed line is the mixture of PEtOx-*b*-PMMA and unreacted PEtOx. Solid line is the results of purified PEtOx-*b*-PMMA obtained after passing through HPLC; chloroform is used as eluent for the HPLC.

2.3.3. Synthesis of the O(Ox)nMA macromonomers

Panel (b) of scheme 2-1 depicted synthetic route for comb-type PMMA-*b*-P[O(Ox)$_n$MA]. As a first step, 2-ethyl-2-oxazoline is polymerized by LCROP described in experimental section. The chain lengths of the targeting oligomer were controlled by $[M]_0/[I]_0$ ratio. After the propagation, the living oligomer was capped by MAA/TEA complex and finally O(Ox)$_n$MA was obtained. Panel (a) of Fig 2-5 shows SEC curves, M_n, and M_w/M_n of two different length of O(Ox)$_n$MA. The M_n and M_w/M_n determined from each SEC curves were 800, 1.09, and 1,000, 1.12. Panel (b) of Fig. 2-5 shows representative ^{1}H NMR spectrum for O(Ox)$_n$MA. The polymerization degree (n) of the oxazoline unit for each O(Ox)$_n$MA

was determined as 9, 13. The value was determined by integral ratio between the signals of **e** and **b**, which are corresponding to methacrylate terminal groups and the methylene protons of oxazoline repeating units of ^{1}H NMR spectra for each O(Ox)$_n$MA.

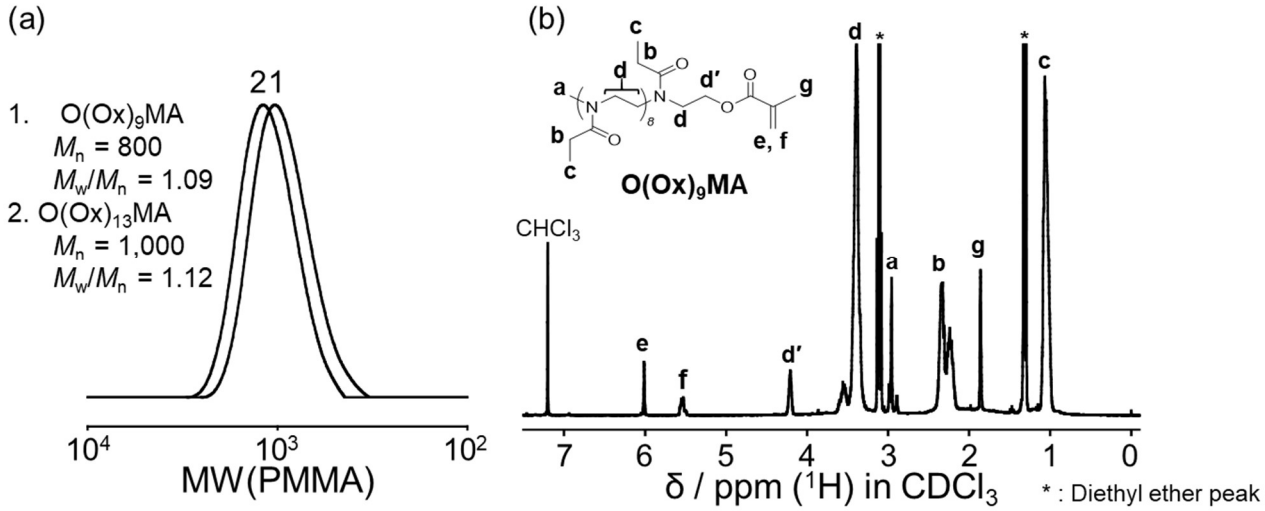

Fig. 2-5. (a) SEC curves for O(Ox)$_n$MA. Molecular weight was calibrated using PMMA standards, (b) ^{1}H NMR spectrum for O(Ox)$_9$MA (400 MHz, in $CDCl_3$). Asterisks represent residual diethyl ether.

2.3.4. ATRP of MMA using an EBiB initiator

A bromide terminated PMMA, which could act as a macroinitiator for ATRP, was synthesized. Also, this structure has further purpose to formed film states, target degree of polymerization was set at 200 units. Panel (a) of Fig. 2-6 shows monomer conversion and kinetic plot on polymerization time for the ATRP obtained in reaction mixture of MMA, EBiB, and CuBr/PMDETA complex catalyst. In the figure, $\ln([M]_0/[M]_t)$ versus polymerization times formed curvature plots. That is, at the beginning of the reaction, radical concentration was decreased, but it soon sustained constant value after 30 min of the polymerization time. Panel (b) of Fig. 2-6 shows dependence of M_n, and M_w/M_n on monomer conversion. The M_n was bigger than theoretical monomer conversion. This is because, the radical concentration was decreased at initial stage. But, the PMMA structure was well controlled with the M_w/M_n keeping smaller

than 1.20.

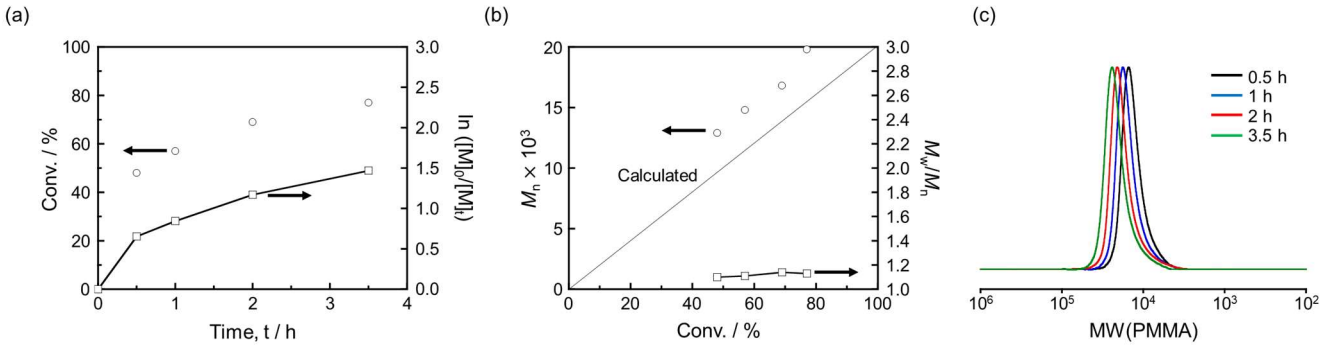

Fig. 2-6. Kinetic study of ATRP for PMMA obtained in $[MMA]_0 : [EBiB]_0 : [CuBr]_0 : [PMDETA]_0 = 200 : 1 : 1 : 1$ in anisole at 353 K; $[MMA]_0 = 4.62$ M. (a) MMA monomer conversion (round shape), and concentration of the remaining monomer in the reaction mixture (rectangular shape) on polymerization time. (b) Dependence of M_n (round shape), M_w/M_n (rectangular shape) on monomer conversion. (c) SEC curves of obtained PMMA on polymerization time. SEC: eluent THF; 1 mg·mL^{-1}; 313 K; PMMA standards.

2.3.5. ATRP of O(Ox)nMA using the PMMA macroinitiator

Amphiphilic type block copolymers, PMMA-*b*-P[O(Ox)MA], were synthesized by ATRP using O(Ox)$_n$MA macromonomer and PMMA macroinitiator. The detail procedure was explained above. Panel (a) of Fig. 2-7 shows monomer conversion and kinetic plot for the ATRP obtained in reaction mixture of O(Ox)$_{13}$MA, PMMA, and CuBr/PMDETA complex catalyst. The polymerization was stopped at the monomer conversion at 30 %. Panels (b, c) of Fig. 2-7 show M_n, M_w/M_n information and the SEC curve for the obtained PMMA-*b*-P[O(Ox)$_{13}$MA], and the M_w/M_n was still maintained around 1.32 with unimodal shape of the SEC curve, meaning that the block copolymer structure was well-controlled.

PMMA-*b*-P[O(Ox)$_9$MA] was also prepared in the same manner. And, the reaction was terminated at monomer conversion of around 30 %.

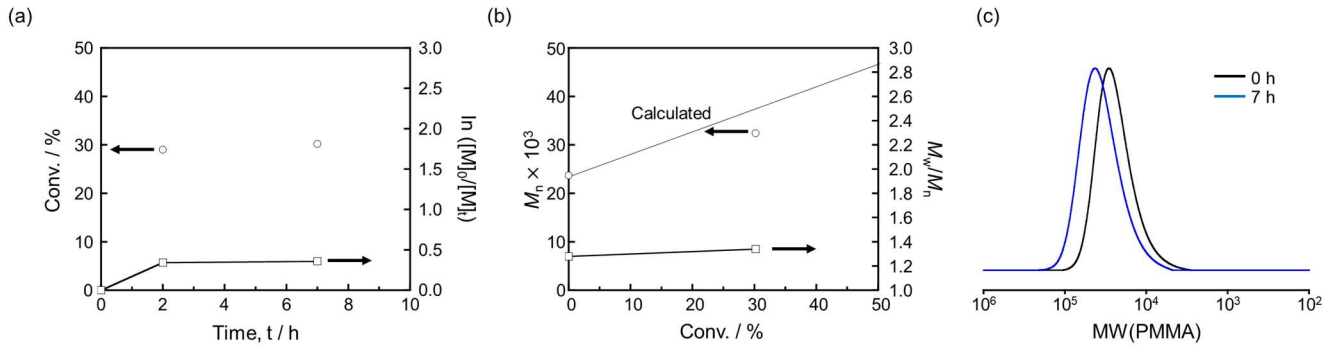

Fig. 2-7. Kinetic study of ATRP for PMMA-*b*-P[O(Ox)$_{13}$MA] obtained in [O(Ox)$_{13}$MA]$_0$: [PMMA]$_0$: [CuBr]$_0$: [PMDETA]$_0$ = 50 : 1 : 1 : 1 in DMF at 353 K; [O(Ox)$_{13}$MA]$_0$ = 333 mM. (a) O(Ox)$_{13}$MA monomer conversion (round shape), and concentration of the remaining monomer in the reaction mixture (rectangular shape) on polymerization time. (b) Dependence of M_n (round shape), M_w/M_n (rectangular shape) on monomer conversion. (c) SEC curves of obtained PMMA-*b*-P[O(Ox)$_{13}$MA] on polymerization time.

Panel (a) of Fig. 2-8 shows SEC curves for the obtained PMMA-*b*-P[O(Ox)$_9$MA], PMMA-*b*-P[O(Ox)$_{13}$MA], and starting PMMA macroinitiator. The curves were unimodal, and the peak was shifted to the higher molecular weight side compared to the one for PMMA. Panel (b) of Fig. 2-8 shows ^{1}H NMR spectra for PMMA and obtained PMMA-*b*-P[O(Ox)$_9$MA]. The degree of polymerization (*l*) of P[O(Ox)$_9$MA] block was by integral ratio between signals **b** and **j** corresponding to methylene group in the initiator and methyl protons in oxazoline repeating units, respectively. The *l* value for the PMMA-*b*-P[O(Ox)$_{13}$MA] also calculated as 11. The synthesized polymer structure information of M_n, M_w/M_n, and polymerization degree of each component are summarized in Table 2-2.

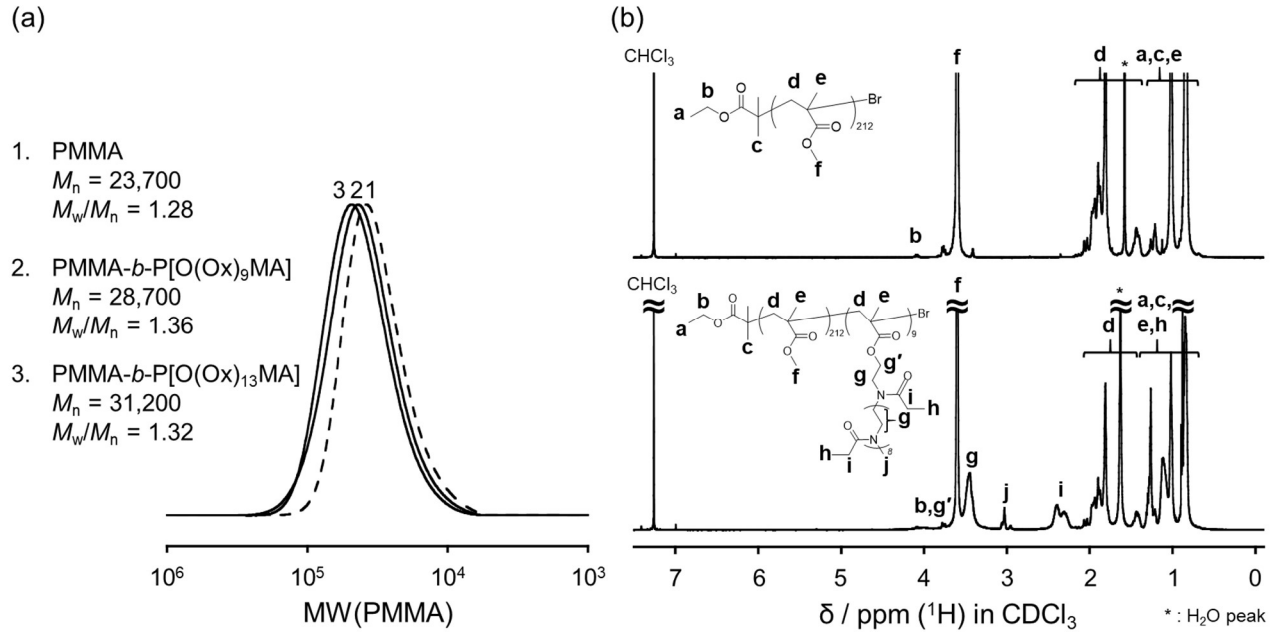

Fig. 2-8. (a) SEC curves for the products. Dashed line corresponding to PMMA macroinitiator and solid lines show PMMA-*b*-P[O(Ox)$_n$MA]. Molecular weight was calibrated using PMMA standards, (b) ^{1}H NMR spectra for PMMA (upper) and PMMA-*b*-P[O(Ox)$_9$MA] (lower) (400 MHz, in $CDCl_3$). Asterisks represent water peak.

2.3.6. ATRP of O(Ox)$_n$MA using the HEBiB initiator

Two kinds of bottlebrush P[O(Ox)$_n$MA] having different side chain length were synthesized based on LCROP followed by ATRP. Panel (a) of Fig. 2-9 shows SEC curves for the P[O(Ox)$_7$MA] and P[O(Ox)$_{19}$MA] showing unimodal shapes. Panel (b) of Fig. 2-9 shows representative ^{1}H NMR spectrum of P[O(Ox)$_7$MA]. All observable signals were well assigned with the respected polymer structure. Especially, broad signals were newly observed from 0.77 ~ 1.25 ppm, which the signals were corresponding with methyl methacrylate backbone structure. Also, checking the disappearance of signals corresponding to vinyl protons between 5.58 and 6.06 ppm, unreacted O(Ox)$_7$MA was successfully removed, that is, P[O(Ox)$_7$MA] was successfully obtained with high purity. However, end-group analysis was impossible because small intensity of signal for the HEBiB terminal group was hided around 4.02 ppm of signals for the P[O(Ox)$_7$MA] brush.

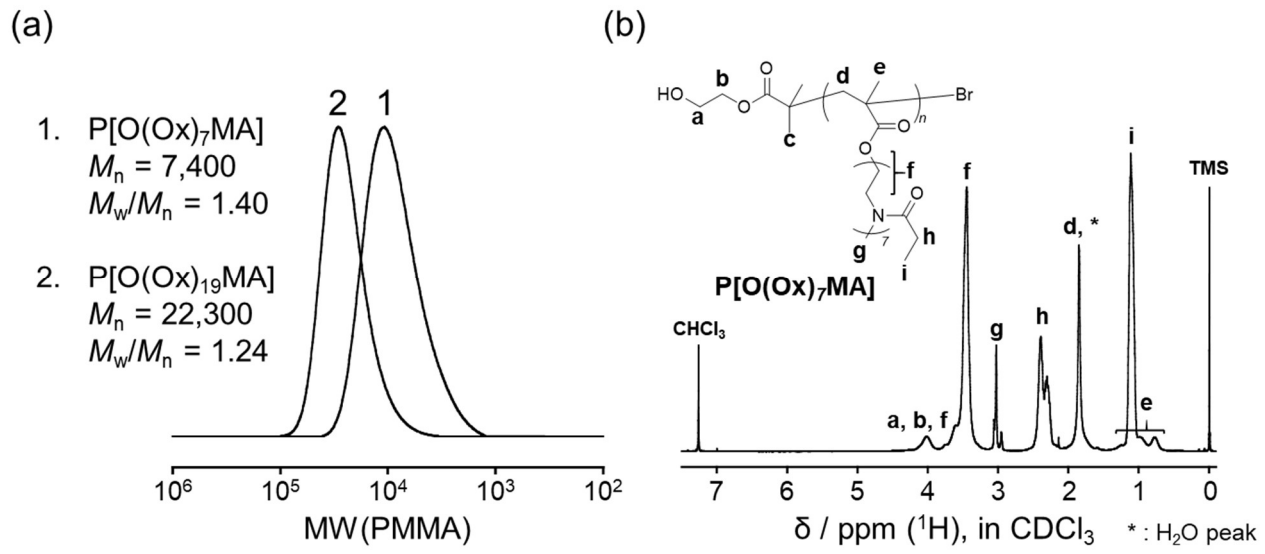

Fig. 2-9. (a) SEC curves of P[O(Ox)$_7$MA], and P[O(Ox)$_{19}$MA]. (b) A representative ^{1}H NMR spectrum of P[O(Ox)$_7$MA]. Asterisks represent water peak.

Table 2-2. Characteristics of the synthesized polymer.

Polymer	$M_{n,NMR}$[a)]	Degree of polymerization[a)]			M_n[b)]	M_w/M_n[b)]	T_g[c)] / K
		m	*l*	*n*			
PMMA-*b*-P[O(Ox)$_9$MA]	30,100	212	9	9	28,700	1.36	303, 365
PMMA-*b*-P[O(Ox)$_{13}$MA]	36,700	212	13	11	31,200	1.32	316, 383
P[O(Ox)$_7$MA]			12[b)]	7	7,400	1.40	300
P[O(Ox)$_{19}$MA]			13[b)]	19	22,300	1.24	312

[a)] Determined by ^{1}H NMR. [b)] A number-average molecular weight (M_n) and molecular weight distribution (M_w/M_n), where M_w is the weight-average molecular weight, determined by SEC with PMMA standards. [c)] Determined by DSC. *m*: Degree of polymerization of PMMA. *l*: Degree of polymerization of P[O(Ox)nMA]. *n*: Degree of polymerization of 2-ethyl-2-oxazoline at the side chain.

2.3.7. Bulk characterizations

Panel (a) of Fig. 2-10 shows DSC curves at the third heating cycle for the bulk samples of PMMA-*b*-P[O(Ox)$_9$MA], PMMA-*b*-P[O(Ox)$_{13}$MA], and PMMA. In the heating cycles for the block copolymers, unlike PMMA, two baseline shift were observed; that is, both block copolymers had lower and upper T_gs ($T_{g,l}$ and $T_{g,u}$), Comparing with T_g for PMMA, the upper T_g of block copolymers were clearly observed at lower temperature with much broader range of baseline shift. That is, partially miscible PMMA-rich

and P[O(Ox)$_n$MA]-rich domains were coexisted in bulk states.[2-13,14] The trends were also observed in SAXS profile shown in panel (b) of Fig. 2-5. In the SAXS profile of both block copolymers broad peaks were observed in the profiles. This means that the phase separation between the two P[O(Ox)$_n$MA] and PMMA block were considered to be not complete. However, the broad peaks were observed at scattering vectors (q) of 0.172 nm^{-1} for PMMA-*b*-P[O(Ox)$_{13}$MA] and 0.181 nm^{-1} for PMMA-*b*-P[O(Ox)$_9$MA] in each of the one-dimensional SAXS profiles. The denoting *d*-spacing for the block copolymers were 36.5 nm for PMMA-*b*-P[O(Ox)$_{13}$MA] and 34.7 nm for PMMA-*b*-P[O(Ox)$_9$MA]. From the SAXS results, the block copolymers seem most likely to form a micelle-like structures in bulk states.

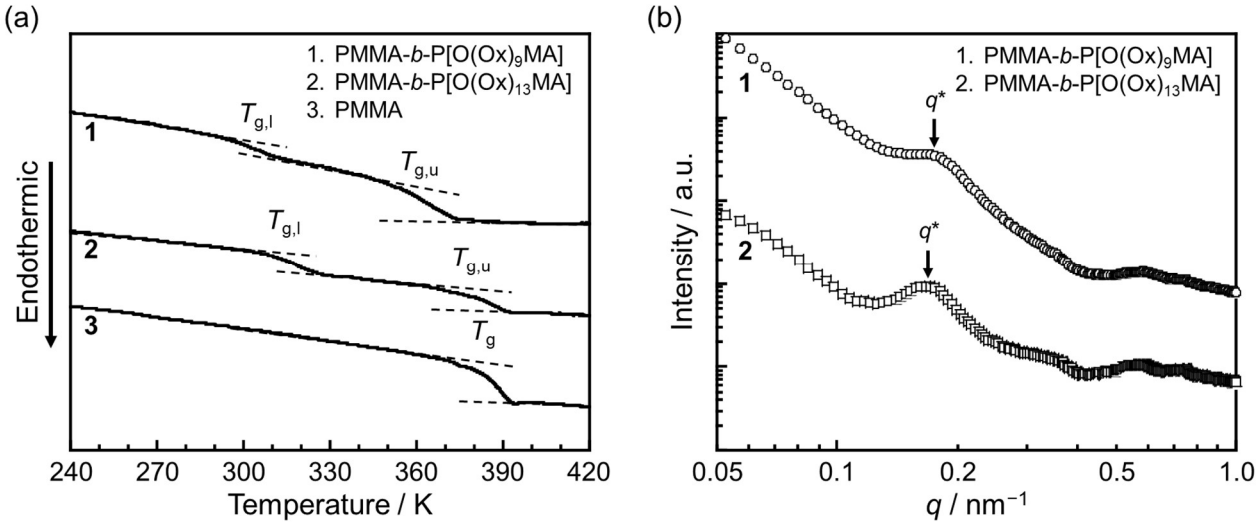

Fig. 2-10. (a) DSC curves for block copolymers and PMMA obtained from the third heating cycle. Dashed lines are the baselines. (b) One-dimensional SAXS profiles for the block copolymers.

2.4. Summary

In this chapter, amphiphilic block copolymers composed of hydrophilic PEtOx and hydrophobic PMMA was planned to be synthesized by controlled polymerization methods. At first, PEtOx-*b*-PMMA was polymerized from bromoisobutyrate functionalized PEtOx macro-initiator. However, poor purity of the initiator and the lower initiation efficiency of the polymerization made it difficult to obtained the well-controlled block copolymer with high yield. As the alternative synthetic route, O(Ox)$_n$MA macromonomer were prepared by LCROP. Subsequently, a series of well-defined PMMA-*b*-P[O(Ox)$_n$MA] were successfully synthesized through ATRP using the O(Ox)$_n$MA macromonomer with PMMA macroinitiator. Also, well-controlled bottlebrush P[O(Ox)$_n$MA] homopolymers were successfully prepared in a similar manner. As the next steps of the synthesis, stable surface are going to be establish using the PEtOx derivatives in water environment, and then, interfacial aggregation states of the oxazoline units will further characterized.

2.5. References

2-1) Tanaka, K.; Takahara, A.; Kajiyama, T. Effect of Polydispersity on Surface Molecular Motion of Polystyrene Films. *Macromolecules* **1997,** *30,* 6626.

2-2) Matsuno, H.; Irie, S.; Hirata, T.; Matsuyama, R.; Oda, Y.; Masunaga, H.; Seki, Y.; Aoshima, S.; Tanaka, K. Heterogeneous Adhesion of Cells on Polymer Surfaces with Underlying Amorphous/crystalline Phases. *J. Mater. Chem. B.*, **2018**, *6(6)*, 903.

2-3) Glassner, M.; Vergaelen, M.; Hoogenboom, R. Poly(2-oxazoline)s: A comprehensive overview of polymer structures and their physical properties. *Polym. Int.*, **2018**, *67*, 32.

2-4) Penczek, S. Cationic Ring-Opening Polymerization (CROP) Major Mechanistic Phenomena. *J. Polym. Sci. Part A: Polym. Chem.*, **2000**, *38*, 1919.

2-5) Drain, B. A.; Becer, C. R. Synthetic Approaches on Conjugation of Poly(2-oxazoline)s with Vinyl Based Polymers. *Europ. Polym. J.*, **2019**, *119*, 344.

2-6) Krieg, A.; Weber, C.; Hoogenboom, R.; Becer, C. R.; Schubert, U. S. Block Copolymers of Poly(2-oxazoline)s and Poly(meth)acrylates: A Crossover between Cationic Ring-Opening Polymerization (CROP) and Reversible Addition−Fragmentation Chain Transfer (RAFT). *ACS Macro Lett.*, **2012**, *1*, 776.

2-7) Weber, C.; Krieg, A.; Paulus, R. M.; Lambermont-Thijs, H. M. L.; Becer, R.; Hoogenboom, R.; Schubert, U. S. Thermal Properties of Oligo(2-ethyl-2-oxazoline) Containing Comb and Graft Copolymers and their Aqueous Solutions. *Macromol. Symp.*, **2011**, *308*, 17.

2-8) Becer, C. R.; Paulus, R. M.; Hoppener, S.; Hoogenboom, R.; Fustin, C. A.; Gohy, J. F.; Schubert, U. S. Synthesis of Poly(2-ethyl-2-oxazoline)-b-poly(styrene) Copolymers via a Dual Initiator Route Combining Cationic Ring-Opening Polymerization and Atom Transfer Radical Polymerization. *Macromolecules*, **2008**, *41*, 5210.

2-9) Gieseler, D.; Jordan, R. Poly(2-oxazoline) Molecular Brushes by Grafting through of Poly(2-

oxazoline) methacrylates with Aquous ATRP. *Polym. Chem.*, **2015**, *6*, 4678.

2-10) Urien, M.; Erothu, H.; Cloutet, E.; Hiorns, R. C.; Vignau, L.; Cramail, H. Poly(3-hexylthiphene) Based Block Copolymers Prepared by "Click" Chemistry. *Macromolecules*, **2008**, *41*, 7033.

2-11) Xia, J.; Matyjaszewski, K. Controlled/"Living" Radical Polymerization. Atom Transfer Radical Polymerization Using Multidentate Amine Ligands. *Macromolecules*, **1997**, *30*, 7697.

2-12) Tsai, T. Y.; Huang, C. F. Data in Support of Dual-Functionalized Cellulose Nanofibrils Prepared through TEMPO-Mediated Oxidation and Surface-Initiated ATRP. *Data Brief*, **2015**, *3*, 195.

2-13) Zeng, J. B.; Zhu, Q. Y.; Lu, X.; He, Y. S.; Wang, Y. Z. From Miscible to Partially Miscible Biodegradable Double Crystalline Poly(ethylene succinate)-*b*-poly(butylene succinate) Multiblock Copolymers. *Polym. Chem.*, **2012**, *3*, 399.

2-14) Abolhasani, M. M.; Guo, Q.; Jalali-Arani, A.; Nazockdast, H.; Poly(vinylidene fluoride)-acrylic Rubber Partially Miscible Blends: Phase Behavior and Its Effects on the Mechanical Properties. *J. Appl. Polym. Sci.*, **2013**, *130*, 1247.

Chapter 3. Water-induced surface segregation in a thin film of an amphiphilic type poly(2-ethyl-2-oxazoline) derivative

3.1. Background

Inhibition of indiscriminate adsorption of cell, protein, or microorganism is pivotal important to the efficacy and safety of biomedical devices. Since, Dejardin *et al.* firstly reported poly(2-methyl-2-oxazoline)-*block*-poly(ethylene oxide)-*block*-poly(2-methyl-2-oxazoline) (PMeOx-*b*-PEO-*b*-PMeOx) triblock copolymer highly suppressed fibrinogen protein adsorption in 1989,[3-1)] there have been a variety of effort to prove biocompatibility of poly(2-oxazoline).[3-3~6)] In particular, as described in the Chapter 1, PEtOx shows outstanding water solubility and bio-inert properties. At the same time, however, the high water solubility somehow leaves homework on how to construct sustainable polymer surface in water.[3-7~12)] Typical methods to form sustainable PEtOx surface is covalently immobilizing the PEtOx chain on solid substrates. There are two general types of grafting methods: grafting to method, and grafting from method. The grafting-to method refers to a method of directly anchoring polymers to a substrate, and it has an advantage of obtaining highly controlled polymer brushes.[3-13,14)] In some previous studies, U.S. Schubert *et al.* attached the PEtOx brush by epoxide ring-opening reaction between an amine-end functionalized PEtOx and a glass substrate modified with glycidyl ether silane.[3-9)] Also, Wang *et al.* successfully connected the mono thiol-terminated poly(methacrylic acid)-*graft*-poly(2-methyl-2-oxazoline) copolymer onto gold substrate through aminolysis reaction.[3-10)] The other typical method is grafting-from methods. In this method, polymer chain starts to grow up from the substrates which were preferentially connected with functionalities capable of polymerization process. Unlike the grafting-to method, grafting-from method binds small molecules to the surface, that is, a high density of polymer brushed can be formed at the substrates.[3-15,16)] However, if the brushes keep growing up, control

of the polymerization become difficult. Especially, in the case of PEtOx brush by grafting-from methods, the requirement for the inert polymerization condition for the cationic polymerization makes the process more difficult.[3-16] As described, it is possible to anchor the PEtOx to the solid substrate through the grafting methods, but the process quite require several pre-treatment process and still limited to specific solid substrates like silicon wafers or metal substrates, and the methodology is hard to scale up for the industrial level in present.

In this chapter, using the amphiphilic PMMA-*b*-P[O(Ox)MA] copolymer synthesized in the last Chapter 2, I plan to prepare a water-stable thin film that has escaped from the conventional chemical bonding method. Then, the aggregation behavior of the hydrophilic P[O(Ox)MA] block to construct the P[O(Ox)MA]/water interface are going to be characterized, and then, the effect of the aggregation structure on bio-inert properties will be evaluated. Fig. 3-1 shows schematic illustration for the construction of the bio-inert interface using thin film of PMMA-*b*-P[O(Ox)MA].

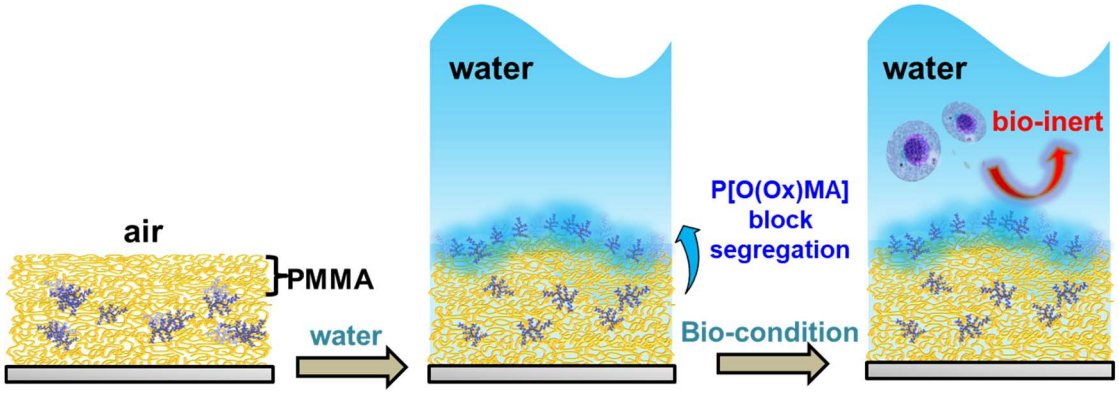

Fig. 3-1. A schematic illustration of formation of the P[O(Ox)MA] segregation layer in a PMMA-*b*-P[O(Ox)MA] film at the water interface, which is resulting in construction of the bio-inert interface.

3.2. Experimental

3.2.1. Materials

PMMA-*b*-P[O(Ox)MA] were synthesized by combination of LCROP and ATRP using PMMA macroinitiator as described in previous chapter. Table 3-1 summarizes the structural characteristics of the synthetized polymers used in this study.

Table 3-1. Characteristics of the synthesized polymers.

Polymer	$M_{n,NMR}$[a)]	Degree of polymerization[a)]			M_n[b)]	M_w/M_n[b)]	T_g[c)] / K
		m	*l*	*n*			
PMMA-*b*-P[O(Ox)MA]	30,100	212	9	9	28,700	1.36	303, 365
PMMA	21,500	212	–	–	23,700	1.28	389

[a)] Determined by ^{1}H NMR. [b)] Determined by SEC with PMMA standards. [c)] Determined by DSC.

3.2.2. Thin film preparation

First, various solid substrates such as Si wafers (Matsuzaki Seisakusho Co., Ltd., Fukui, Japan) and borosilicate glasses (Matsunami Glass Ind., Ltd., Osaka, Japan), were hydrophobized with chloro-(decyl)dimethylsilane through vacuum-deposition. Hydrophobization was confirmed based on water contact angles against the treated substrates. The values were approximately 103˚ and 100˚, respectively, for the Si wafer and the borosilicate glasses.

Thin films of the PMMA-*b*-P[O(Ox)MA] were prepared on the hydrophobized substrates by a spin-coating method using a 1H-D7 spin-coater (MIKASA Co., Ltd., Tokyo, Japan) at 2000 rpm for 120 s. As a reference, thin films of PMMA were also prepared in the same manner on the solid substrate without hydrophobization. Then, the films were annealed at ($T_{g,u}$ + 20) K under vacuum for 12 h.

3.2.3. Surface aggregation states of the block copolymer film

The surface morphology of block copolymer films was observed by atomic force microscopy (AFM, Cypher ES, Asylum Research, an Oxford Instruments Co., Santa Barbara, CA, US) under air and in water at 298 K. To evaluate surface hydrophilicity, static contact angles at the film surfaces were estimated under air and in water. The measurements were performed using a DropMaster 500 (Kyowa Interface Science Co., Ltd., Niiza, Saitama, Japan). As a probe, 1 μL of ultrapure water and 2 μL of air bubble were used, respectively.

The surface chemical composition of the thermal annealed film surfaces was estimated by angular-dependent X-ray photoelectron spectroscopy (AD-XPS) using a PHI 5000 VersaProbe III (ULVAC-PHI, INC., Chigazaki, Kanagawa, Japan) with an anode source of Al-Kα operated at 15 kV and 25 W. The emission angles were set in a range of 15˚ to 90˚. The XPS signals were calibrated to a binding energy of 285.0 eV for neutral carbons. For evaluation of the reorganized surface chemical composition driven by water, freeze-dried films of PMMA-*b*-P[O(Ox)MA] and PMMA were prepared by immersing them into water at RT for 24 h, subsequently, lyophilizing the surfaces. The measurement was conducted in the same condition for the thermal annealed film surfaces.

To correlate the AD-XPS results with the real analytical depth, the inelastic mean free path (λ) was calculated by following Ashley models:[3-17)]

$$\lambda = \frac{M}{\rho n} E_k / (13.6 \ln(E_k) - 17.6 - 1400/E_k) \quad (3\text{-}1)$$

where, M is the molecular weight of repeating unit, ρ is the density of the polymer, n is the number of valance electrons in the repeating units and, E_k is the kinetic energy obtained using the Al-Kα source.

3.2.4. Film stability in water

Because P[O(Ox)MA] is highly water soluble, the stability of PMMA-*b*-P[O(Ox)MA] thin film in water was evaluated by static contact angle measurement at RT in water using 2 μL of air bubble as a probe. The air bubble contact angles (θ_a) were recorded in every 1 h until 24 h in water.

3.2.5. Density profile of the block copolymer film

The density profile of the block copolymer film along the depth direction from the film surface was evaluated by Soft Interface Analyzer (SOFIA) at the Materials and Life Science Experimental Facility (MLF), Japan Proton Accelerator Research Complex (J-PARC). The block copolymer film was spin-coated on 60 × 60 × 8 mm size of the hydrophobized quartz substrate. The water droplet contact angle value of the hydrophobized quartz substrates was around 96˚. First, the measurement was conducted under ambient conditions. Then, the film was contacted with deuterated water (D_2O) in a Teflon-made reservoir for at RT for 4 h, which was enough to reach a quasi-equilibrium state in D_2O. The measurement was conducted in D_2O again in a same manner. The incident angles of the neutron beam were 0.3, 0.75, and 1.8˚ against the film surface. The reflectivity was calculated on the basis of a model scattering length density (b/V) profile along the depth direction using the error function. For the calculation, Motofit program, which is provided from Dr. Andrew Nelson, was used. The (b/V) values of PMMA, SiO_2, and D_2O used for the calculations were 1.04×10^{-4}, 3.48×10^{-4}, and 6.36×10^{-4} nm^{-2}, respectively.

3.2.6. Cell adhesion test

Swiss mouse embryo fibroblasts NIH3T3 (RCB1862, RIKEN BRC Cell Bank, Tsukuba, Ibaraki, Japan) were used for the investigation of cell adhesion behavior. The detail procedures were as follows. First, the block copolymer films spin-coated on hydrophobized borosilicate glass substrates were

immersed into water in 24-well plates (Corning Incorporated, Corning, New York, United States) composed of PS at RT for 24 h. After removing water, the 4×10^4 cells·cm^{-2} of cell suspension in Dulbecco's modified Eagle's medium (DMEM) containing 10% of fetal bovine serum (FBS, Life Technologies Japan, Ltd., Tokyo, Japan) were added into each plates and incubated at 310 K for 12 h. Cell adhesion behaviors at each film surfaces were observed by using a phase-contrast microscope (BZ-8100, Keyence Co., Osaka, Japan) as a function of culturing-time of 0 h, 3 h, 6 h, 9 h, and 12 h. After the cell culturing for 12 h, weakly adhered or suspended cells were removed by washing with phosphate buffered saline (PBS, Takara Bio, Inc., Shiga, Japan) several times. Then, the adherent cells were fixed by immersion the surface in 2 % (vol./vol.) of glutaraldehyde/PBS at 277 K for 20 min. The fixed cells were stained by 0.01 wt% crystal violet/mixed solvent of methanol/water (1/200 (vol./vol.)). The number and morphology of adherent cells were estimated by using the phase-contrast microscope.

3.2.7. Protein adsorption test

10% FBS in DMEM was used as a protein sample solution. Before the test, the film surfaces were immersed in water at RT for 24 h. After removing the water, 10% FBS in DMEM was added at each sample, subsequently, incubated at 310 K for 1 h. Then, the film surfaces were gently washed by PBS. Subsequently, adsorbed proteins were detached in 1wt% of aqueous sodium dodecyl sulfate (SDS) solution following by sonication at 313 K for 20 min. The concentration of detached protein was evaluated by the microplate procedure of a micro-bicinchoninic acid protein assay kit (micro-BCA, Thermo Fisher Scientific K.K., Tokyo, Japan), which also calibrated with 9 different concentration of bovine serum albumin standards. The light absorbance at the wavelength of 560 nm of the sample solution was detected using a plate reader (INFINITE 200, Tecan Japan Co., Ltd., Kanagawa, Japan). PMMA films and polyethylene terephthalate (PET) sheets (Toray Industries, Inc., Tokyo, Japan) were also used as references.

3.3. Results and discussion

3.3.1. Surface aggregation states of the block copolymer film

The surface aggregation states of the films were examined by AFM in conjunction with static contact angle measurement. Fig. 3-2 shows AFM (a, b) height and (c, d) phase images for (a, c) PMMA-*b*-P[O(Ox)MA], and (b, d) PMMA films. The root-mean-square surface roughness (R_{RMS}) values for the block copolymer and PMMA films were 0.39, 0.30 nm, respectively. This result indicates that the films were sufficiently flat to be applicable for following surface-sensitive characterization. And, there were no specific features in the phase images for block copolymer film surface as well as the PMMA film surface. That is, the outermost surface of the block copolymer film was covered with a component. To identify which component covers the outermost surface, static contact angle measurement under air were conducted using water droplet. As a result, both films show almost same water droplet contact angle value; PMMA-*b*-P[O(Ox)MA] for 75.5 ± 0.8°, and PMMA for 75.0 ± 0.6°. This implies that outermost surface at PMMA-*b*-P[O(Ox)MA] film is mainly covered with PMMA block.

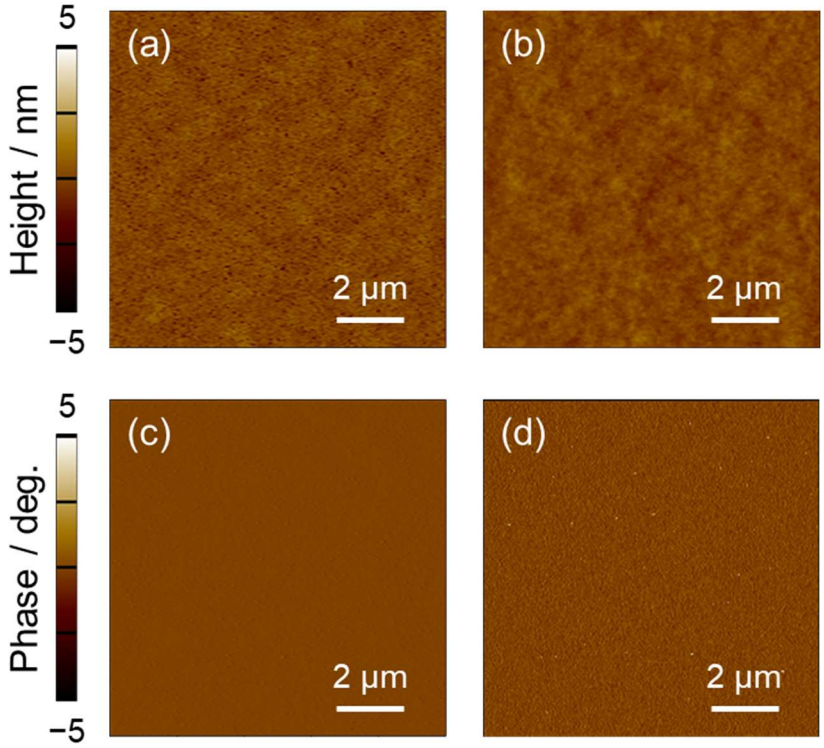

Fig. 3-2. (a, b) AFM height and (c, d) phase images for (a, c) PMMA-*b*-P[O(Ox)MA] and (b, d) PMMA films under air.

Fig. 3-3 shows AFM (a, b) height and (c, d) phase images for (a, c) PMMA-*b*-P[O(Ox)MA], and (b, d) PMMA films after immersing the films in water. After contacting with water, the outermost surface of PMMA-*b*-P[O(Ox)MA] film became clearly rough with a R_{RMS} of 1.39 nm; whereas that for PMMA film was unchangeable. These results indicate that surface structure rearrangement was greatly occurred on the block copolymer film, even though there was still small contrast in the phase image.

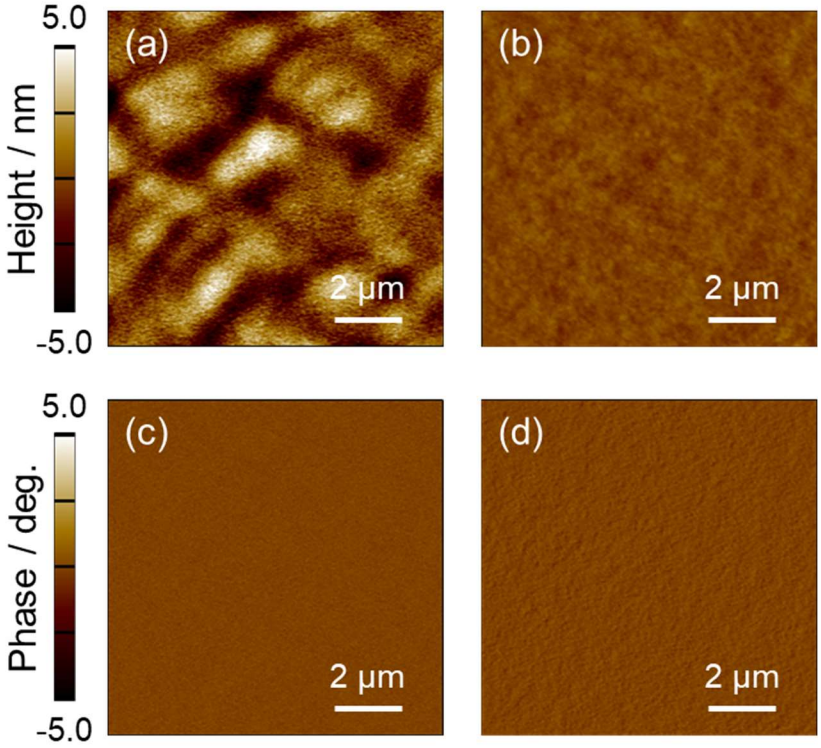

Fig. 3-3. (a, b) AFM height and (c, d) phase images for (a, c) PMMA-b-P[O(Ox)MA] and (b, d) PMMA films in water.

To trace the surface structure reorganization occurred in water, static contact angle measurement was also conducted using air bubble as a probe in water. After immersing the film into water, air bubble contact angles on the films show clear differences that the contact angle on the block copolymer film was 131.6 ± 0.7°, and that for PMMA film was 114.0 ± 0.5° in 24 h. The clear differences of the surface hydrophilicity imply that, P[O(Ox)MA] block in the block copolymer film was suspected to be emerged toward water interface even though the block copolymer film surface was firstly covered by PMMA block.

To support the above hypothesis, the surface chemical composition was examined by AD-XPS. Panels (a, b) of Fig. 3-4 show representative XPS N_{1s} and C_{1s} spectra for PMMA-*b*-P[O(Ox)MA] film in initial thermal annealed state at φ_e of 15, 30, 90°, and representative PMMA spectrum. In the case of the N_{1s} spectra shown in panel (a) of Fig. 3-4, a nitrogen peak signal corresponding to tertiary amine (N–C=O) was observed at 400 eV acquired at φ_e of 30, 90°, whereas the signal was not appeared at φ_e of 15°.

Because the nitrogen atoms are only composed in P[O(Ox)MA] block, it is apparent that outermost surface area covered with PMMA block, not with P[O(Ox)MA] block. The results were also confirmed by using C_{1s} spectra shown in panel (b) of Fig. 3-4. While the C_{1s} signals at φ_e of 30, 90° could be decomposed to the five contributions such as neutral (C–C/C–H), amine (C–N), ether (C–O), amide (N–C=O), and ester (O–(C=O)) carbons, the signals at φ_e of 15° was almost identical with homo PMMA, which peaks only comprised with three C_{1s} peaks like neutral, ether, and ester peaks. Open circles in panel (c) of Fig. 3-4 show integral intensity ratio of all nitrogen to all carbon peaks (I_{N1s}/I_{C1s}) dependence on sin φ_e. The relationship between I_{N1s}/I_{C1s} and real analytical depth was estimated by fitting the experimental data on the basis of a model concentration profile. Photoelectrons cannot travel for a long distance in matter and the number of photoelectrons detected exponentially decays along the depth direction. Thus, the I_{N1s}/I_{C1s} at φ_e is given by;

$$\frac{I_{N1s}}{I_{C1s}} = \frac{\int_0^\infty [n_N(z)\cdot\exp(-z/\lambda_N \sin\varphi_e)]dz}{\int_0^\infty [n_C(z)\cdot\exp(-z/\lambda_C \sin\varphi_e)]dz} \quad (3\text{-}2)$$

where z is the depth, λ_i and $n_i(z)$ are the inelastic mean free path of photoelectrons and atomic fraction of component i, respectively. Also, the curve fitting was conducted by assuming the surface consisted of two uniform over-layer model as follows.

$$n_N(z) = \begin{cases} n_{N,s} \ (z < z_i) \\ n_{N,\infty} \ (z > z_i) \end{cases} \quad (3\text{-}3)$$

where the $n_{N,s}$ and $n_{N,\infty}$ are the nitrogen atomic fraction at the outermost surface and in the bulk, respectively. The solid line was the best-fit based on model depth profile of nitrogen atomic fraction (n_N) shown in panel (d) of Fig. 3-4 and the obtained fitting parameter of n_s and z_i were 0.01, and 5.3 nm, respectively. The results show that the PMMA wetting layer with a thickness of approximately 5 nm was formed at the thermal annealed film surface.

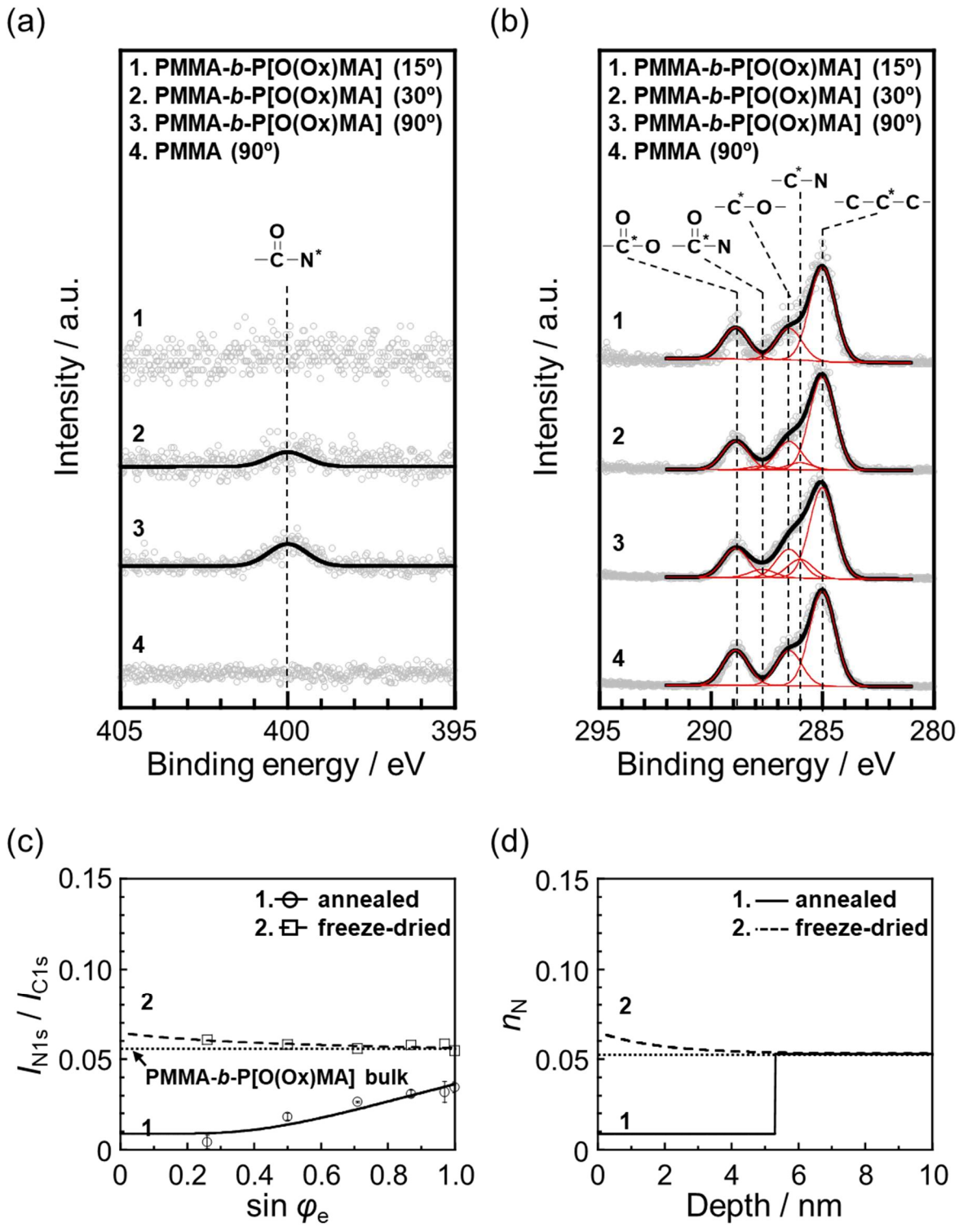

Fig. 3-4. (a, b) XPS (a) N_{1s} and (b) C_{1s} spectra for the PMMA-*b*-P[O(Ox)MA] at various φ_es of 15, 30, 90°, and that for reference PMMA at φ_e of 90°. Open circles denote the experimental data and solid lines are curve fitting results. The black solid line in panel (b) was separated to the red solid lines. (c) Sin φ_e dependence of the integral intensity ratio (I_{N1s}/I_{C1s}) for initial thermal annealed and freeze-dried PMMA-*b*-P[O(Ox)MA] films. Circles and squares denote for the thermal annealed and freeze-dried films, respectively, and solid and dashed lines show the best-fits results using model depth profiles shown in (d). Dotted lines in (c) and (d) represent the calculated bulk value (n_N = 0.053) based on the chemical structure confirming by ^{1}H NMR.

To tracing surface reorganization of the films in water, AD-XPS analyses were also performed on freeze-dried PMMA-*b*-P[O(Ox)MA] films. Panels (a, b) of Fig. 3-5 show the XPS N_{1s} and C_{1s} spectra of the freeze-dried block copolymer film surface at the various φ_es and the representative spectrum for the reference PMMA film. Unlike spectra obtained in the thermal annealed film, both N_{1s} and C_{1s} signals originated oxazoline units were clearly observed at the all measurement angle. Open squares in panel (c) of Fig. 3-4 indicate the I_{N1s}/I_{C1s} against sin φ_e. Then, using the experimental results curve fitting was conducted in the similar manner. For the curve fitting, the two uniform over-layer model was applied at first, however, the model could not fit the data well. Then, another model composition profile using the additional fitting parameter of decay length (ξ) was applied. The alternative model profile was shown as follow.

$$n_{\mathrm{N}}(z) = n_{\mathrm{N},\infty} + \left(n_{\mathrm{N,s}} - n_{\mathrm{N},\infty}\right) \cdot \exp(-z/\xi) \qquad (3\text{-}4)$$

The dashed curve in panel (c) of Fig. 3-4 is the best fit result based on the model n_N profile in panel (d) of Fig. 3-4. The values of $n_{\mathrm{N,s}}$ and ξ were estimated to be 0.065 and 1.8 nm, respectively. The results suggested that the P[O(Ox)MA] block became enriched at the water interface and possibly formed the swollen layer.

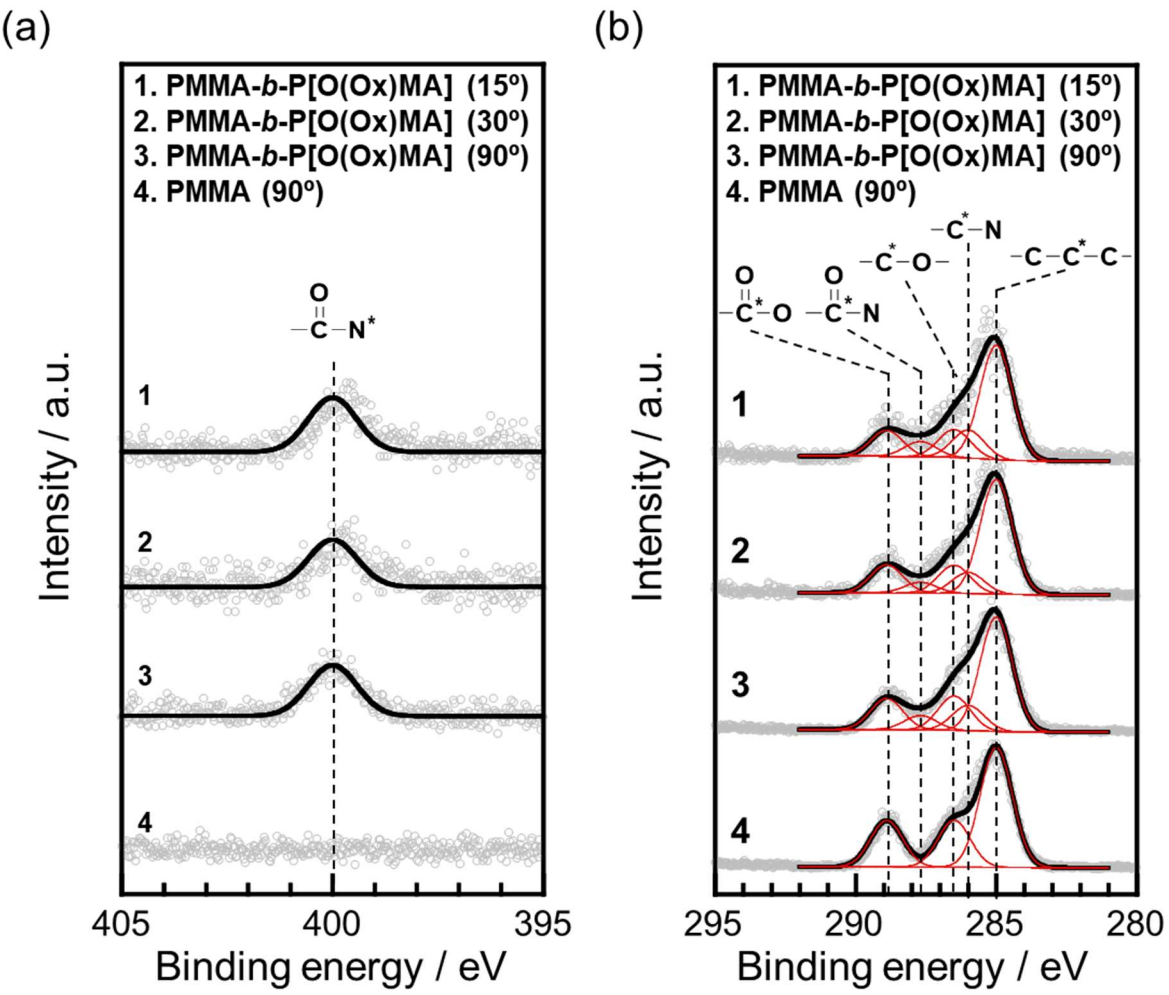

Fig. 3-5. (a, b) XPS (a) N_{1s} and (b) C_{1s} spectra for the freeze-dried films at various φ_es. Open symbols denote the experimental data and solid curves are fitting results. The black solid line in panel (b) is the composite of the all red solid lines.

3.3.2. Film stability in water

To evaluate the thin film stability in water, air bubble contact angle measurement against film surface was conducted to monitor whether surface hydrophilicity keep maintained over the time. Fig. 3-6 shows immersion time dependence of the air bubble contact angle for the PMMA-*b*-P[O(Ox)MA] and PMMA in water. The initial values for the PMMA-*b*-P[O(Ox)MA] and PMMA film surfaces were 133.0 ± 1.1 and 112.1 ± 0.5°, respectively. After 24 h of immersion time, the contact angle values were 131.6 ± 0.7 and 114.0 ± 0.5°, that is, surface hydrophilicity especially at the block copolymer film surfaces keep

unchanged within experimental error. This result indicates that the block copolymer film is stable without detachment or dissolution in water.

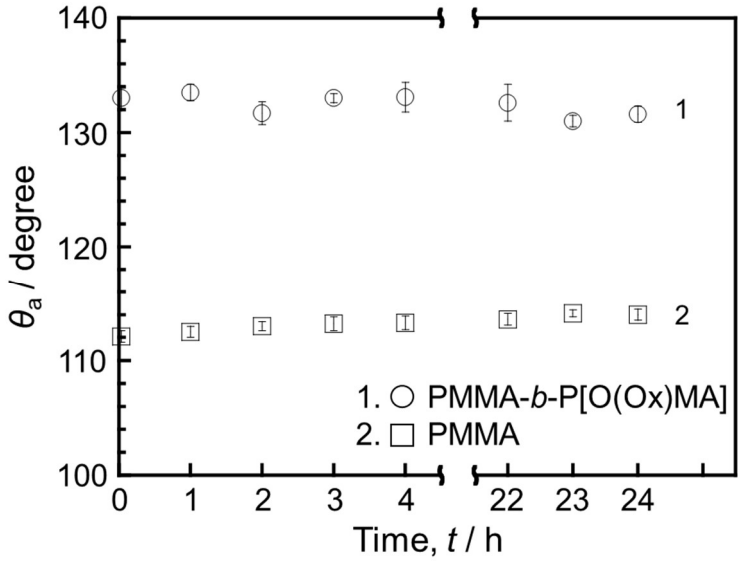

Fig. 3-6. Time dependence of air bubble contact angle (θ_a) of the PMMA-*b*-P[O(Ox)MA], and PMMA film surface. Plots shows the average and standard deviations. Initial value was recorded in 2 min, and, the measurement was conducted in every 1 h up to 24 h.

3.3.3. Density profiles of the block copolymer film

To obtain better understanding of interfacial aggregation states facing with water, NR measurements were carried out for the PMMA-*b*-P[O(Ox)MA] film. Open symbols in panel (a) of Fig. 3-7 shows the reflectivity for the PMMA-*b*-P[O(Ox)MA] film as a function of q along the depth direction (q_z) in air and deuterated water (D_2O). The red solid curves were the calculated reflectivity on the basis of the model scattering length density (b/V) profiles shown in panel (b) of Fig. 3-7. To simplify a fitting model, it was assumed that the block copolymer film was consisted by 3 layers: segregation layer at air or water interface, bulk layer, and segregation layer at substrate interface. Dashed line in panel (b) of Fig. 3-7 was the (b/V) profile in D_2O. Comparing with the profile in the air shown as a solid line of Fig. 3-7(b), thickness of the film increased from 75.3 to 88.1 nm. Also, (b/V) values acquired in all film thickness range increased in D_2O and these implied that the D_2O were well penetrated inside the film. In the profile acquired in D_2O, the (b/V) value of the bulk layer was 1.35. Taking into account that the (b/V) values of

the D_2O and polymer bulk were 6.36 and 0.99, respectively, the volume fraction of the D_2O (Φ_{D2O}) in the bulk layer were calculated to 7 vol/vol % by using following equation.

$$(b/V)(z) = \Phi_{D2O} \cdot (b/V)_{\mathrm{D2O}} + (1 - \Phi_{D2O}) \cdot (b/V)_{\mathrm{polymer}} \quad (3\text{-}5)$$

where z, Φ_{D2O}, and $(b/V)_{\mathrm{i}}$ were the depth, volume fraction of the D_2O at the depth position, and (b/V) value of *i* component. Also, the most important feature was that the increment of the (b/V) was formed much broader at the water interface, comparing with the (b/V) decrement at the air interface. That is, the outermost region of the block copolymer film was diffused by D_2O at the water interface. Also, the Φ_{D2O} gradually increased from 7 to 63 vol/vol % in the segregation layer at the water interface. In a similar manner, D_2O molecules were accumulated at the solid interface, and the Φ_{D2O} gradually increased from 7 to 86 vol/vol % in the segregation layer at the solid substrate.

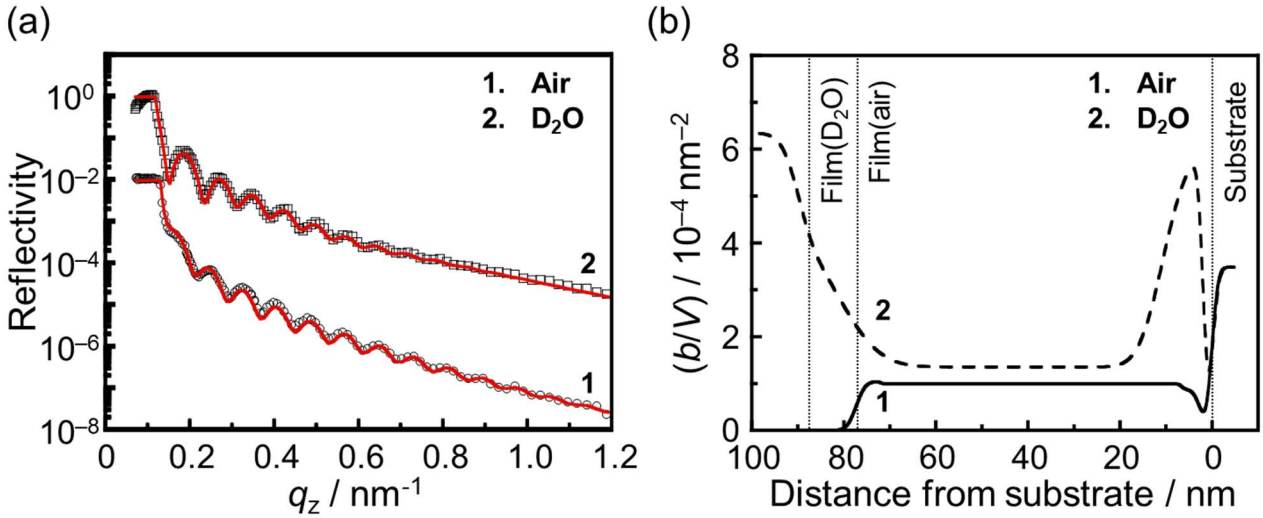

Fig. 3-7. (a) NR curves for the thin film of PMMA-*b*-P[O(Ox)MA] in air and D_2O. Open symbols are corresponding the experimental data, and red solid lines are the calculated reflectivity results on the basis of the (b/V) profile of the film shown in (b).

3.3.4. Cell adhesion test

Finally, adhesion behaviors of NIH3T3 fibroblasts on PMMA-*b*-P[O(Ox)MA] and PMMA films were chased to evaluate bio-inert properties of the films. Panels (a-f) of Fig. 3-8 shows phase-contrast microscopic images for the cell cultured on both film surface as a function of culturing time. After 6 h

of cell culture, a clear difference in adhesion behavior was observed between the two film surfaces. A number of cells strongly adhere and spread out at the PMMA film. However, most of cells maintained the original spherical shape and some cells formed aggregation at the block copolymer film. Panels (g, h) of Fig. 3-8 are the surface images after washing/fixation. The aggregation of the cells and weekly adhered cells were easily removed on the block copolymer films; whereas spread cells on PMMA films were still strongly adhered. Panel (i) of Fig. 3-8 shows the number of adhered cells (N_{cell}) on the films. The N_{cell} value for the PMMA-*b*-P[O(Ox)MA] films were only 20 % comparing with that for PMMA films. Panels (a, b) of Fig. 3-9 shows percent abundance of the adherent cell areas on both films. From the histogram, it was also known that the adherent cells on block copolymer film was harder to spread out comparing with that on PMMA film. And the results of the number and morphology of the adherent cells indicate that the PMMA-*b*-P[O(Ox)MA] film exhibited good suppression of cell attachment.

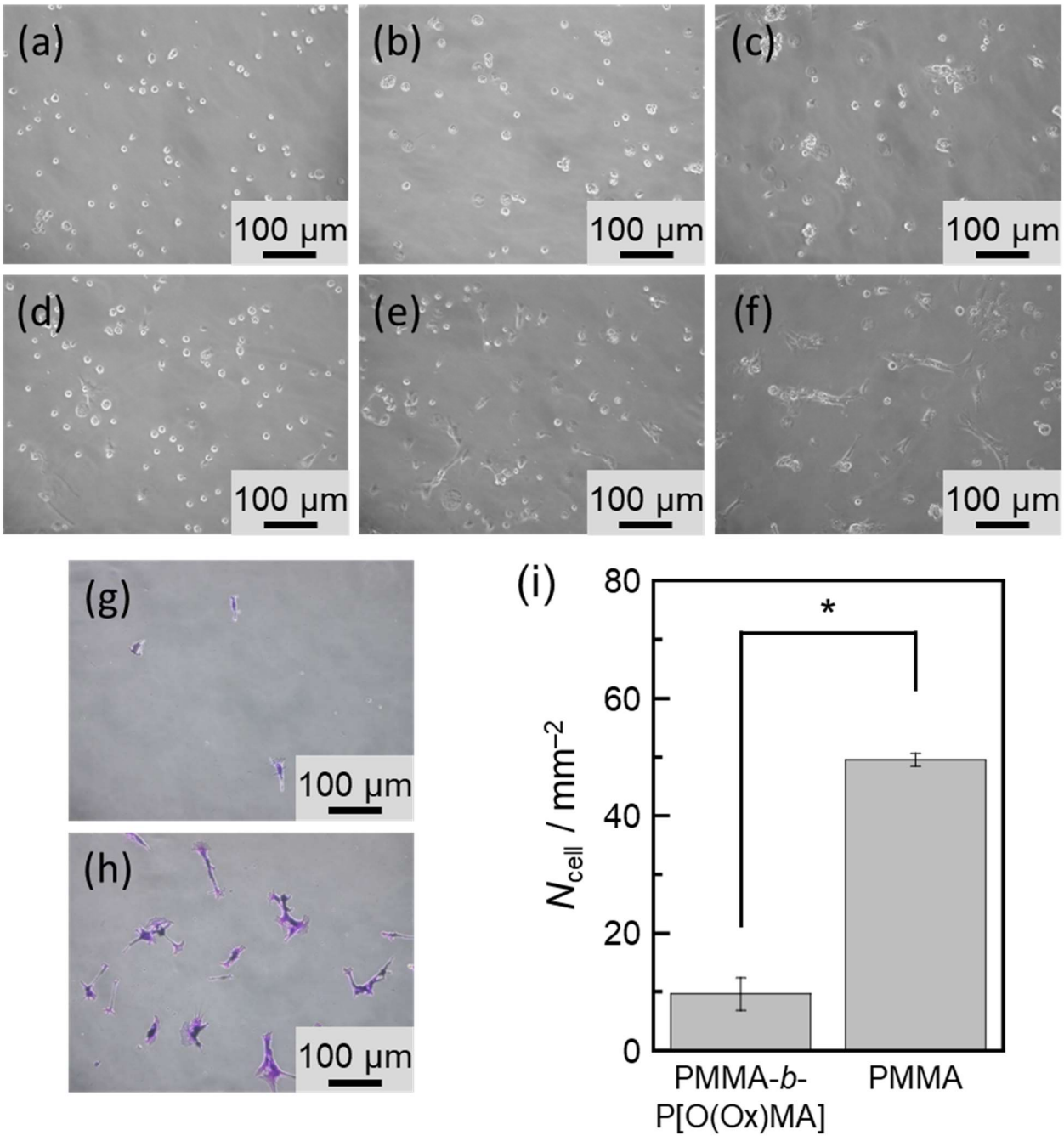

Fig. 3-8. (a–f) Phase-contrast microscopic images of NIH3T3 fibroblasts cultured on (a–c) PMMA-*b*-P[O(Ox)MA] and (d–f) PMMA films with culturing time; (a, d) 3 h, (b, e) 6 h and (c, f) 12 h. Cell culturing was pursued at 310 K in DMEM containing 10% FBS. (g, h) Phase-contrast microscopic images for adherent NIH3T3 cells on (g) PMMA-*b*-P[O(Ox)MA] and (h) PMMA films, respectively, after fixation/staining. (i) The N_{cell} value on each films. ANOVA: *$p < 0.01$.

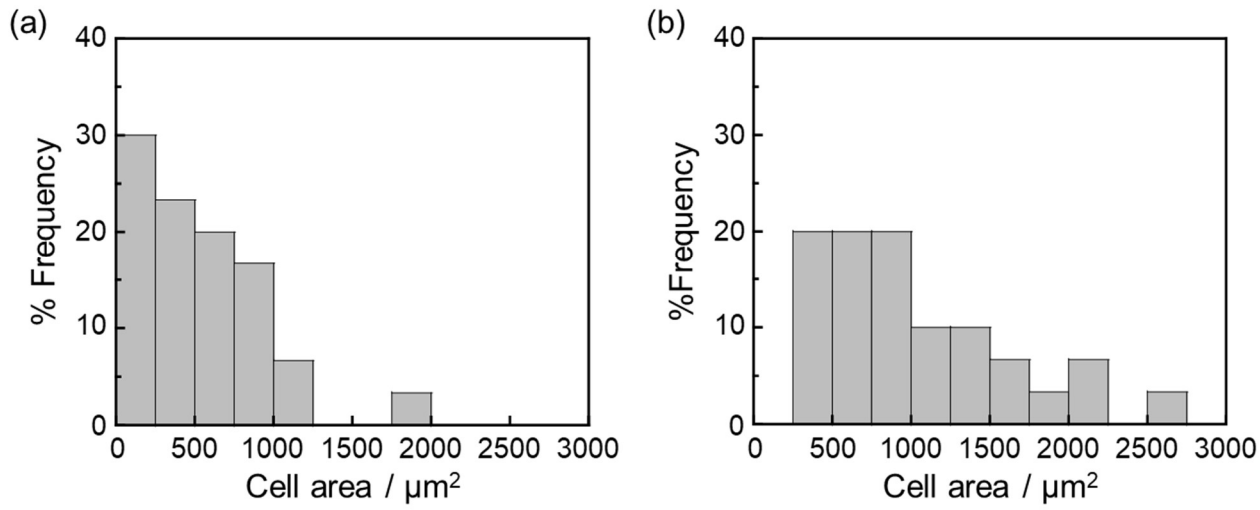

Fig. 3-9. The %frequency of projected area of adherent NIH3T3 fibroblasts on (a) PMMA-*b*-P[O(Ox)MA] and (b) PMMA films.

3.3.5. Protein adsorption test

The cell adhesion behavior was strongly influenced by FBS protein adsorption at the film surface. So, it was also examined a model protein of FBS adsorption test. Fig. 3-10 shows relative absorbance of the adsorption FBS. Like cell adhesion behavior, adsorption of FBS protein was strongly restricted on the block copolymer films comparing with the PMMA films and the reference PET sheets.

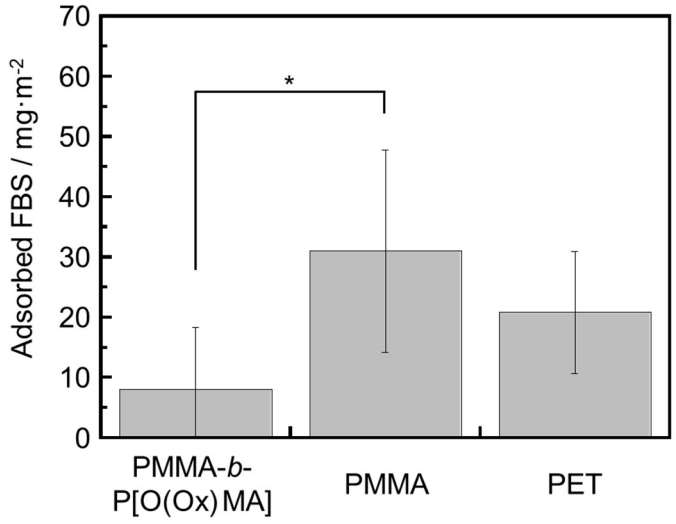

Fig. 3-10. Total amounts of adsorbed serum proteins on PMMA-*b*-P[O(Ox)MA], PMMA film, and PET sheet surfaces assessed by micro-BCA assay. The values are expressed as mean ± standard deviation; ANOVA: * $p < 0.01$.

3.4. Summary

As a first step to establish reasons why PEtOx shows excellent bio-inert properties, in this chapter, well-defined PEtOx/water interface was targeted to be construct by preparing the thin film of PMMA-*b*-P[O(Ox)MA]. Surface aggregation states of the thin film of PMMA-*b*-P[O(Ox)MA] under air and in water environment were estimated using AFM, AD-XPS, and NR measurement. Under air condition, just after thermal annealing, PMMA wetting layer, which thickness was approximately 5 nm, was formed on the block copolymer film. However, once the film contacted with water, the P[O(Ox)MA] block was segregated toward the water interface, forming diffused interfacial layer after contacting with water. Subsequently, it is confirmed that the interfacial layer composed of the segregated P[O(Ox)MA] block at the film surface strongly restrict the fibroblast cell and FBS protein adhesion behavior.

3.5. References

3-1) Maechling-Strasser, C.; Dejardin, P.; Galin, J. C.; Schmitt, A.; House-Ferrari, V.; Sebille, B.; Mulvihill, J. N.; Cazenave, J. P. Synthesis and Adsorption of a Poly(n-acetylethyleneimine)-Polyethyleneoxide-Poly (n-acetylethyleneimine) Triblock-Copolymer at a Silica/Solution Interface. *J. Biomed. Mater. Res.*, **1989**, 23, 1395.

3-2) Svoboda, J.; Sedlacek, O.; Riedel, T.; Hurby, M.; Pop-Georgievski, O; Poly(2-oxazoline)s One-Pot Polymerization and Surface Coating: From Synthesis to Antifouling Properties Out-Performing Poly(ethylene oxide). *J. Mater. Chem. B*, **2019**, 20, 3453.

3-3) Morgese, G.; Gombert, Y.; Ramakrishna, S. N.; Benetti, E. M. Mixing Poly(ethylene glycol) and Poly(2-alkyl-2-oxazoline)s Enhances Hydration and Viscoelasticity of Polymer Brushes and Determines Their Nanotribological and Antifouling Properties. *ACS Appl. Mater. Interfaces*, **2018**, *10*, 41839.

3-4) Konradi, R.; Pidhatika, B.; Muhlebach, A.; Textor, M. Poly-2-methyl-2-oxazoline: A Peptide-like Polymer for Protein-Repellent Surfaces. *Langmuir*, **2008**, *24*, 613.

3-5) Lorson, T.; Jaksch, S.; Lubtow, M. M.; Jungst, T.; Groll. J.; Luhmann, T.; Luxenhofer. A Thermogelling Supramolecular Hydrogel with Sponge-Like Morphology as a Cytocompatible. *Biomacromolecules*, **2017**, *18*, 2161.

3-6) Bai, L.; Tan, L.; Chen, L.; Liu, S.; Wang, Y. Preparation and Characterizations of Poly(2-methyl-2-oxazoline) Based Antifouling Coating by Thermally Induced Immobilization. *J. Mater. Chem. B*, **2015**, 3, 1921.

3-7) Wang, H.; Li, L.; Tong, Q.; Yan, M. Evaluation of Photochemically Immobilized Poly(2-ethyl-2-oxazoline) Thin Films as Protein-Resistant Surfaces. *ACS Appl. Mater. Interfaces*, **2011**, *3*, 3463.

3-8) Hea, T.; Janczewski, D.; Guo, S.; Man, S. M.; Jiang, S.; Tan, W. S. Stable pH Responsive Layer-

by-Layer Assemblies of Partially Hydrolysed Poly(2-ethyl-2-oxazoline) and Poly(acrylic acid) for Effective Prevention of Protein, Cell and Bacteria Surface Attachment. *Colloids Surf. B Biointerfaces*, **2018**, *161*, 269.

3-9) Tauhardt, L.; Frant, M.; Pretzel, D.; Hartlieb, M.; Bucher, C.; Hildebrand, G.; Schroter, B.; Weber, C; Cempe, K.; Gottschaldt, M.; Liefeith, K.; Schubert, U. S. Amine end-functionalized poly(2-ethyl-2-oxazoline) as promising coating material for antifouling applications. *J. Mater. Chem. B*, **2014**, *2*, 4883.

3-10) Zheng, X.; Zhang, C.; Bai, L.; Liu, S.; Tan. L.; Wang, Y. Antifouling Properties of Monothiol-terminated Bottle-brush Poly(methylacrylic acid)-graft-poly(2-methyl-2-oxazoline) copolymer on gold surfaces. *J. Mater. Chem. B*, **2015**, *3*, 1921.

3-11) Weber, C.; Becer, C. R.; Guenther, W.; Hoogenboom, R.; Schubert, U. S. Dual Responsive Methacrylic Acid and Oligo(2-ethyl-2-oxazoline) Containing Graft Copolymers. *Macromolecules*, **2010**, *43*, 160.

3-12) Morgese, G.; Verbraeken, B.; Ramakrishna, S. N.; Gombert, Y.; Cavalli, E.; Rosenboom, J. G.; Zenobi-Wong, M.; Spencer, N. D.; Hoogenboom, R.; Benetti, E. M. Chemical Design of Non-Ionic Polymer Brushes as Biointerfaces: Poly(2-oxazoline)s-Outperform Both Poly(2-oxazoline)s and PEG. *Angew. Chem. Int. Ed.*, **2018**, *57*, 11667.

3-13) Zhao, B.; Brittain, W. J. Polymer Brushes: Surface-Immobilized Macromolecules. *Prog. Polym. Sci.*, **2000**, *25*, 677.

3-14) Zdyrko, B.; Luzinov, I. Polymer Brushes by the "Grafting to" Method. *Macromol. Rapid Commun.*, **2011**, *32*, 859.

3-15) Li, Q.; Imbrogno, J.; Belfort, G.; Wang, X. L. Making Polymeric Membranes Antifouling via "Grafting from" Polymerization of Zwitterions. *J. Appl. Polym. Sci.*, **2015**, *132*, 41781.

3-16) Zhang, N.; Pompe, T.; Amin, I.; Luxenhofer, R.; Werner, C.; Jordan, R. Tailored Poly(2-oxazoline) Polymer Brushes to Control Protein Adsorption and Cell Adhesion. *Macromol. Biosci.*,

2012, *12*, 926.

3-17) Andrade, J. D. Surface and Interfacial Aspects of Biomedical Polymers. Volume 1. Surface Chemistry and Physics. *Ed., Plenum, New York*, **1985**, 197.

Chapter 4. Water-induced surface segregation of bottlebrush poly(2-ethyl-2-oxazoline) derivatives in the mixture films with poly(methyl methacrylate)

4.1. Background

To accomplish surface specified properties such as wettability adhesiveness and bio-inertness, it is necessary to approach to focus on surface with minimizing the affect for their bulk properties.[4-1~4] One of effective surface modification methods is through spontaneous segregation behavior of a component to the surface in multicomponent blend systems. The surface segregation of the one component in the blend system is natural phenomenon. Through the segregation behavior, thermodynamically stable surface can be formed. And also, it can achieve great surface modification effect even with small amount of addition is mixed, that is, it become a promising method in industry fields.[4-5,6]

As described in introduction section, there are several strategies for enhancing the surface segregation in terms of polymer structure. (1) Structure having lower surface free energy preferentially segregated toward surface.[4-5~8] (2) Polymer chains are arranged in a direction to minimize the conformational entropic loss.[4-9~12] This can explain that the higher the ratio of chain ends group, such as small molecular weight, tend to aggregate at the surface. In addition, the unique polymer architecture, such as branch and cyclic polymers, is considered as a tunable factor for the entropic-driven surface segregation.[4-13~15]

In addition to the structure effect, boundary environment, such as contacting liquid, solid and temperature is one of the key factor to the surface segregation behavior in the blend systems.[4-16~18] When the polymers contact at the boundary with different medium such as water, the local conformation and the segregation behavior was influenced by interfacial interaction between the polymer and the

contacting medium, subsequently, the polymer chains rearrange to minimize interfacial free energy. [4-19~21)]

In this chapter, I especially focus on the bottlebrush polymer architecture. Bottlebrush polymers, which is a class of a branch polymer, and have densely attached polymeric side chains to linear backbone. Whereas the linear backbone was strongly restricted, the polymeric side chain exhibit significant flexibility comparing with its linear structure.[4-15,22)] Therefore, thermodynamic properties of the structure are greatly influenced by the chemical composition of the side chain or its length.[4-23)] Base on the background, I prepared the bottlebrush P[O(Ox)$_n$MA]s with different degree of oligomerization of oxazoline side chain. Segregation behaviors of P[O(Ox)$_n$MA]s in mixtures with PMMA were planned to demonstrate controlled by entropic effects based on oxazoline side chain length. Then, the surface functionality of bioinertness were planned to be evaluated on the modified film surfaces.

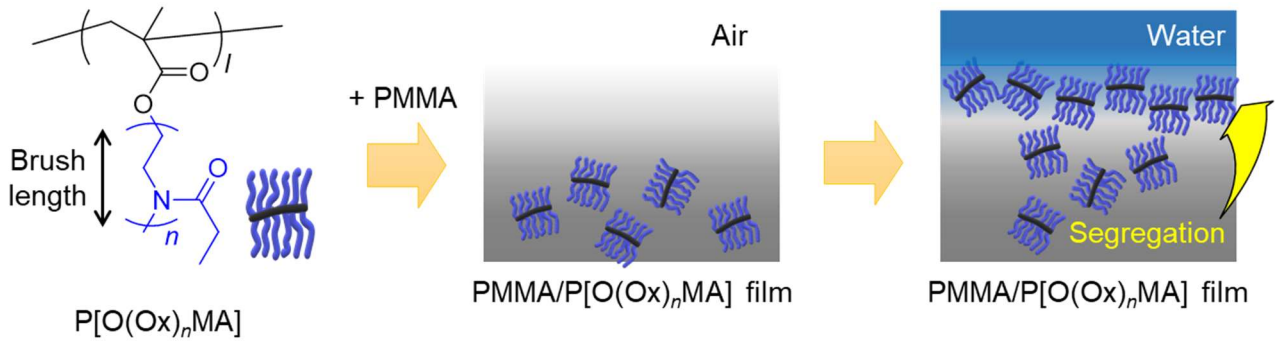

Fig. 4-1. A schematic illustration of formation of the water-induced P[O(Ox)$_n$MA] segregation layer in a mixture with PMMA film at the water interface.

4.2. Experimental

4.2.1. Materials

Bottlebrush P[O(Ox)$_n$MA]s were synthesized by combination of LCROP and ATRP as described in chapter 2. Also, commercially available PMMA and dPMMA (Polymer Source, Inc., Quebec, Canada) were prepared as matrix polymers. Table 4-1 summarizes the structure characteristics of the synthetic polymers used in this study. The M_n, M_w/M_n, and the degree of polymerization of main chain (l) and oxazoline side chain (n) of the P[O(Ox)$_n$MA]s were determined by SEC and ^{1}H NMR. For convenience, two types of bottlebrush P[O(Ox)$_n$MA]s, which have almost the same main chain lengths (l = 12 or 13) and different side chain lengths (n = 7 or 19), were going to called P[O(Ox)$_7$MA] and P[O(Ox)$_{19}$MA] in the following section. The glass transition temperatures of polymer in the dried state ($T_{g,dry}$) and in the wet state ($T_{g,wet}$) were examined by DSC. The wet samples were prepared by immersing the dried samples in water at RT for 24 h. The DSC measurements were conducted in a temperature range of 173 to 353 K with a heating rate of 10 K·min^{-1}. Surface free energies (γ) of the polymers were evaluated by static contact angle measurements according to Owens' procedure[4-24,25] using droplets of ethylene glycol (γ_{LV}^d= 29.0 mN·m^{-1}, γ_{LV}^p= 19.0 mN·m^{-1}) and diiodomethane (γ_{LV}^d= 50.8 mN·m^{-1}, γ_{LV}^p= 0.00 mN·m^{-1}) as a polar and a nonpolar probe, respectively.[4-26,27] γ_{LV}^d is the dispersion factor of liquid-vapor surface free energy, and the γ_{LV}^p is the polarity factor of the surface free energy.[4-27]

Table 4-1. Characteristics of the synthetic polymer used in this study.

Polymer	M_n[a]	M_w/M_n[a]	l[a]	n[b]	$T_{g,dry}$[c]/ K	$T_{g,wet}$[c]/ K	γ[d]/ mJ·m^{-2}
P[O(Ox)$_7$MA]	7.4k	1.40	12	7	300	255	44.8
P[O(Ox)$_{19}$MA]	22.3k	1.24	13	19	312	254	45.1
PMMA	171k	1.09	1708	–	405	–	42.1
dPMMA	174k	1.09	1609	–	–	–	–

[a] Determined by SEC calibrated with five PMMA standards. [b] Determined by end group analysis by using ^{1}H NMR spectroscopy. [c] Evaluated by DSC. [c]Estimated by static contact angle measurement. Ethylene glycol and diiodomethane were used as polar, and nonpolar probes, respectively.

4.2.2. Film preparation

The miscibility between the PMMA and P[O(Ox)$_n$MA]s with various weight ratio was examined by DSC. For the measurement, PMMA films containing different amounts of P[O(Ox)$_n$MA]s were prepared by solvent casting methods from their chloroform solutions on poly(tetrafluoroethylene (PTFE) substrates (NICHIAS Corp, Tokyo, Japan). The weight ratio between the PMMA and P[O(Ox)$_n$MA]s were 85/15, 70/30, 60/40, 50/50, 40/60 (wt/wt %). After the solvent casting, the films were dried at RT under room pressure for 24 h, following vacuum dried at 333 K for overnight. The dried films peeled out of the PTFE plates, and then, each film were placed on the aluminum pans. As a reference, an empty aluminum pan was used. Temperature range for the measurement was 243-453 K, with the heating rate of 10 K·min^{-1} under nitrogen flow.

To prepare PMMA thin films containing P[O(Ox)$_n$MA], solid substrates such as Si wafer and borosilicate glass, and quartz substrates were hydrophobized with chloro(decyl)dimethylsilane following the same procedure described in chapter 3. Then, the thin film was prepared by spin coating methods on the solid substrates from their mixed solution in chloroform. The weight ratio of the PMMA and P[O(Ox)$_n$MA] was fixed at 85/15 wt/wt%. For the other mixing ratio, such as 70/30 and 50/50, the stability of the thin films in aqueous environment was insufficient to do further characterization. The detail results were going to described following section. As a reference, PMMA homo film was spin-coated on the solid substrates without hydrophobization. The prepared thin films were annealed at 423 K for 12 h.

4.2.3. Surface aggregation states of the thin films

The surface morphologies of PMMA containing P[O(Ox)$_n$MA] additives and reference PMMA films were observed by AFM (Cypher ES) using AC mode under air at 298 K. A silicone cantilever coated its tip with Al was used. A spring constant and a resonance frequency of the cantilever were 12 N·m^{-1} and

116 kHz. Surface wettability of the blend film were evaluated by static contact angle measurement using water droplet as a probe.

The chemical composition on the films was examined by AD-XPS with Al-Kα anode source. The X-ray irradiation was operated at 15 kV and 25 W. The emission angle (φ_e) was set in a range of 15 to 90°. The XPS peaks were calibrated to a binding energy of 285.0 eV for neutral carbons.

4.2.4. Water-induced surface rearrangement

Film stability and the surface hydrophilicity of the thin films in aqueous environment was examined by the static contact angle measurement using 2 μL of air bubble as a probe. The static contact angle values were recorded as a function of immersion time in water. The initial contact angle was obtained in 2 min after immersing film in water, and air bubble contact angles were recorded in every 1 h until 24 h.

The morphology of the outermost region of the films in aqueous environment was observed by AFM using AC mode at 298 K. A spring constant and a resonance frequency of the Si microfabricated cantilever, which tip was coated with Al, were 1.2 $N \cdot m^{-1}$ and 34 kHz.

The chemical composition of the freeze-dried film surfaces was evaluated by AD-XPS in a same manner. To prepare the freeze-dried films, thermal annealed film was first immersed in water for 12 h, following the surfaces were iced by liquid nitrogen and lyophilized for 2 h. The obtained sample were also examined by AD-XPS in a same manner.

In order to evaluate the surface chemical composition in the environment close to real aqueous phase, near ambient pressure X-ray photoelectron spectroscopy (NAP-XPS) were conducted under Ar gas and water vaporized conditions using an EnviroESCA (SPECS Surface Nano Analysis GmbH, Berlin, Germany) with Al-K_α source at room temperature. The pressure of the Ar gas or water vapor in the analysis chamber was set to automated control. Also, several differential stages of pump system were

applied to compensate the difference between pressure in the analysis chamber and that in electron detector which was kept under high vacuum.[4-28,29)] The emission angle from sample to the electron detector was fixed at 90°. The obtained XPS signals were calibrated to a binding energy of 285.0 eV corresponding with the neutral carbon. The detail procedures for the measurement were as follows. First, thermal annealed films were set on a sample stage, and then, the stages were introduced into the main chamber. Thereafter, the chamber was filled with Ar gas. After reducing the pressure to 1.3 kPa, NAP-XPS measurement was conducted. Figure 4-2 shows a schematic illustration for NAP-XPS measurement carried out in water vapor environment. Before the measurements, the thermal annealed films were immersed in ultrapure water at RT for 24 h. The hydrated films were placed on a sample stage with a petri dish. The petri dish was filled with enough water to fully cover the film surfaces. Subsequently, the sample stage was introduced into the analysis chamber. The pressure in the analysis chamber gradually decreased to evaporate water on the sample surfaces and to reach to 1.3 kPa. The measurement was conducted in a same manner in the water vapor environment.

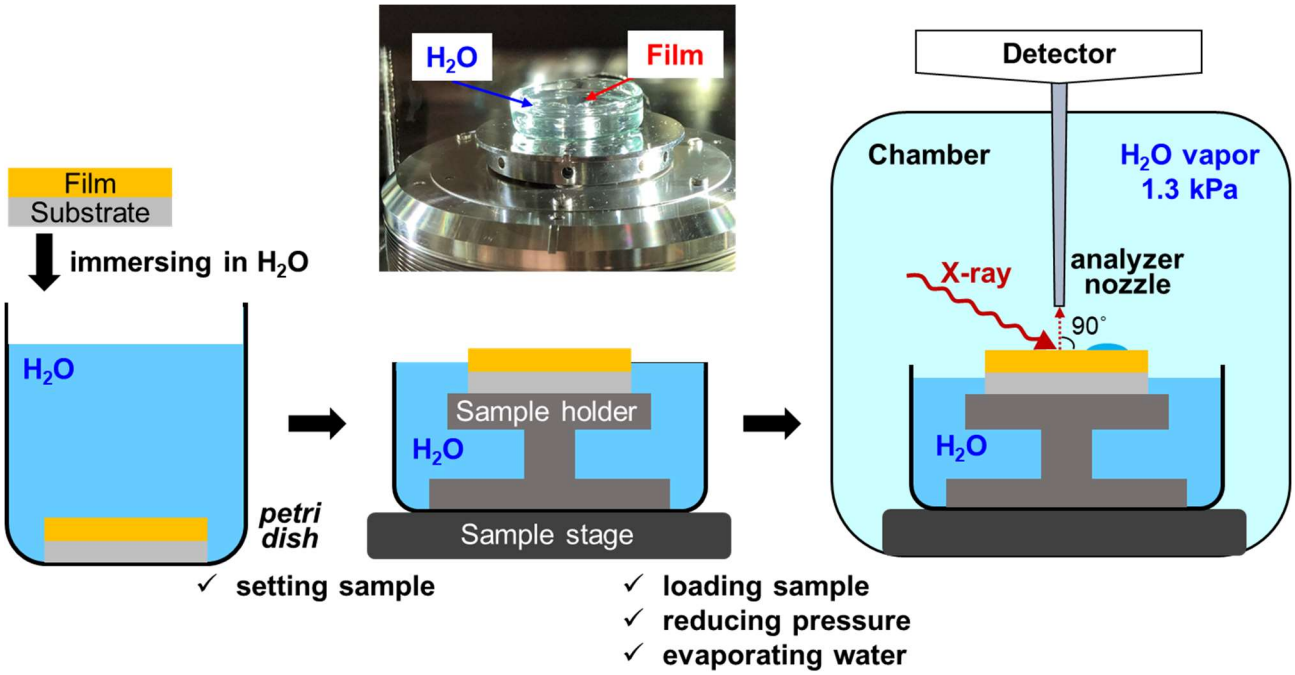

Fig. 4-2. A schematic illustration of NAP-XPS measurement in water vapor environment after hydrating films.

4.2.5. Density profiles of the mixture films

The density profile of the mixture films along the normal direction from the film surface was examined by SOFIA at the MLF in J-PARC. For the NR measurement, similar length of dPMMA was used instead of PMMA to increase contrast between (b/V) values for the dPMMA and P[O(Ox)$_n$MA]. The dPMMA/ P[O(Ox)$_n$MA] films were spin-coated on 60 × 60 × 8 mm size of the hydrophobized quartz substrate. The procedures for the measurement conducted in air and D_2O conditions were as follows. First, the measurement was carried out under air. Then, the films were immersed in D_2O contained in a Teflon-made reservoir at RT for 4 h, which was enough to reach quasi-equilibrium states. The measurement was conducted in D_2O in a same manner. The neutron beams were irradiated on the film surface side in air and on the quartz side in D_2O. The incident angles were set as 0.3, 0.75, and 1.8°. The neutron reflectivity was calculated using the Motofit programs based on a model scattering length density (b/V) profile along the depth direction using the error function. The (b/V) values of dPMMA, P[O(Ox)$_n$MA], SiO_2, and D_2O used for the calculations were 7.02×10^{-4}, 0.88×10^{-4}, 3.48×10^{-4}, and 6.36×10^{-4} nm^{-2}, respectively.

4.2.6. Mechanical properties of the thin films at water interface

Mechanical properties of the thin films at water interface were estimated on a basis of force- distance (F-d) curve measurement by AFM (E-sweep with a SPI3800 controller, Hitachi High-Tech Science) using contact mode at RT in water. Spring constant and tip radius of the silicone cantilevers coated with Au were 1.3 N·m^{-1} and 40 nm. Force curves were obtained with an approach speed of 50 nm·s^{-1} at randomly selected 5 positions.

4.2.7. Bioassay

NIH3T3 fibroblast cell adhesion behaviors on the thin film were estimated. The detail procedures were as follows. First, the thin films, which were coated on borosilicate glass, were placed in 24-well plates composed of the tissue cultured poly(styrene) (TCPS) (Corning Incorporated) and were immersed in water at RT for 24 h. After removing water, the 4×10^4 cells·cm^{-2} of cell suspension in DMEM with 10% FBS were added in each plate. Subsequently, the cells were cultured at 310 K for 12 h. After 12 h of the cell culturing, the weakly adherent or suspended cells were washed by PBS several times. The strongly adherent cells on the films were fixed by adding 2 % (vol./vol.) of glutaraldehyde/PBS, keeping at 277 K for 20 min. Then, the fixed cells were stained by immersing the films in 0.01 wt% crystal violet/mixed solvent of methanol/water (1/200 (vol./vol.)). The number and morphology of the adherent cells were evaluated by using phase-contrast microscopy.

For a protein adsorption test, 10 % FBS in DMEM was used as a protein sample solution. Before the test, the thin films coated on Si-wafer were immersed in water at RT for 24 h. After removing the water, 10 % FBS in DMEM was charged on the films. Subsequently, the films were incubated at 310 K for 1 h. After washing the film surface gently by PBS, the adsorbed proteins were detached by 1wt% of aqueous SDS solution and the sample solutions were sonicated at 313 K for 20 min. The concentration of the detached protein was examined by the microplate procedure of a micro-BCA protein assay kit with calibrating with 9 different concentration of bovine serum albumin standards. The absorbance of the light at the wavelength of 560 nm was recorded by using a plate reader (INFINITE 200). As references, PMMA films and polyethylene terephthalate (PET) sheets were used.

The platelet adhesion test was conducted on the thin films. For the test, platelet-rich plasma was separated from human blood by centrifugation. Before test, the films and reference poly(ethylene terephthalate) (PET) sheets were hydrated in water at RT for 12 h. After removing the water, 0.2 mL of platelet suspension solution was added on each sample and incubated at 310 K for 1 h. After washing

the surfaces by PBS 3 times, the adhered platelets were fixed by immersing the samples in 2 % (v/v) of glutaraldehyde/PBS solution. Then, samples were dried under air at RT. The number and morphology of the adhered platelet was observed by using an SU3800 scanning electron microscope (SEM, Hitachi High-Tech Corp., Tokyo, Japan) at acceleration voltage of 15 kV with samples which were sputter-coated by using Pt target before the observation.

4.3. Results and discussion

4.3.1. Miscibility between PMMA and P[O(Ox)$_n$MA]

Panel (a) of Fig. 4-3 shows DSC curves for PMMA containing different weight ratio of P[O(Ox)$_7$MA] and each of the homopolymers. The DSC curves corresponding with homo P[O(Ox)$_7$MA] and PMMA, represent a single baseline shift and the defined T_gs were 300 K and 405 K, respectively. On the other hand, two baseline shifts were detected in the DSC curves for the mixture regardless of mixing ratio, meaning that, phase-separation was occurred in the mixture with all the mixing ratios. However, unlike the general phase separation behavior in which the glass transition temperature of each component is maintained, the two baseline shifted were detected between the positions of baseline shift for each homopolymers; the $T_{g,l}$ of the PMMA/P[O(Ox)$_7$MA] mixtures were 320 K and $T_{g,u}$ were 400 K for all weight ratios. These results suggested that states of the phase separation were not strong, in other word, the PMMA and P[O(Ox)$_7$MA] were in partial miscible states. In the case of PMMA/P[O(Ox)$_{19}$MA] mixtures, similar tendency was observed in the DSC curves. Panel (b) of Fig. 4-3 is the DSC curves for PMMA/P[O(Ox)$_{19}$MA] mixtures. $T_{g,l}$ of the PMMA/P[O(Ox)$_{19}$MA] mixtures were 325 K and $T_{g,u}$ were 400 K for all weight ratios.

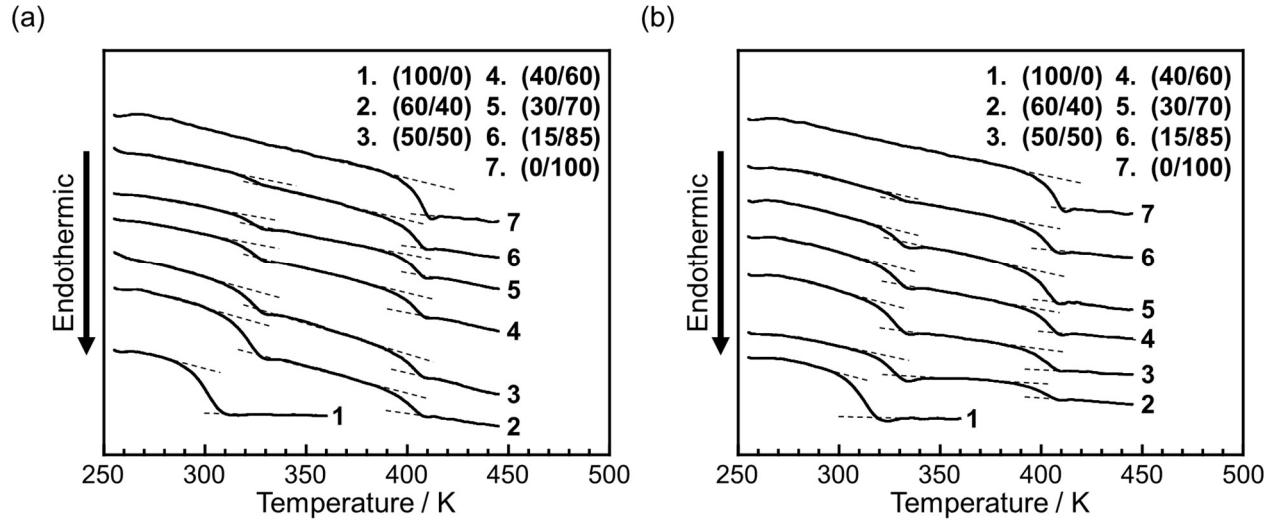

Fig. 4-3. DSC curves for (a) PMMA/P[O(Ox)$_7$MA] and (b) PMMA/P[O(Ox)$_{19}$MA] mixtures with various weight ratios and that for P[O(Ox)$_n$MA] and PMMA homopolymers. The ratios of PMMA/P[O(Ox)$_n$MA] (wt/wt %) are shown in brackets. The DSC curves were obtained at the third heating cycles. The T_gs were determined as mid-points of the baseline shifts.

4.3.2. Film stability in water

Because P[O(Ox)$_n$MA]s are highly water soluble, the stability of the thin PMMA films containing P[O(Ox)$_n$MA]s was an important factor to construct stable bio-inert surfaces. Therefore, the stability of the PMMA/P[O(Ox)$_{18}$MA] films with weight ratio of (50/50), (70/30), (85/15), was estimated by static contact angle measurement in water. In a case of (50/50) mixture film, the film was peeled off from the substrate in aqueous environments. This is probably because the film contained the large amount of water-soluble P[O(Ox)$_{19}$MA] and the oxazoline segments easily dissolved in water. On the other hand, the mixture films with the weight ratios of (70/30), (85/15) were kept maintaining their film states on the substrate without peeling off. So, the measurement was conducted on the two films.

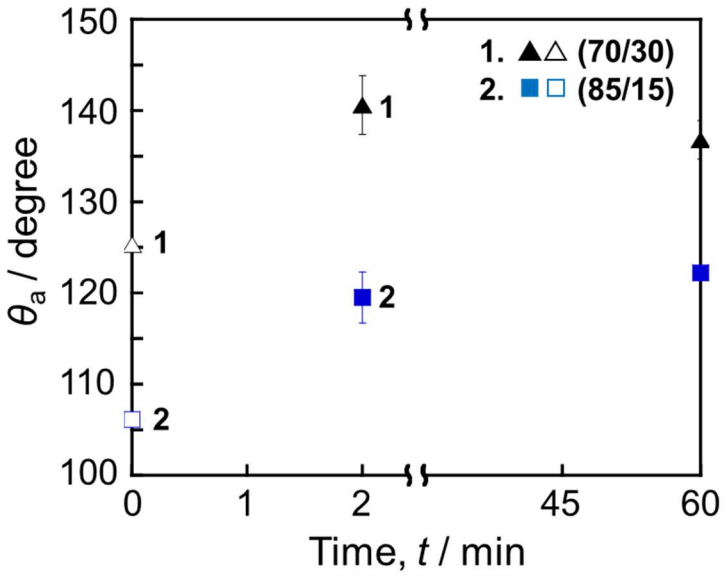

Fig. 4-4. Immersion time (t) dependence of θ_a on PMMA/P[O(Ox)$_{19}$MA] films with weight ratios of (70/30) and (85/15). Open symbols indicate theoretical values at $t = 0$, calculated by $180 - \theta_w$ which θ_w is water droplet contact angles in air.

Fig. 4-4 shows immersion time dependence of the air bubble contact angle against PMMA/ P[O(Ox)$_{19}$MA] with the mixture ratios of (70/30) and (85/15). In the case of (70/30) mixture film, the value of air bubble contact angle was 140.6 ± 3.2° at 2 min of immersion time. However, the value was decreased to 136.8 ± 2.1° after 1 h, meaning that, some amounts of P[O(Ox)$_{19}$MA] in the mixture films leaked to the aqueous phase. The mixture film of (85/15), on the other hand, the value of the air bubble contact angles was changed from 119.5 ± 2.8 to 122.2 ± 0.1° in the same periods. As showing following figures, the air bubble contact angle was evaluated to be maintained until 24 h. Therefore, it was considered that mixture films with the mixing ratio of (85/15) were suitable for the further surface characterization. For convenience, the PMMA films containing 15% of P[O(Ox)$_7$MA] or P[O(Ox)$_{19}$MA] are going to referred as 7Ox and 19Ox, respectively.

4.3.3. Surface aggregation states of the thin films

The surface aggregation states of the films, which acquired in air, were examined by AFM in conjunction with static contact angle measurement using water droplet and diiodomethane as a probe. Panel (a-c) of Fig. 4-5 show height images for (a) 7Ox, (b) 19Ox, and (c) PMMA film surfaces under air. The R_{RMS} values for the films were 0.42, 0.30, and 0.22 nm, separately. The mixture film surfaces were relatively rough than PMMA film, however, the roughness for the mixture films was sufficiently small for further surface characterization. Also, all of the film surfaces were featherless in their phase image as shown in panel (d-f) of Fig. 4-5. Surface wettability on the films was estimated by static contact angle measurement. The water droplet contact angles for 7Ox and 19Ox were 72.6 ± 1.9 and 72.9 ± 1.6°, respectively, which were slightly lower than that on the PMMA film (75.1 ± 0.4°). Also, calculated surface free energy values against the 7Ox and 19Ox films were determined as 44.3 and 43.9 $mJ \cdot m^{-2}$.[4-24] Taking into account the values for the contact angles and the surface free energies, it is considered that the outermost regions of the mixture films were mainly covered by homogenous phase of PMMA-rich layers.

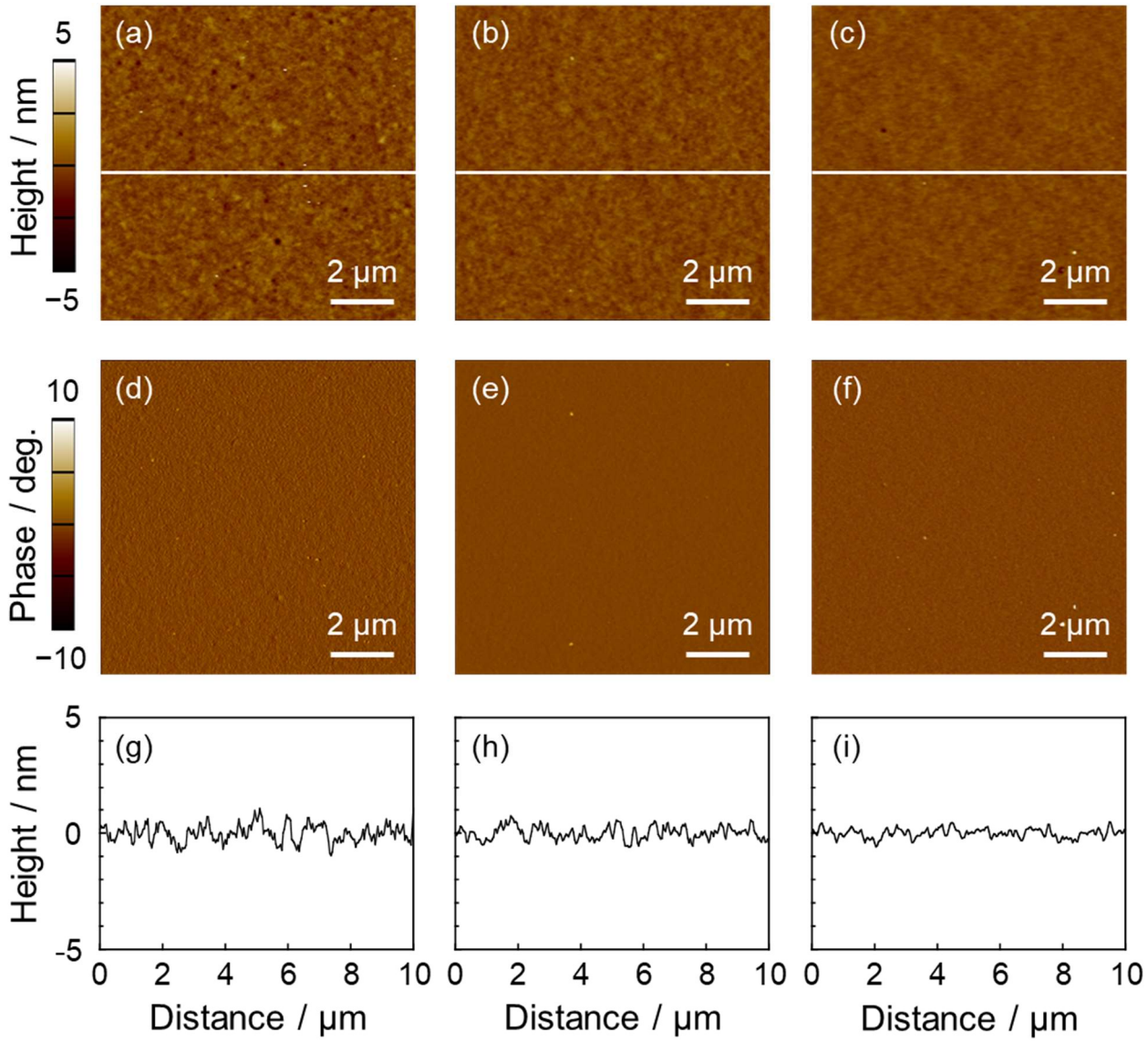

Fig. 4-5. AFM (a-c) height, (d-e) phase images, and (g-i) sectional views along lines in height images of (a-c); (a, d, g) 7Ox, (b, e, h) 19Ox, and (c, f, i) PMMA films acquired in air.

To prove the hypothesis, AD-XPS measurement was conducted on the mixture films. Panel (a, b) of Fig 4-6 shows XPS (a) N_{1s} and (b) C_{1s} spectra for the 7Ox, 19Ox, and PMMA films at the emission angle of 60°. Frist, in N_{1s} spectra, a signal corresponding with tertiary amine (N–C=O) was observed at 400 eV, whereas no signal was observed on the PMMA film. This imply that the P[O(Ox)$_n$MA] located close to the surface region. Also, the intensity of the nitrogen signals was much stronger for 7Ox than 19Ox, meaning that, large amounts of P[O(Ox)$_7$MA] having shorter side chain were aggregated at the surface

than P[O(Ox)$_{19}$MA] having longer side chain. The trend was also demonstrated by C_{1s} spectra shown in panel (b) of Fig. 4-6. Whereas the C_{1s} spectrum for the PMMA film was decomposed to three peaks corresponding with neutral (C–C/C–H), ether (C–O), and ester (O–(C=O)) carbon at binding energy of 285.0, 286.5, and 288.9 eV, the C1s spectra for the mixture films needed two more peaks attributed to amine (C–N), and amide(N–(C=O)) at the binding energy of 286.0, and 287.7 eV. And, the intensity for the two peaks were stronger for 7Ox than that for 19Ox. Panel (c) of Fig. 4-6 shows sin φ_e dependence of I_{N1s}/I_{C1s} for the mixture films. The important feature was that the I_{N1s}/I_{C1s} decreased with smaller φ_e. Also, the values for the I_{N1s}/I_{C1s} were much stronger for 7Ox than that for 19Ox in all range of φ_e. To discuss the trends quantitatively, the relationship between I_{N1s}/I_{C1s} and the real analytical depth was estimated with the following equation once described in chapter 3;

$$\frac{I_{N1s}}{I_{C1s}} = \frac{\int_0^\infty [n_N(z)\cdot\exp(-z/\lambda_N \sin\varphi_e)]dz}{\int_0^\infty [n_C(z)\cdot\exp(-z/\lambda_C \sin\varphi_e)]dz} \quad (4\text{-}1)$$

where z is the analytical depth, λ_i and $n_i(z)$ are the inelastic mean-free path of photoelectrons and the atomic fraction of i component. For a model profile, the following two uniform over-layer was used for the fitting;

$$n_N(z) = \begin{cases} n_{N,s} \ (z < z_i) \\ n_{N,\infty} \ (z > z_i) \end{cases} \quad (4\text{-}2)$$

where the $n_{N,s}$ and $n_{N,\infty}$ are the nitrogen atomic fraction at the top surface and in the bulk, respectively. Solid curves in panel (c) of Fig. 4-6 are the best-fit results based on the model composition profiles of nitrogen atomic fraction (n_N) shown as solid lines in panel (d) of Fig. 4-6. In the case of the 7Ox, the surface PMMA-rich layer was to be existed with a thickness of approximately 5 nm with n_N of 8×10^{-3} at the surface. In addition, 19Ox mainly covered surface PMMA-rich layer with a thickness of approximately 6 nm, the n_N value was 1×10^{-3} smaller than that of the 7Ox. Therefore, it can be supports the hypothesis that the mixture films were mainly covered with PMMA component and oxazoline units were existed just under the top PMMA-rich layer.

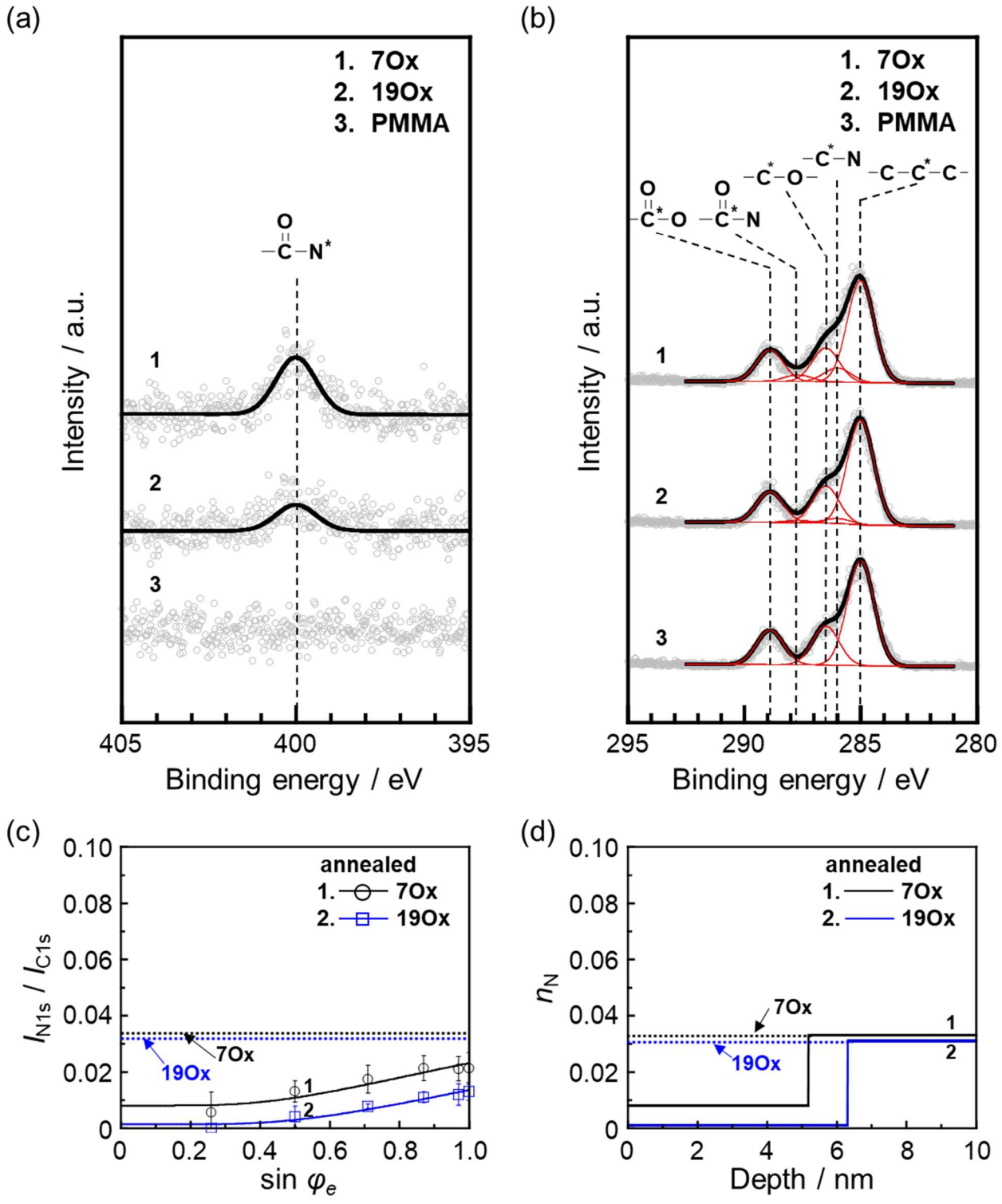

Fig. 4-6. XPS (a) N_{1s} and (b) C_{1s} core level spectra of 7Ox, 19Ox, and reference PMMA films acquired at φ_e=60°. The black solid line in panel (b) was composite of the red solid lines. (c) I_{N1s}/I_{C1s} as a function of sin φ_e. Open circle and open square are the experimental data and solid line denote fitting curves on the basis of model composition profiles of nitrogen atomic fraction shown in (d). Black solid line attributes to 7Ox and blue solid line is for 19Ox.

4.3.4. Water-induced surface rearrangement

In general, changing surrounding environment, surface polymer structure is rearranged to minimize interfacial free energy. Therefore, we subsequently estimated the surface aggregation states on the mixture films after contacting with water. Panels (a-c) of Fig. 4-7 shows AFM height images of (a) 7Ox, (b) 19Ox, and (c) PMMA films. For the observation, the films were immersed in water in advance for at least 4 h, which was to reach a *quasi*-equilibrium state. The R_{RMS} values of the films for the 7Ox, 19Ox, and PMMA were 1.22 nm, 0.61 nm, and 0.21 nm. Even though R_{RMS} of PMMA was almost unchanged comparing with the value obtained in air, that for the mixture films became bigger. This suggests that the structure rearrangement on the mixture films after contacting with water. However, only the small contrasts were observed in the phase images of the mixture films as shown in panels (d-f) of Fig. 4-7.

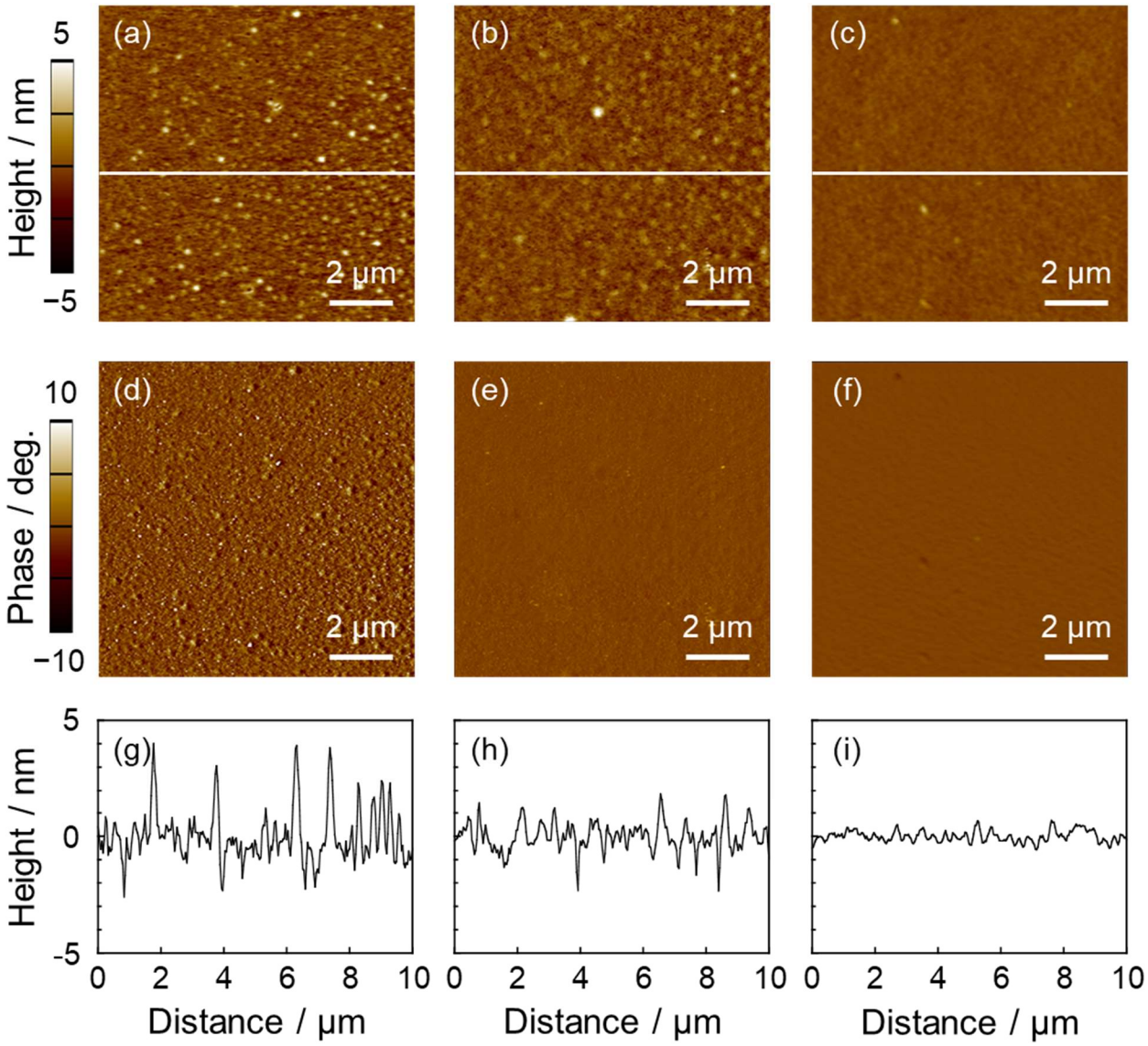

Fig. 4-7. AFM (a-c) height, (d-e) phase images, and (g-i) sectional views along lines in height images of (a-c); (a, d, g) 7Ox, (b, e, h) 19Ox, and (c, f, i) PMMA films acquired in water.

To trace the structure rearrangement on the films, the θ_a was recorded as a function of immersion time (t) in water. Panels (a, b) of Fig. 4-8 show the results and its enlarged figure at the first 1 h, respectively. The open symbols at t = 0 are the theoretical values ($\theta_{a(t=0\ h)}$), which were obtained by $180 - \theta_w$. If there was no structure rearrangement occurred on the films, the θ_a values keep constant at the $\theta_{a(t=0\ h)}$ of 107.4 for 7Ox, 107.1 for 19Ox, and 104.9° for PMMA films, respectively. However, the θ_a values for the films increased within 2 min and saturated to constant values within a few hours. The θ_a values at t = 24 h

($\theta_{a(t=24\ h)}$) for the 7Ox, 19Ox and PMMA films were 128.6 ± 1.6, 124.8 ± 1.5, and 113.9 ± 0.4°, respectively. In the case of PMMA film, the increase of θ_a could be explained by the change in the local conformation of the PMMA chains in water.[4-19] Whereas the change in θ_a ($\Delta\theta_a$), given by $\theta_{a(t=24\ h)} - \theta_{a(t=0\ h)}$, for the PMMA was around 9°, $\Delta\theta_a$ for the mixture films were approximately, 21 and 18° for 7Ox and 19Ox mixture films, respectively. The results also suggest that the structure rearrangement was occurred in a large spatial scale on the mixture films and the extent of the surface rearrangement was also influenced on the length of the oxazoline unit lengths. In addition, it also be confirmed that the mixture films were stable in aqueous environment for 24 h.

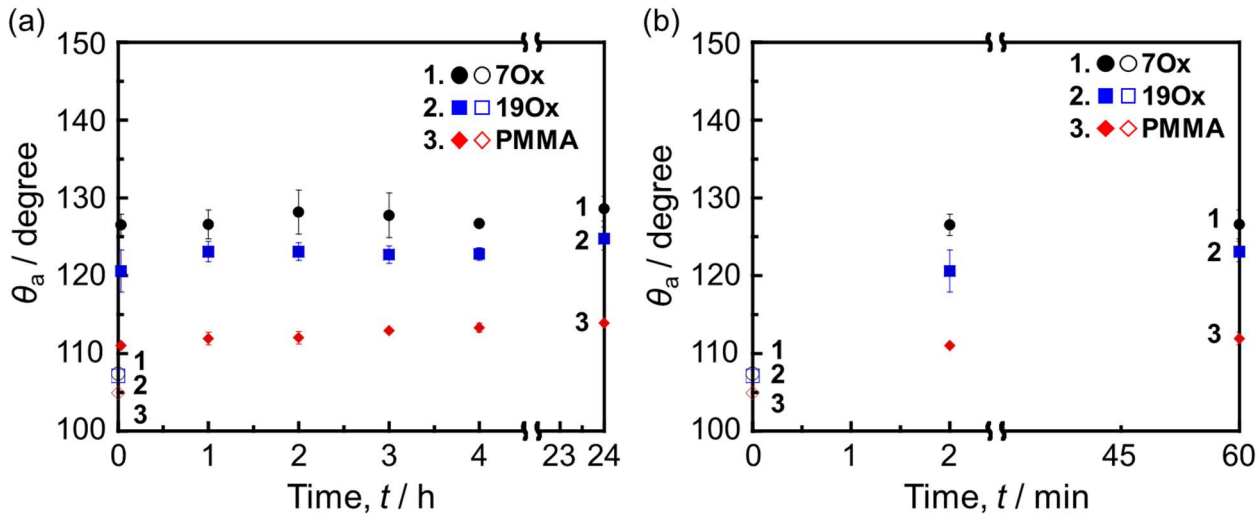

Fig. 4-8. (a) Immersion time (t) dependence of the θ_a values against 7Ox, 19Ox, and PMMA films at RT in water, and (b) enlarged figure of in a range of t = 0 h to 1 h. Open shapes at t = 0 ($\theta_{a(t=0\ h)}$) are theoretical value, calculate by 180 − θ_w.

Due to the structure rearrangement occurred in water, surface aggregation states of the polymer were also affected. In order to evaluate the aggregation states on the mixture films at water interface, surface chemical composition at the outermost region of the freeze-dried films was examined by AD-XPS. Panels (a, b) of Fig. 4-9 show the (a) N_{1s} and (b) C_{1s} spectra for the freeze-dried 7Ox at different φ_es of 15, 30, 90° and the representative spectrum for the freeze-dried PMMA at φ_e of 15°. In the case of N_{1s}

spectra for the 7Ox, a nitrogen signal at 400 eV corresponding with tertiary amine (N–C=O) peak was clearly observed. In addition, the relative integral intensity of the nitrogen signals increased with decreasing the φ_e. The similar trends also observed in C_{1s} spectra. The oxazoline related signals of amine carbon (C–N), and amide(N–(C=O)) at the binding energy of 286.0, and 287.7 eV increased with decreasing the φ_e. This tendency was opposite to that of formation of PMMA-rich surface layer under air. That is, the outermost region of the mixture films was converted from the PMMA-rich phase to the P[O(Ox)$_n$MA]-rich phase in aqueous environment.

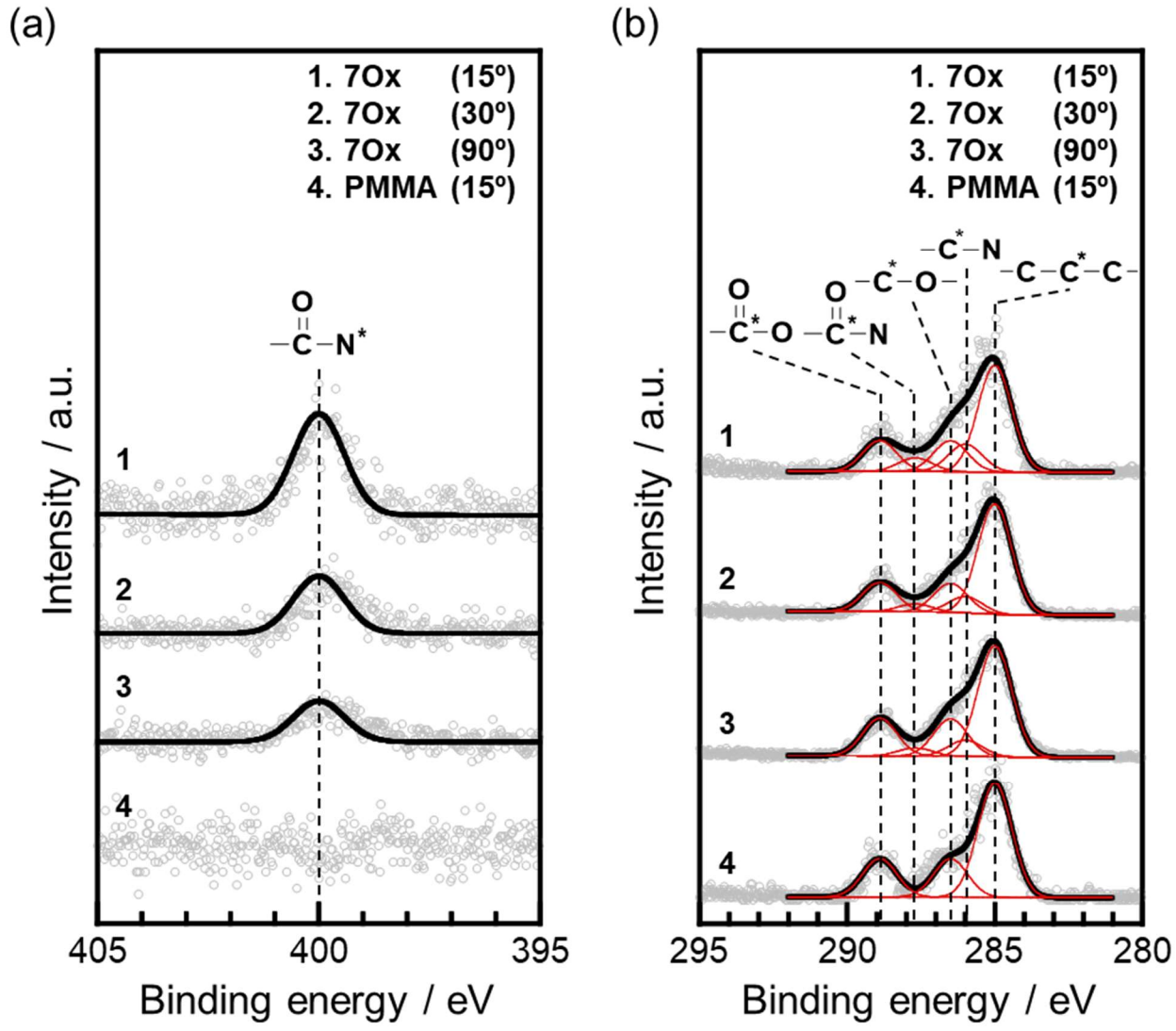

Fig. 4-9. XPS (a) N_{1s} and (b) C_{1s} core level spectra for 7Ox film at various φ_es of 15, 30, 90°, and the representative spectrum for PMMA film acquired at φ_e=15°. The black solid line in panel (b) was decomposed to the red solid lines.

For quantitative discussion, panel (a) of Fig. 4-10 summarize I_{N1s}/I_{C1s} as a function of sin φ_e. In addition, the following model composition profile was applied to the fitting equation of (4-1);

$$n_N(z) = n_{N,\infty} + \left(n_{N,s} - n_{N,\infty}\right) \cdot \exp(-z/\xi) \qquad (4\text{-}3)$$

where the $n_{N,s}$, $n_{N,\infty}$ are the nitrogen atomic fraction at the top surface and in the bulk, and ξ is the decay length. Dash lines in panel (a) of Fig. 4-10 are the best-fit results on the basis of the model profiles described as dashed line in panel (b) of Fig. 4-10. The obtained fitting parameter of $n_{N,s}$ values were 8.1×10^{-2} for the 7Ox and 8.9×10^{-2} for the 19Ox, which were greater than those for the calculated bulk values based on the chemical structure of each components and their mixing ratio. The most interesting feature for the fitting were the ξ parameter. While ξ value for the 19Ox was 0.78 nm, that for 7OxB was 1.8 nm. This means that the thicker P[O(Ox)$_7$MA] layer was formed on the 7Ox film than P[O(Ox)$_{19}$MA] layer on 19Ox film at water interface. This can be considered as molecular size effect of P[O(Ox)$_n$MA]. The small size of P[O(Ox)$_7$MA] is more easily segregated toward the water interface than P[O(Ox)$_{19}$MA] thanks to the entropic effects.

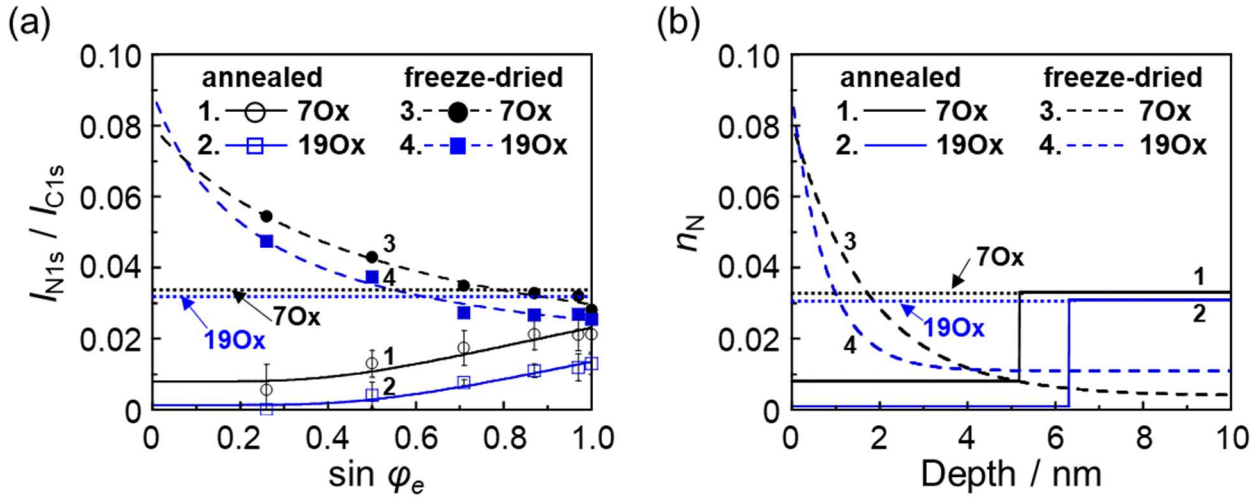

Fig. 4-10. (a) Sin φ_e dependence of I_{N1s}/I_{C1s}. Open symbol and solid lines are the experimental data and best fit results obtained on the thermal annealed films. Closed symbol and dashed lines are results for the freeze-dried films. (b) Model composition profiles of n_N against real analytical depth. Solid line and dashed line denote for the thermal annealed and freeze-dried films, respectively. Black and blue line denote 7Ox, and 19Ox, respectively.

Because there was some probability of structure rearrangement under high vacuum, such as measurement condition for XPS, NAP-XPS measurement was conducted in low vacuum of 13 mPa surrounding Ar gas or water vapor. Panels (a, b) of Fig. 4-11 shows the NAP-XPS N_{1s} spectra acquired under (a) Ar, and (b) water vapor condition, respectively. Whereas there was no signal observed under Ar, unimodal shape signals around 400 eV were clearly detected on 7Ox and 19Ox under water vapor condition. The results well agree with the previous results that the P[O(Ox)$_n$MA] was successfully segregated toward outermost region of the mixture films. Also, the peak area for the detected nitrogen signals on 7Ox film were much bigger than that for 19Ox film, meaning that P[O(Ox)$_7$MA] were segregated toward water interface with high density than P[O(Ox)$_{19}$MA].

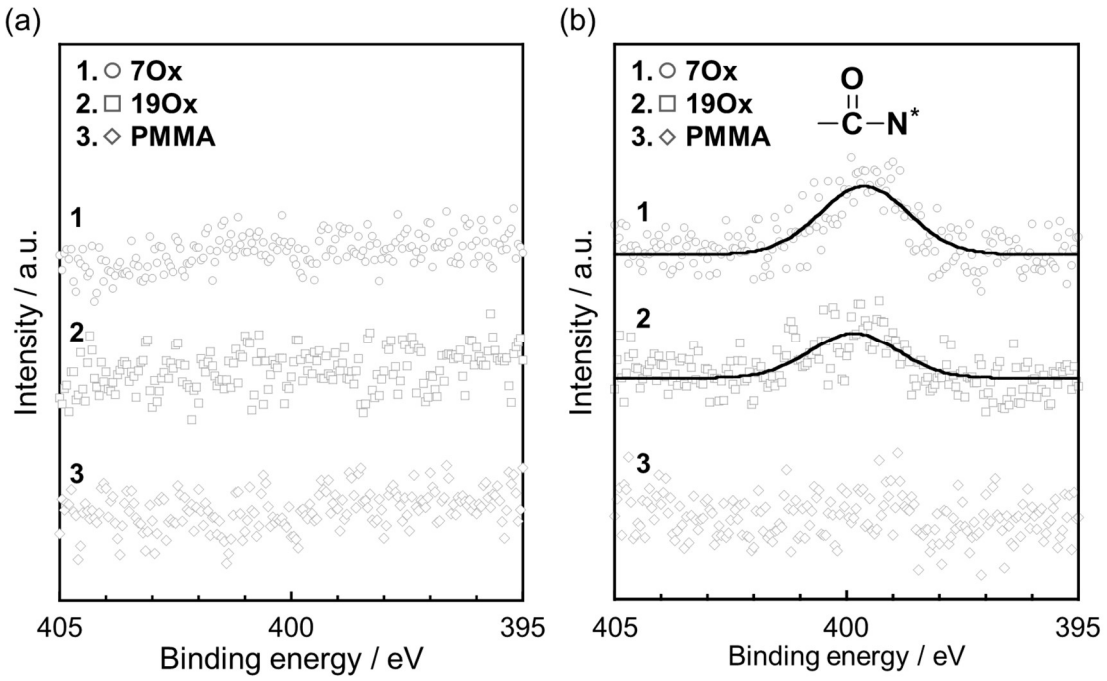

Fig. 4-11. NAP-XPS N_{1s} core level spectra for PMMA/P[O(Ox)$_n$MA] mixture and reference PMMA films under (a) Ar, and (b) water vapor condition.

4.3.5. Density profiles of the mixture films

To discuss aggregation states of the P[O(Ox)$_n$MA] in the mixture films along the depth direction, NR measurement was conducted. Panels (a–d) of Fig. 4-12 show (a, c) the reflectivity data as a function of scattering vector (q_z), and (b, d) model (b/V) profiles for the (a, b) 7Ox, and (c, d) 19Ox under air and in D_2O. For the fitting, simple 4 uniform layer model was used as described in panel (e) of Fig. 4-12. The open symbols and red solid line in Fig. 4-12(a, c) represent reflectivity data and the best-fits based on the model (b/V) profiles shown in Fig. 4-12(b, d). For both mixture films, the (b/V) value at the outermost surface regions were higher than that in bulk region, and the values were almost close to that of homo dPMMA. This means that the outermost regions of the films were mainly covered by dPMMA, and the thicknesses of the dPMMA-rich layers was thicker on 19Ox than 7Ox film. The results were in good corresponding with previous AD-XPS results.

When the films contacted with D_2O, the (b/V) values for the outermost region became smaller comparing with the values for surrounding D_2O region and bulk region, meaning that P[O(Ox)$_n$MA] which have relatively smaller (b/V) value largely aggregated at the D_2O interface. Also, the thicknesses of the outermost P[O(Ox)$_n$MA] segregation layer were evaluated to be 7.8 nm and 5.2 nm for the 7Ox and 19Ox films, respectively.

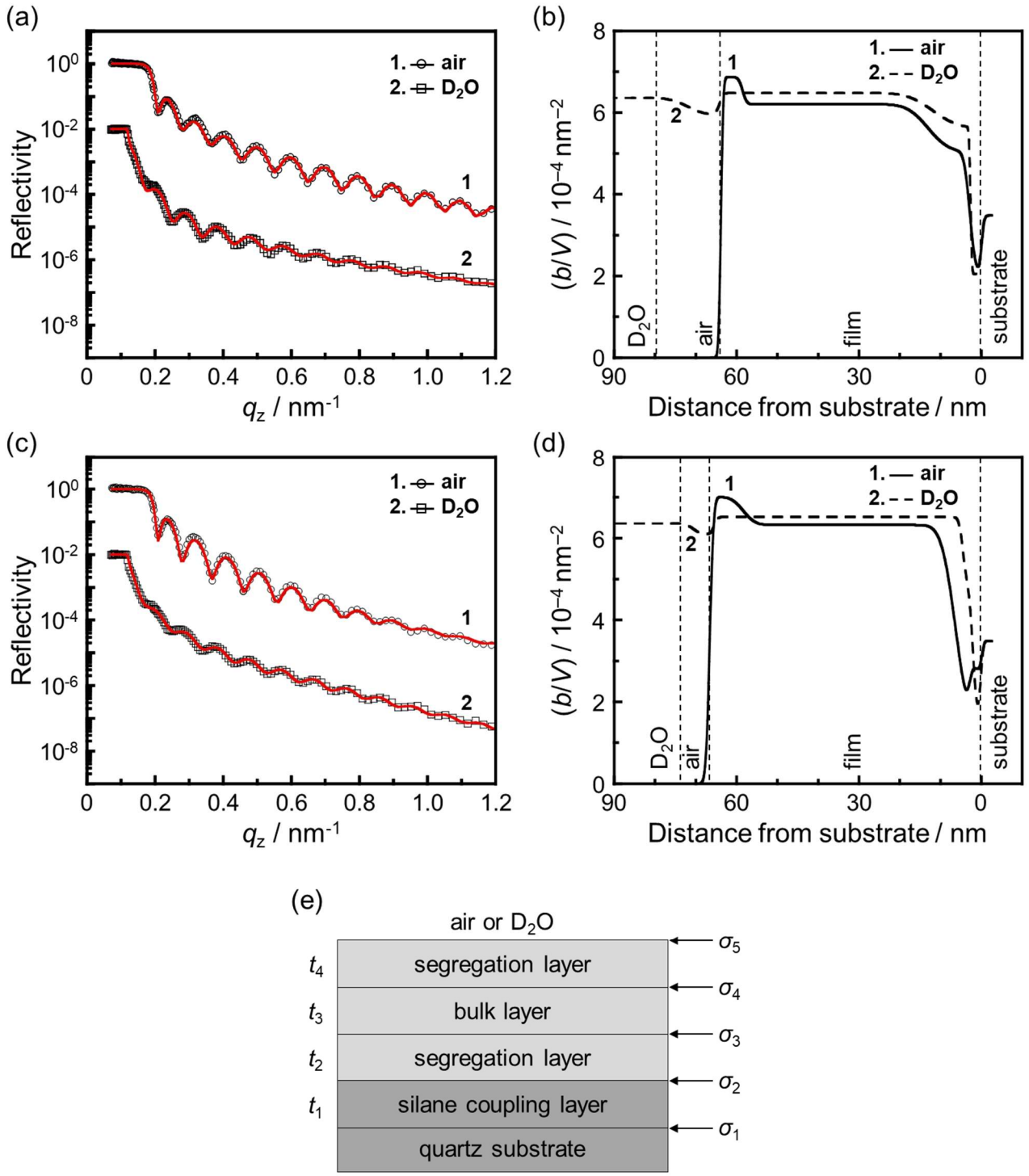

Fig. 4-12. NR curves and model *(b/V)* profiles for (a, b) 7Ox, and (c, d) 19OxB acquired under air and in D_2O environment. Open symbols denote experimental data and the red line are the calculated reflectivity based on the model (*b/V*) profiles shown in panels (b) and (d), respectively. Solid lines in panels (b, d) are the (*b/V*) profiles acquired under air and dashed lines are the profiles obtained in D_2O environment. (e) Schematic illustration of the 4 uniform layers fitting model. t_i, and σ_i denote the thickness and Gaussian roughness at each layers.

4.3.6. Mechanical properties of the thin films at water interface

Mechanical response against the mixture films was examined in water along the depth direction by using contact mode of AFM. Panel (a) of Fig. 4-13 shows the repulsive force (*F*) against indentation depth (*d*) from the water interface. The depth of zero was selected as the position where F began to increase. The increment of *F* against *d* near the water interface was much smaller in the mixture films than that in the PMMA. This result suggesting that the P[O(Ox)$_n$MA] segregation layer was well diffused at the water interface, and the extent was more remarkable in the 7Ox than 19Ox film. Subsequently, the *F*-*d* curves were converted to the Young's modulus (*E*) as a function of the *d* by using the following Hertz model; [4-30)]

$$E = (3/4) \cdot (1 - \nu^2) \cdot F / \left(r^{1/2} \cdot d^{3/2} \right) \quad (4\text{-}4)$$

where, ν and *r* are the Poisson's ratio and tip radius of the cantilever. Poisson's ratio for the PMMA/ P[O(Ox)$_n$MA] and the homo PMMA films were fixed as 0.50 and 0.33,[4-31)] respectively. Panel (b) of Fig. 4-13 shows *E*-*d* curves for the films. Because water molecules, which absorbed to the films, act as plasticizers, the depth region where the E decreased was attributed to the thickness of the diffused layer at the water interface. From the *E*-*d* curves, it is also can considered that the P[O(Ox)$_n$MA] segregation layer became more diffused and the depth region was thicker for the mixture films, especially for the 7Ox film.

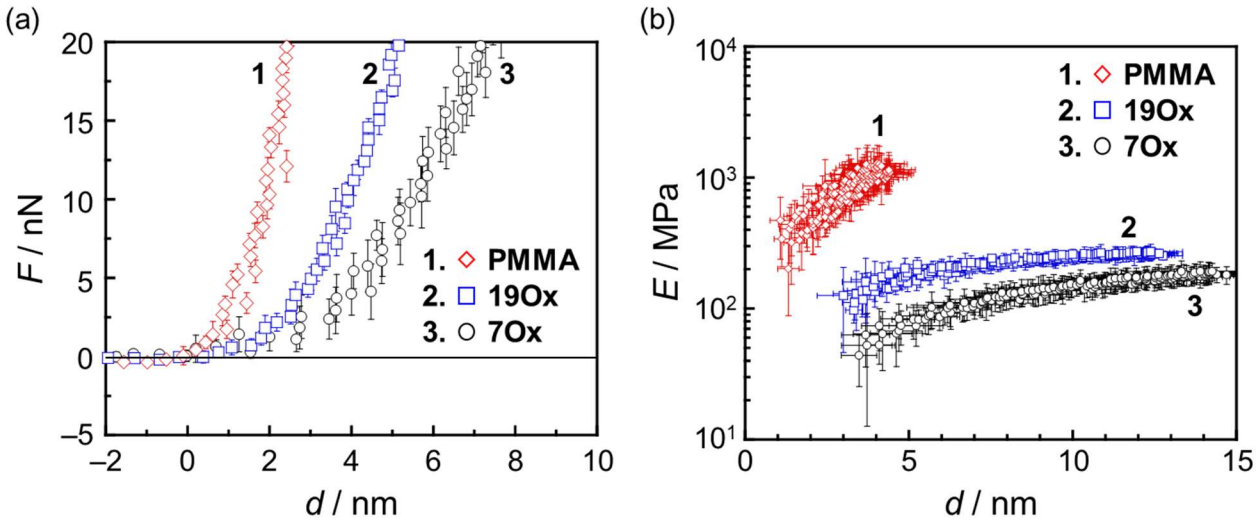

Fig. 4-13. Indentation depth (*d*) dependence of (a) repulsive force (*F*) and (b) Young's modulus (*E*) for the 7Ox (black circle), 19Ox (blue square) mixture, and reference PMMA (red rhombus) films. The zero position of the indentation depth is the location of the water/polymer interface.

4.3.7. Bioassay

Finally, surface functionality of bio-inert properties on the films were evaluated in terms of NIH3T3 cell adhesion test, FBS protein adsorption test, and platelet adhesion test. Panels (a-d) of Fig. 4-14 shows phase-contrast microscopic images for the adherent NIH3T3 cells on the films and on the TCPS. And, panel (e) of Fig. 4-14 summarizes the N_{cell} on all the films and TCPS. As the results, the N_{cell} on the mixture films were smaller than those on the PMMA film and TCPS. Especially, the N_{cell} was drastically suppressed on the 7Ox, and the adhered cell still remain their original round shape on the film. This results strongly suggest that 7Ox have an outstanding bio-inert functionality. Panel (f) of Fig. 4-14 shows the number of adsorbed serum protein on the films and reference PET sheet. From the results, it was confirmed that the mixture films inhibit the protein adsorption comparing with the homo PMMA. In particular, 7Ox expressed remarkable suppression for the adsorption of the serum proteins, which was because the thicker diffused layer was formed at the water interface.

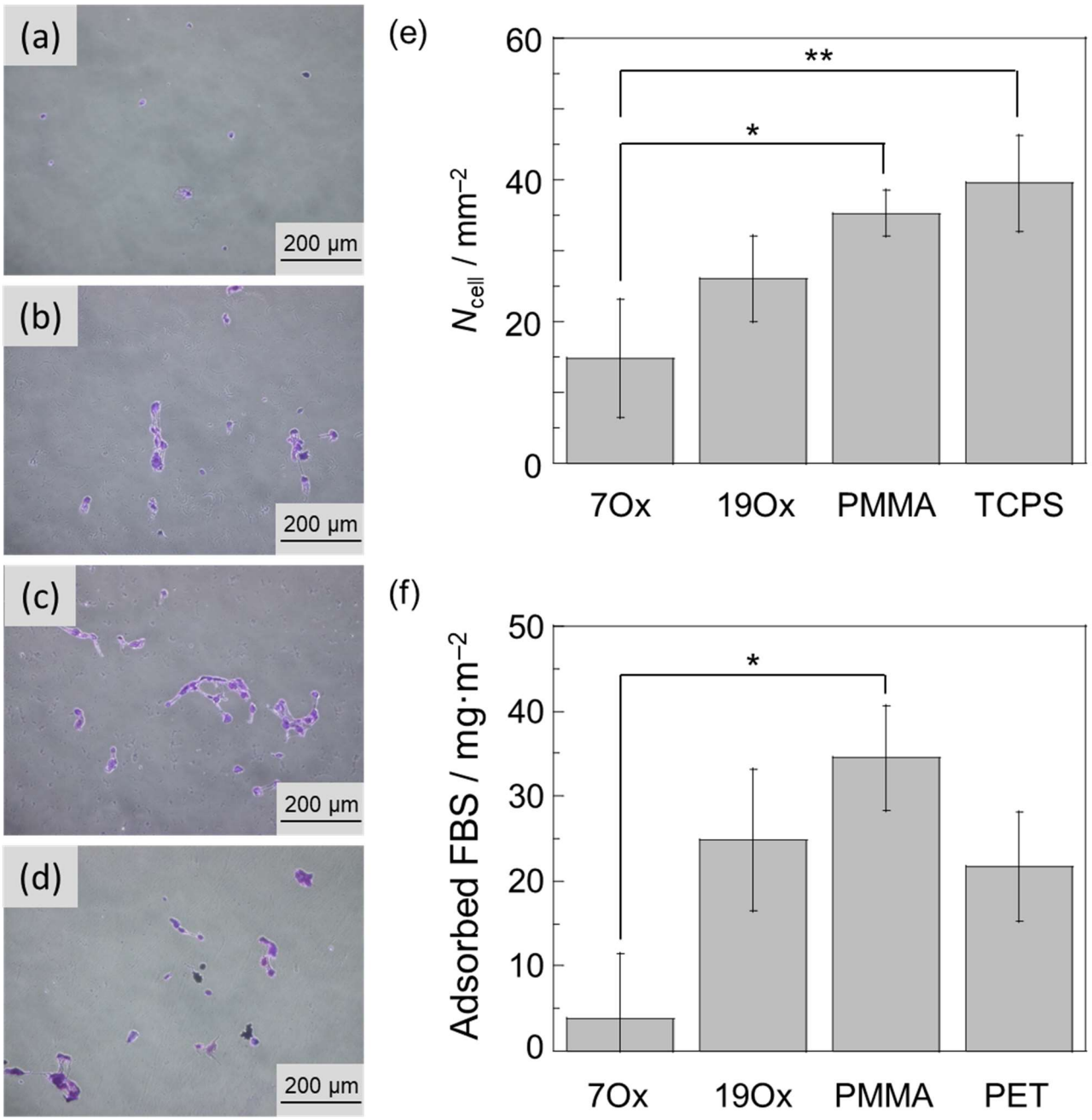

Fig. 4-14. (a–d) Phase-contrast microscopic images of adherent NIH3T3 fibroblasts on (a) 7Ox, (b) 19Ox, (c) PMMA films, and (d) tissue cultured poly(styrene) (TCPS), after staining with crystal violet. (e) The N_{cell} value on the films and TCPS plates.; ANOVA: ** $p < 0.01$, * $p < 0.05$. (f) Total amounts of adsorbed FBS proteins on the films, and on the PET sheet assessed by micro-BCA assay; ANOVA: * $p < 0.01$.

Panel (a-h) in Fig.4-15. shows the SEM images with scale bars of 100 μm and 10 μm of adherent platelets on all the mixture and homo-PMMA films and PET sheets. The number of platelets (N_{PLT}) and

their breakdown are classified into 3 categories: Type 1, the original spherical shape; Type 2, partially spread shape; Type 3, fully spread and aggregated shape. The N_{PLT} was significantly decreased on mixture films comparing with that for PMMA film and PET sheet. The results indicated that P[O(Ox)$_n$MA] segregation layers strongly suppressed the platelet adhesion on the films. In particular, in the case of 7Ox, activation of the platelets also drastically restricted. That is, formation of thicker P[O(Ox)$_n$MA] segregation and diffused layer at water interface more effectively restrained the platelet adhesion behaviors.

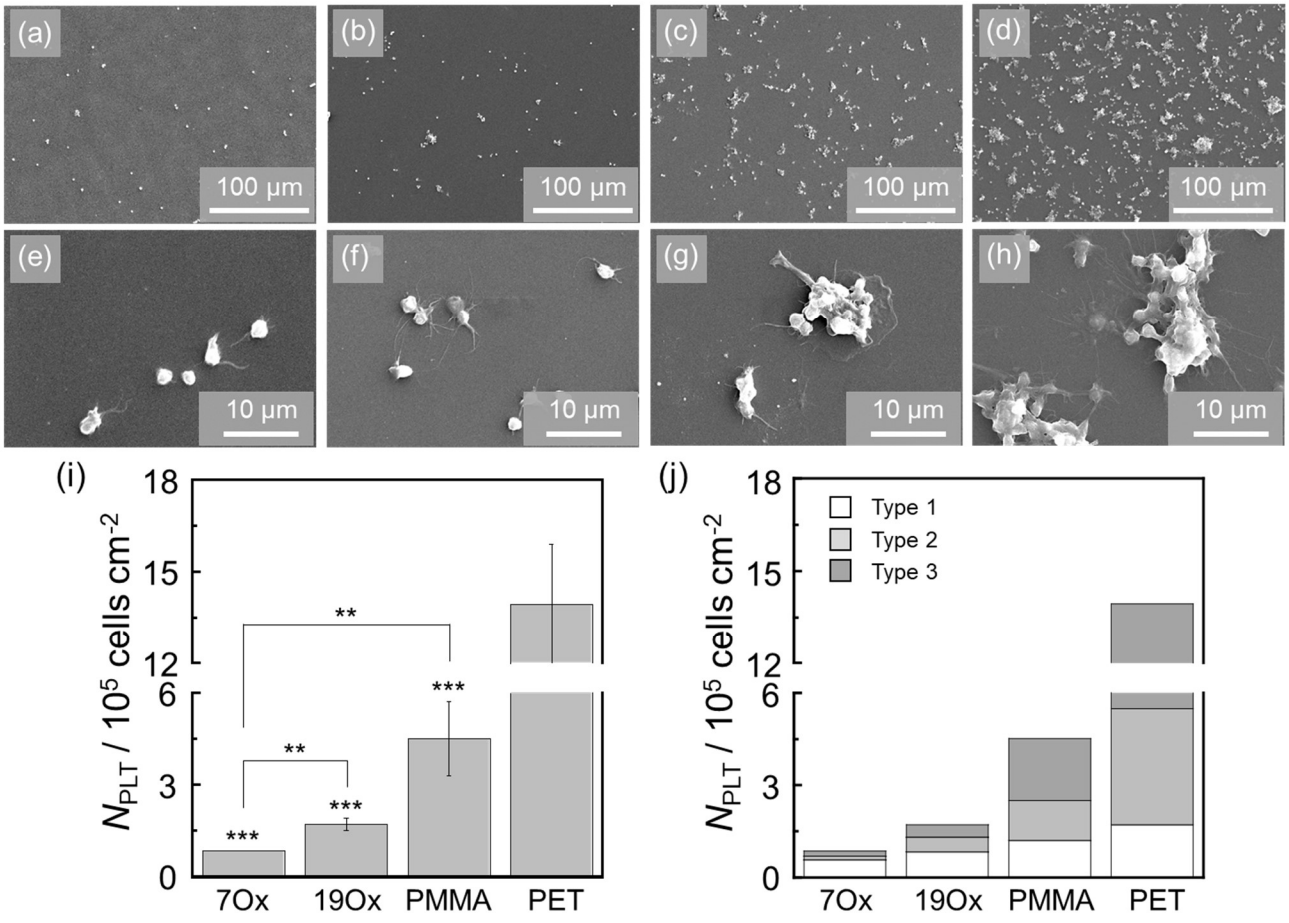

Fig. 4-15. SEM images of platelets adhered at (a, e) 7Ox, (b, f) 19Ox mixture, (c, g) homo PMMA films, and (d, h) reference PET sheets. Scale bars correspond to (a-d) 100 μm, and (e-h) 10 μm. (i) The number of adhered platelets on each sample were shown with the average values and standard deviation (n = 3). (j) The breakdown of the adhered platelets classified into 3 categories based on degree of platelet activation. ANOVA: *** $p < 0.001$, ** $p < 0.005$.

4.4. Summary

To construct stable PEtOx surface, in this chapter, P[O(Ox)$_n$MA]s, which have different lengths of oxazoline segment, were mixed to PMMA films, respectively. Then, surface aggregation states of the thin mixture films were characterized in air and water environments. At first, after thermal annealing at 423 K, P[O(Ox)$_n$MA] did not aggregated at the outmost region of the films. However, once the mixture films immersed in water, P[O(Ox)$_n$MA] were emerged toward water interface. Especially, P[O(Ox)$_7$MA], which have relatively short oxazoline side chains, strongly aggregated and successfully formed the diffused layer at the mixture film/water interface. The results imply that the extent of the surface aggregation states, and the diffused interfacial layer were changed depending on architecture of P[O(Ox)$_n$MA]. In addition, it also confirmed that the bio-inert properties were greatly improved on the interface where the thicker diffusion layer with the high density of P[O(Ox)$_n$MA] was formed near the water phase. From this study, it became convinced that the surface aggregation states and the surface functionality can be tuned by designing bottlebrush type polymer architecture.

4.5. References

4-1) Park, C. H.; Lee, S. Y.; Hwang, D. S.; Shin, D. W.; Choi, D. H.; Lee, K. H.; Kim, T. W.; Kim, T. W.; Lee, M.; Kim, D. S.; Doherty, C. M.; Thornton, A. W.; Hill, A. J., Guiver, M. D.; Lee, Y. M. Nanocrack-Regulated Self-Humidifying Membranes. *Nature*, **2016**, *532*, 480.

4-2) Lee, H.; Dellatore, S. M.; Miller, W. M.; Messersmith P. B. Mussel-Inspired Surface Chemistry for Multifunctional Coatings. *Science*, **2007**, *318*, 426.

4-3) Tung, S.; Fisher, S. L. Kotov, N. A.; Thompson, L. T. Nanoporous Aramid Nanofibre Separators for Nonaquous Redox Flow Batteries. *Nat. Commun.*, **2018**, *9*, 4193.

4-4) Yang, C.; Ding, X.; Ono, R. J.; Lee. H.; Hsu, L. Y.; Tong, Y. W.; Hedrick, J.; Yang, Y. Y. Brush-Like Polycarbonates Containing Dopamine, Cations, and PEG Providing a Broad-Spectrum, Antibacterial, and Antifouling Surface via One-Step Coating. *Adv. Mater.*, **2014**, *26*, 7346.

4-5) Kawaguchi, D.; Tanaka, K.; Takahara, A.; Tasaki, S.; Kajiyama, T. Surface Composition Control via Chain End Segregation in Blend Films of Polystyrene and Poly(vinyl methyl ether), *Macromolecules*, **2003**, *36*, 6824.

4-6) Hester, J. F.; Bannerjee, P.; Mayes, A. M. Preparation of Protein-Resistant Surfaces on Poly(vinylidene fluoride) Membranes via Surface Segregation. *Macromolecules*, **1999**, *32*, 1643.

4-7) Oda, Y.; Inutsuka, M.; Awane, R.; Totani, M.; Yamada, L. N.; Haraguchi, M.; Ozawa, M.; Matsuno, H.; Tanaka, K. Dynamic Interface Based on Segregation of an Amphiphilic Hyperbranched Polymer Containing Fluoroalkyl and Oligo(ethylene oxide) moieties. *Macromolecules*, **2020**, *53*, 2580.

4-8) Zhang, C.; Oda, Y.; Kawaguchi, D.; Kanaoka, S.; Aoshima, S.; Tanaka, K. Dynamic-Driven Surface Segregation of a Hydrophilic Component in Diblock Copolymer Films. *Chem. Lett.*, **2015**, *44*, 166.

4-9) Yamamoto, K.; Kawaguchi, D.; Abe, T.; Komino, T.; Mamada, M.; Kabe, T.; Adachi, C.; Naka, K.; Tanaka, K. Surface Segregation of a Star-Shaped Polyhedral Oligomeric Silsesquioxane in a Polymer Matrix. *Langumuir*, **2020**, *36*, 9960.

4-10) Tanaka, K.; Kajiyama, T.; Takahara, A.; Tasaki, S. A Novel Method to Examine Surface Composition in Mixtures of Chemically Identical Two Polymers with Different Molecular Weights. *Macromolecules*, **2002**, *35*, 4702.

4-11) Tanaka, K.; Kajiyama, T.; Takahara, A. Surface Molecular Aggregation Structure and Surface Molecular Motions of High-Molecular-Weight Polystyrene/Low-Molecular-Weight Poly(methyl methacrylate) Blend Films. *Macromolecules*, **1998**, *31*, 863.

4-12) Blaber, S.; Mahmoudi, P.; Spencer, R. K. W.; Matsen, M. W. Effect of Chain Stiffness on the Entropic Segregation of Chain ends, to the Surface of a Polymer Melt. *J. Chem. Phys.*, **2019**, *150*, 014904.

4-13) Sugimoto, S.; Oda, Y.; Hirata, T.; Matsuyama, R.; Matsuno, H.; Tanaka, K. Surface Segregation of a Branched Polymer with Hydrophilic Poly[2-(2-ethoxy)ethoxyethyl vinyl ether] Side Chains. *Polym. Chem.*, **2017**, *8*, 505.

4-14) Hirai, T.; Huan, L.; Ohta, Y.; Yokozawa, T.; Tanaka, K. Surface Segregation of Well-defied N-Substituted Hyperbranched Polyamides in Linear Polymer Matrix. *Chem. Lett.*, **2011,** *40,* 366.

4-15) Mei, H.; Laws, T. S.; Mahalik, J. P.; Li, J.; Mah, A. H.; Terlier, T.; Bonnesen, P.' Uhrig, D. Kumar, R.; Stein, G. E.; Verduzco, R. Entropy and Enthalpy Mediated Segregation of Bottlebrush Copolymers to Interfaces. *Macromolecules*, **2019**, *52*, 8910.

4-16) Yokoyama, H.; Miyamae, T.; Han, S.; Ishizone, T.; Tanaka, K.; Takahara, A.; Torikai, N. Spontaneously Formed Hydrophilic Surfaces by Segregation of Block Copolymers with Water-Soluble Blocks. *Macromolecules*, **2005**, *38*, 5180.

4-17) Inutsuka, M.; Yamada, N. L.; Ito, K.; Yokoyama, H. High Density Polymer Brush Spontaneously Formed by the Segregation of Amphiphilic Diblock Copolymers to the Polymer/Water Interface.

ACS Macro Lett., **2013**, *2*, 265.

4-18) Hong, J. H.; Totani, M.; Kawaguchi, D.; Masunaga, H.; Yamada, N. L.; Matsuno, H.; Tanaka, K. Design of a Bioinert Interface Using an Amphiphilic Block Copolymer Containing a Bottlebrush Unit of Oligo(oxazoline). *ACS Appl. Bio Mater.*, **2020**, *3*, 7363.

4-19) Tateishi, Y.; Kai, N.; Noguchi, H.; Uosaki, K.; Nagamura, T.; Tanaka, K. Local Conformation of Poly(methyl methacrylate) at Nitrogen and Water Interfaces. *Polym. Chem.*, **2010**, *1*, 303.

4-20) Matsuno, H.; Tsukamoto, R.; Shimomura, S.; Hirai, T.; Oda, Y.; Tanaka, L. Platelet-Adhesion Behavior Synchronized with Surface Rearrangement in a Film of Poly(methyl methacrylate) Terminated with Elemental Blocks. *Polym. J*, **2016**, *48*, 413.

4-21) Matsuno, H.; Totani, M.; Yamamoto, A.; Haraguchi, M.; Ozawa, M.; Tanaka, K. Water-Induced Surface Reorganization of Bioscaffolds Composed of an Amphiphilic Hyperbranched Polymer. *Polym. J*, **2019**, *51*, 1045.

4-22) Mitra, I.; Li, X.; Pesek, S. L.; Makarenko, B.; Lokitz, B. S.; Uhrig, D.; Ankner, J. F.; Verduzco, R.; Stein, G. E. Thin Film Phase Behavior of Bottlebrush/Linear Polymer Blends. *Macromolecules*, **2014,** *47,* 5269.

4-23) Verduzco, R.; Li, X.; Pesek, S. L.; Stein, G. E. Structure, Function, Self-assembly, and Application of Bottlebrush Copolymers. *Chem. Soc. Rev.*, **2015,** *44,* 2405.

4-24) Owens, D. K.; Wendt, R. C. Estimation of the Surface Free Energy of Polymers. *J. Appl. Polym. Sci.*, **1969,** *13,* 1741.

4-25) Kwok, D. Y.; Neumann, A. W. Contact Angle Measurement and Contact Angle Interpretation. *Adv. Colloid Interface Sci.*, **1999,** *81,* 167.

4-26) Wijnans, S.; Gans, B. J.; Wiesbrock, F.; Hoogenboom, R.; Schubert, U. S. Characterization of a Poly(2-oxazoline) Library by High-Throughput, Automated Contact-Angle Measurements and Surface-Energy Calculations *Macromol. Rapid Commun.*, **2004,** *25,* 1958.

4-27) Janczuk, B.; Bialopiotrowicz, T.; Zdziennicka, A. Some Remarks on the Components of the

Liquid Surface Free Energy. *J. Colloid Interface Sci.*, **1999,** *211,* 96.

4-28) Patel, D. I.; Dietrich, P.; Thißen, A.; Linford, M. R. Near Ambient Pressure X-ray Photoelectron Spectroscopy (NAP-XPS). Characterization of Non-Traditional Materials with the SPECS EnviroESCA Instrument. *J. Electron Spectrosc. Relat. Phenom.*, **2019**, *26*, 162.

4-29) Dietrich, P. M.; Bahr, S.; Yamamoto, T.; Meyer, M.; Thissen, A. Chemical Surface Analysis on Materials and Devices under Functional Conditions – Environmental Photoelectron Spectroscopy as Non-destructive Tool for Routine Characterization. *J. Surf. Anal.* **2019**, *231*, 118.

4-30) Itagaki, N.; Kawaguchi, D.; Oda, Y.; Nemoto, F.; Yamada, N. L.; Yamaguchi, T.; Tanaka, K. Surface Effect on Frictional Properties for Thin Hydrogel Films of Poly(vinyl ether). *Macromolecules*, **2019,** *52,* 9632.

4-31) Tanaka, K.; Fujii, Y.; Atarashi, H.; Akabori, K.; Hino, M.; Nagamura, T. Nonsolvents Cause Swelling at the Interface with Poly(methyl methacrylate) Films. *Langmuir*, **2008**, *24*, 296.

Chapter 5. Water vapor-induced surface segregation in thin films of amphiphilic type poly(2-ethyl-2-oxazoline) derivatives

5.1. Background

Surface chemical composition in the multicomponent polymer systems, such as block copolymer and polymer blend, is well known to be different comparing with the bulk composition.[5-1)] The phenomenon is a crucial factor to express unique surface properties like surface wettability, adhesion properties, and biocompatibility.[5-2~4)] So far, it has been revealed that the surface chemical composition is controlled by enthalpic interaction, entropic effects, and the combination of the factors between the polymeric materials with the surrounding medium.[5-5~9)] At the air interface, for examples, polymer segments having lower surface free energy values localized at the outermost surface region.[5-5,6)] On the other hand, once the surrounding medium is changed to water, a component or a part of polymer segment having higher affinity with water preferentially aggregated near the water phase.[5-8,9)] These tendencies are thermodynamically spontaneous phenomena and occur to minimize interfacial fee energy between the polymers and surrounding mediums.

In reality, like nonsolvent-induced phase separation (NIPS)[5-10~14)] and vapor-induced phase separation (VIPS) methods[5-15~17)], there have been some development to tune the surface chemical compositions using nonsolvent or its vapor to introduce surface functionality such as antifouling properties on polymer membranes. In a previous study, H. Matsuyama *et al.* prepared poly(vinylidene fluoride) (PVDF)/poly(ethylene glycol) methyl ether methacrylate-poly(methyl methacrylate) [P(PEGMA-*r*-MMA)] blend solutions which were dissolved in dimethylacetamide. Then, surface P(PEGMA-*r*-MMA) aggregated antifouling PVDF membranes were obtained after immersing solvent casted blend solution into water bath to induce phase separation in water.[5-10)]

In this chapter, I focus on the effects of the two kinds of film annealing methods on surface aggregation states of the PMMA-*b*-P[O(Ox)$_n$MA] films; (1) thermal annealing method, (2) water vapor annealing method. In Chapter 3, the thin film of amphiphilic PMMA-*b*-P[O(Ox)$_9$MA] was prepared and its aggregation states and physical properties were characterized. As a result, it was revealed that the P[O(Ox)$_9$MA] block first hided inside the bulk region after thermal annealing, and then, some of the P[O(Ox)$_9$MA] block emerged toward the outermost surface region after contacting with water. However, it was believed that there is still have a possibility to increase the oxazoline density on the block copolymer films, and one of the key factor is to find how to increase probability to contact P[O(Ox)$_n$MA] block in the film and water molecules. In a previous study, K. Tanaka *et al.* reported that the as cast PMMA film uptake much amount of water molecules comparing with thermal annealed PMMA films. This is because there were increase pathway to penetrate water molecules inside the film.[5-18] Motivated from the phenomenon, the effect of annealing method under water vapor environment is planned to examined on a basis of surface aggregation states of the P[O(Ox)$_n$MA] block. Therefore, surface characterization for thin films prepared after the water vapor annealing method was going to conducted in this chapter comparing against thin films prepared by the typical thermal annealing method.

5.2. Experimental

5.2.1. Materials

PMMA-*b*-P[O(Ox)$_n$MA]s were polymerized by combination of LCROP and ATRP. Detail synthetic procedure and the results were described in chapter 2. Table 5-1 summarizes the molecular information of the synthetized polymers used in this study.

Table 5-1. Structure characteristics of the synthesized block copolymers.

Polymer	$M_{n,NMR}$[a)]	Degree of polymerization[a)]			M_n[b)]	M_w/M_n[b)]	T_g[c)] / K
		m	*l*	*n*			
PMMA-*b*-P[O(Ox)$_{13}$MA]	36,700	212	11	13	31,200	1.32	316, 383
PMMA-*b*-P[O(Ox)$_9$MA]	30,100	212	9	9	28,700	1.36	303, 365

[a)] Determined by ^{1}H NMR. [b)] Determined by SEC with PMMA standards. [c)] Determined by DSC.

2-butanone (methyl ethyl ketone, MEK, purity > 99.0 %), and potassium chloride (KCl, purity > 99.5 %) was purchased from FUJIFILM Wako Pure Chemical Industries Ltd. The chemicals were used as received.

5.2.2. Thin film preparation

Solid substrates such as Si wafer were hydrophobized with chloro(decyl)dimethylsilane in a same manner. The detail procedure was described in chapter 3. 2 wt % of block copolymer/MEK solution was spin-coated on the solid substrate at 2000 rpm for 60 s by using a 1H-D7 spin-coater (MIKASA). Fig. 5-1 shows the schematic illustration from the spin coating to various annealing procedures. Panel (a) of Fig. 5-1 shows the schematic illustration of a water vapor annealing method using the thin films just after the spin-coating. To make the water vaporized environment, saturated KCl aqueous solution

was placed inside the humid box.[5-19] Relative humidity (RH) inside the humid box increased upto 95 % at RT after 24 h. Subsequently, the spin-coated thin films were moved inside the humid box, and the films were annealed at 323 K for 6 h. As control groups, thin films of the block copolymer were annealed at (T_g +20) K for 12 h under high vacuum condition, and also, thin films, which was annealed under high vacuum and sequentially was annealed under water vapor, were prepared as depicted in panels (b, c) of Fig. 5-1. For the convenience, the thin films of PMMA-*b*-P[O(Ox)$_n$MA] annealed under the water vapor were called 13V, and 9V. The 13 and 9 denote the degree of polymerization (n) of oxazoline units at the side chain. Also, the thin films thermally annealed under high vacuum were called 13T and 9T. At last, the thin films thermally annealed under high vacuum and water vapor sequentially were denote as 13TV and 9TV.

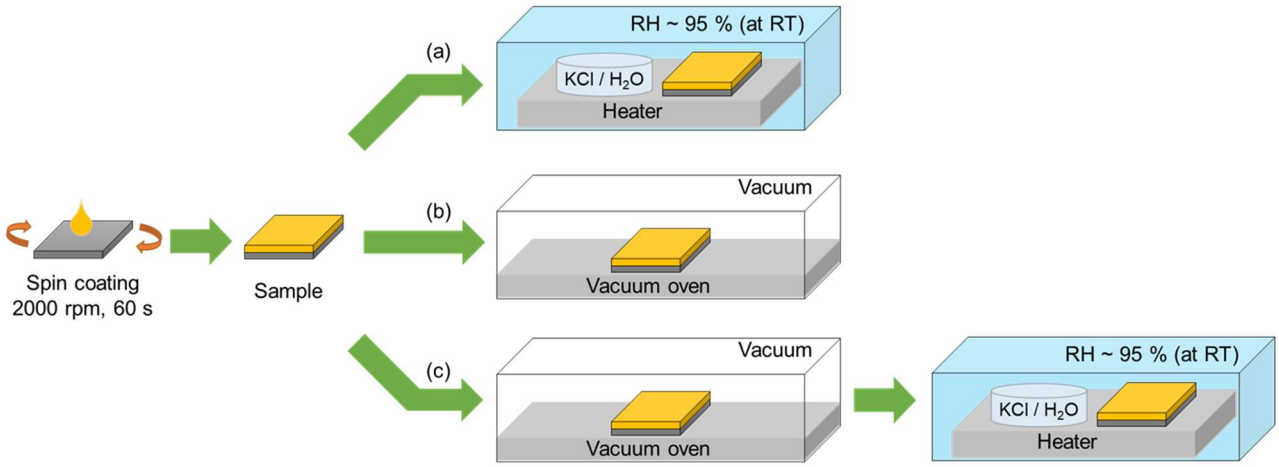

Fig. 5-1. Schematic illustration for the thin film preparation. (a) water vapor annealing at 323 K for 6 h, (b) thermal annealing at (T_g +20) K for 12 h, and (c) the thermal annealing, subsequently, water vapor annealing with the described condition.

5.2.3. Surface characterization

The surface morphology of the thin films on Si-wafers was observed by Cypher ES AFM using an AC mode in air and water at 298 K. Si micro-fabricated cantilevers tip coated with Al were used. Spring constants and resonance frequencies of the cantilevers for each environment were 40 N·m^{-1} and 312 kHz

under air and 1.6 $N \cdot m^{-1}$ and 23 kHz in water. Before the AFM observation in water, the films were immersed in water for 24 h. The surface chemical composition of the block copolymer films was evaluated by AD-XPS by using the PHI 5000 VersaProbe III. The emission angle (φ_e) was set in the range of 15 to 90°. For the measurement, Al-Kα anode source was used at 15 kV and 25 W. The XPS peaks were calibrated to the neutron carbon peak corresponding at binding energy of 285.0 eV. Surface hydrophilicity and its sustainability in water were examined by the static contact angle measurement using the DropMaster 500 and 2 μL of air bubble as a probe. The initial air bubble contact angle (θ_a) values were obtained at 2 min after immersing in water, and then, the contact angles were recorded in every 1 h until 24 h. The quality of surface diffusion on the films was discussed on a basis of force (F)-distance (d) measurement using contact mode of the Cypher ES AFM.

5.3. Results and discussion

5.3.1. Surface aggregation states of the films

As a first step to examine the surface aggregation states of the block copolymer films, the morphology of the outermost surface region was observed by AFM. Fig. 5-2 shows (a-f) topological and (g-l) phase images for all the film surfaces. The R_{RMS} for the (a) 13T, (b) 13TV, (c) 13V, (d) 9T, (e) 9TV, and (f) 9V were 0.51 nm, 1.21 nm, 1.28 nm, 0.48nm, 0.86 nm, and 1.26 nm, respectively. These results show that the film surfaces became relatively rough when the films were annealed under water vapor condition, however, the extent of roughness was still sufficiently small to conduct surface sensitive characterization. Also, in the phase images, some phase contrast was observed, however, the extent was not so strong and irregular like phase separated surfaces.

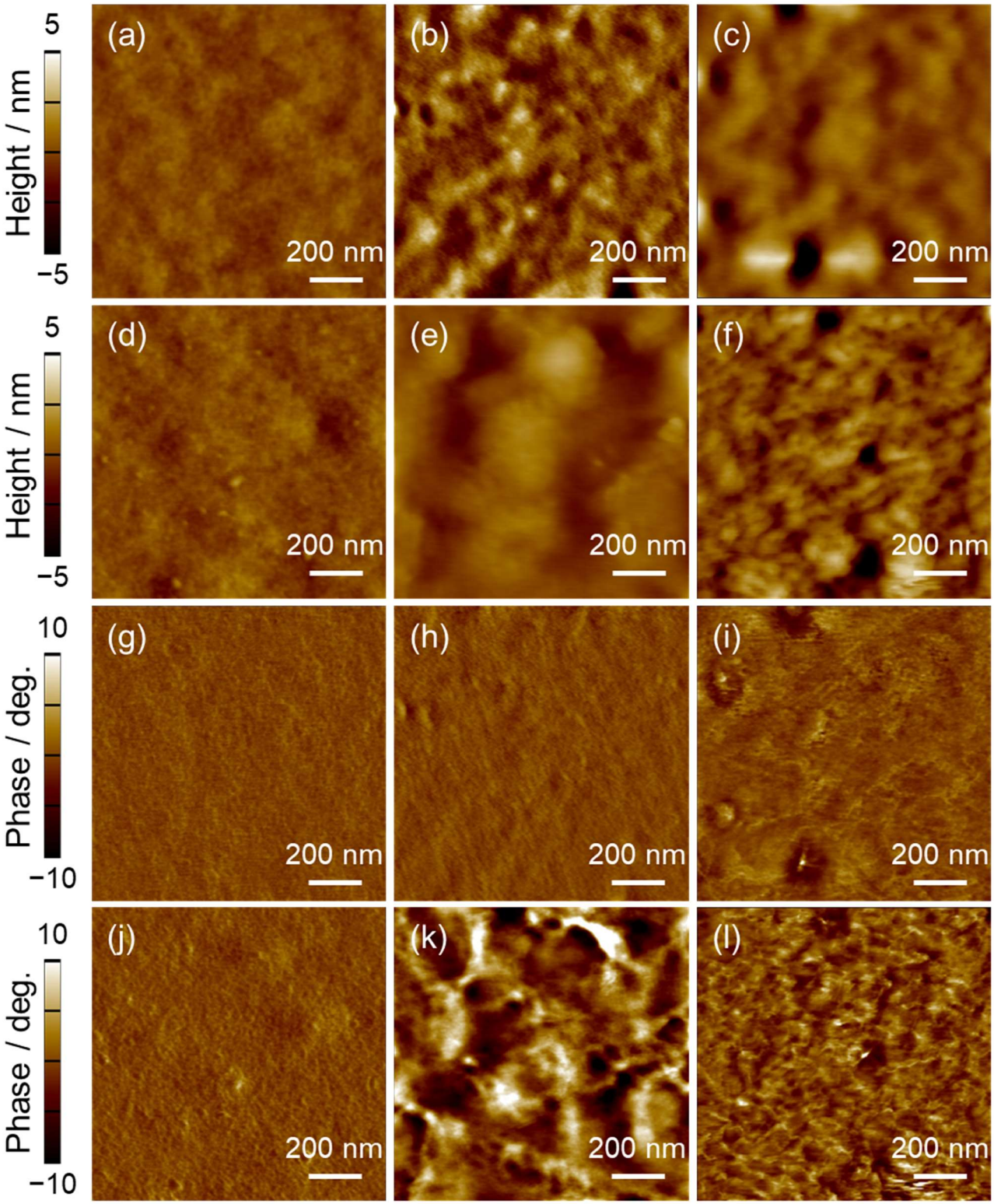

Fig. 5-2. AFM (a-f) topographic and (g-l) phase images for the thin films of (a, g) 13T, (b, h) 13TV, (c, i) 13V, (d) 9T, (e, k) 9TV, and (f, l) 9V.

To obtain concentration profile for the P[O(Ox)$_n$MA] block from the outermost surface region of the film, AD-XPS measurement was conducted. Fig. 5-3 shows the representative XPS spectra for the thin films of (a-b) PMMA-*b*-P[O(Ox)$_{13}$MA], and (c-d) PMMA-*b*-P[O(Ox)$_9$MA] annealed with the various condition. In the case of N_{1s} spectra as shown in panels (a, c) of Fig. 5-3, all the block copolymer films showed a signal at 400 eV indicating tertiary amine (N–C=O) of the oxazoline units. Likewise, the C_{1s} spectra described in panels (b, d) of Fig. 5-3 also included signals for the amine (C–N), and amide(N–(C=O)) of oxazoline units at the binding energy of 286.0, and 287.7 eV, meaning that the P[O(Ox)$_n$MA] block was existed near the surface region. Interesting feature was that the intensity of the signals for the oxazoline units was different depending on the annealing methods.

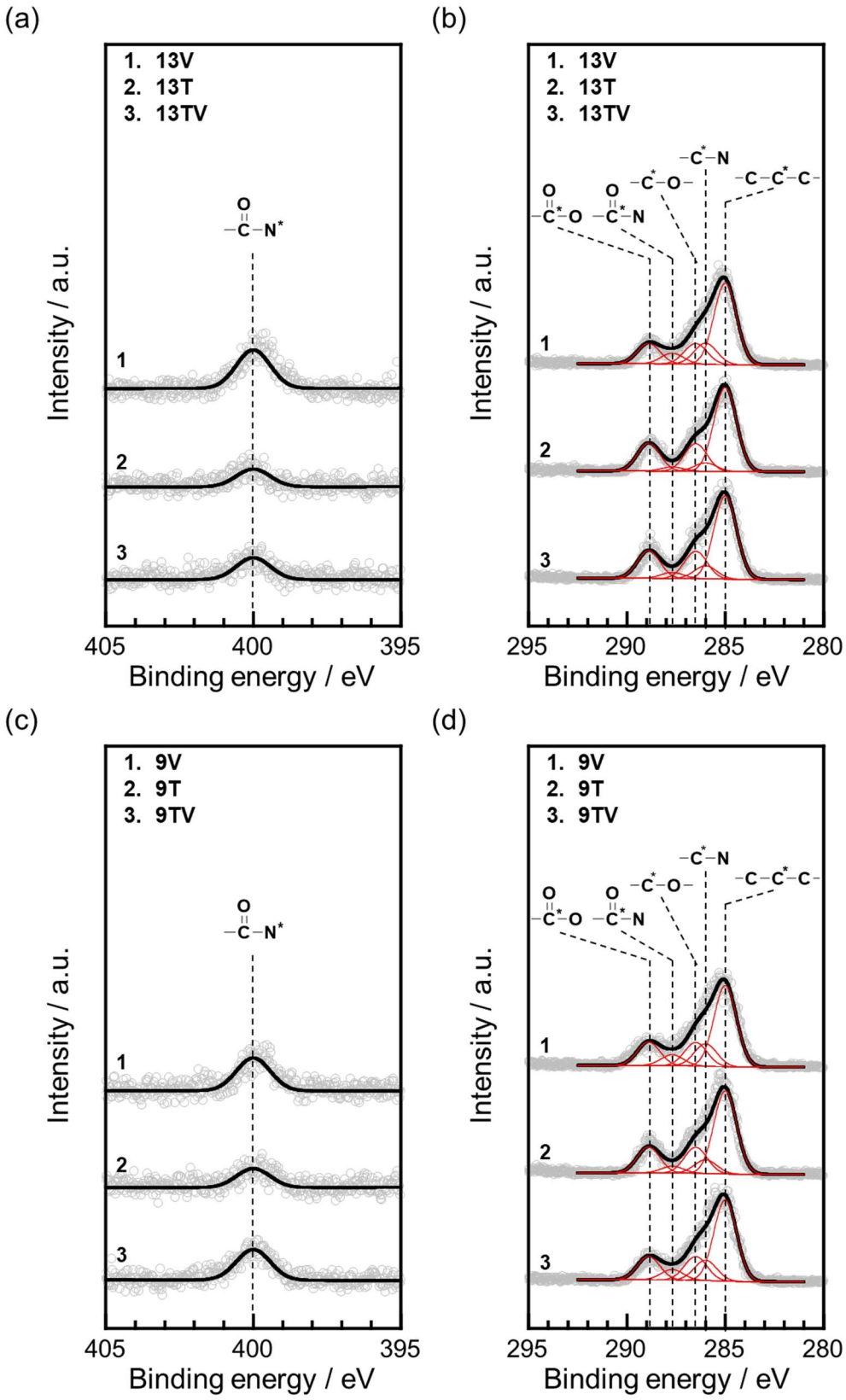

Fig. 5-3. XPS (a, c) N_{1s}, and (b, d) C_{1s} spectra for the (a, b) PMMA-*b*-P[O(Ox)$_{13}$MA], and (c, d) PMMA-*b*-P[O(Ox)$_9$MA] thin films with the various annealing conditions at φ_e=90°. The black solid line in panel (b) was decomposed to the five red solid lines.

Panels (a, b) of Fig. 5-4 show the I_{N1s}/I_{C1s} for the block copolymer films as a function of sin φ_e. There was two common features observed in both figures. In the cases of 13T and 9T, the intensity ratios gradually decreased with decreasing the sin φ_e, meaning that, P[O(Ox)$_n$MA] blocks were not segregated toward surfaces but hided inside the bulk regions. In addition, in the cases of 13V and 9V, the intensity ratios were near the theoretical bulk values of 0.078 for PMMA-*b*-P[O(Ox)$_{13}$MA] and 0.053 for PMMA-*b*-P[O(Ox)$_9$MA] in all range of the sin φ_e. These results imply that the P[O(Ox)$_n$MA] blocks were well dispersed on the film surfaces. On the other hand, there was a different feature was observed on the 13TV and 9TV. In the case of 13TV, the intensity ratios slightly increased comparing with the value for the 13T. Whereas, the intensity ratios for the 9TV significantly increased and almost comparable with that for 9T and 9V. To understand the difference, we tried to make sure the surface structure on the 13T and 9T films on the basis of the relation between the I_{N1s}/I_{C1s} and the real analytical depth by using the following fitting equation and the model composition profiles;

$$\frac{I_{N1s}}{I_{C1s}} = \frac{\int_0^\infty [n_N(z)\cdot\exp(-z/\lambda_N \sin\varphi_e)]dz}{\int_0^\infty [n_C(z)\cdot\exp(-z/\lambda_C \sin\varphi_e)]dz} \quad (5\text{-}1)$$

$$n_N(z) = \begin{cases} n_{N,s} & (z < z_i) \\ n_{N,\infty} & (z > z_i) \end{cases} \quad (5\text{-}2)$$

where z, λ_i, $n_i(z)$, $n_{N,s}$ and $n_{N,\infty}$ are the real analytical depth, inelastic mean-free path of the photoelectrons, the atomic fraction of *i* component, and the nitrogen atomic fraction at the outermost surface and inside the bulk region, respectively. The solid curves in panels (a, b) of Fig. 5-4 are the best-fit results on the basis of model composition profiles as shown in panels (c, d) of Fig. 5-4. As the results, the obtained z value was 6.1 nm and $n_{N,s}$ was almost equal to zero for the 13T, however, the values of z and $n_{N,s}$ for the 9T were 5.2 nm, 1.0×10^{-2}, respectively. These results suggest the close to the homogeneous PMMA wetting layer was thickly formed on 13T than 9T. From the results, it was deduced that the development of the PMMA wetting layer restricted the segregation of the P[O(Ox)$_n$MA] blocks

under water vapor, and this was because the water vapor became hard to penetrated inside the bulk from the film surface.

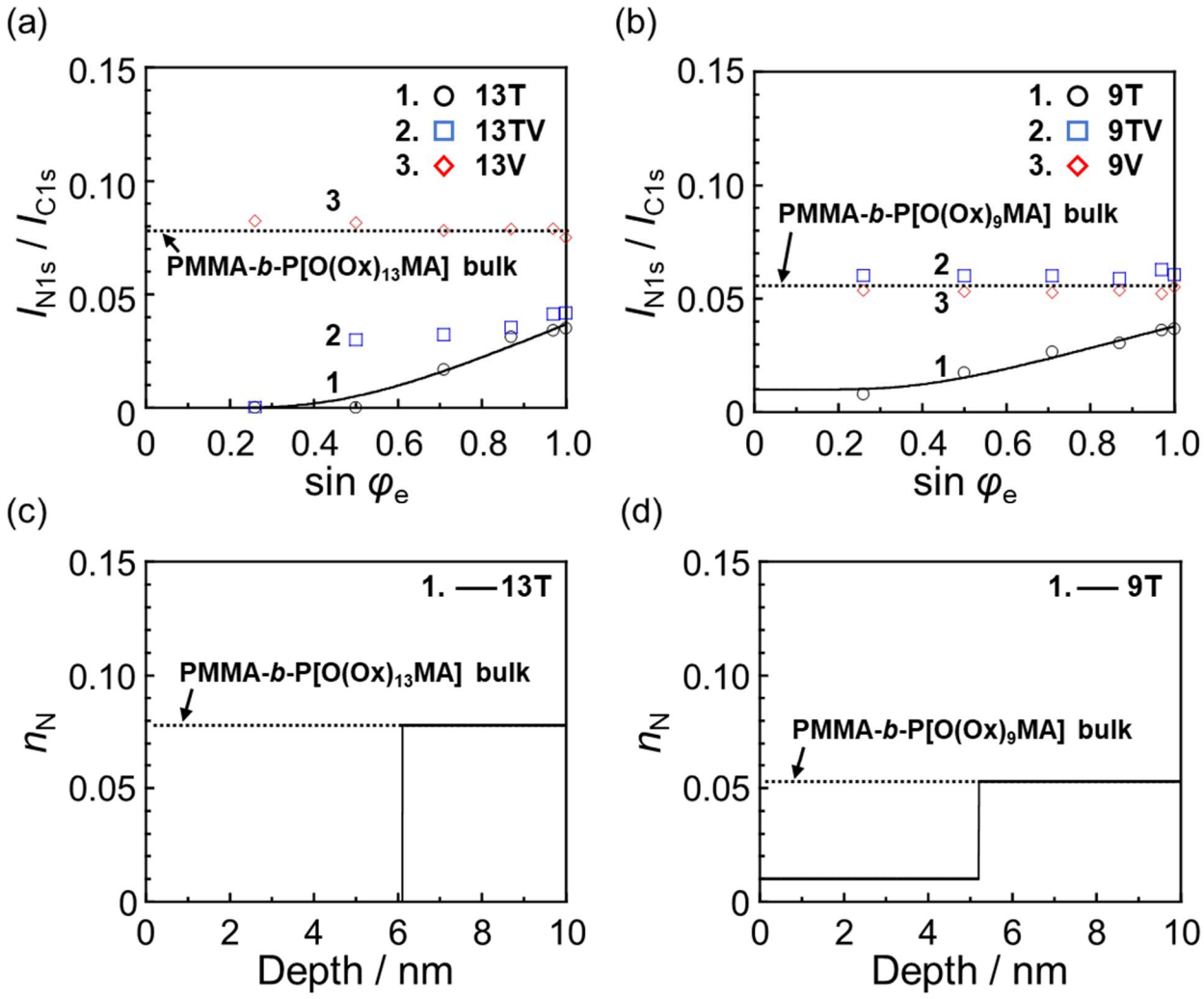

Fig. 5-4. Integral intensity ratio of all nitrogen (N_{1s}) versus all carbon (C_{1s}) for the (a) PMMA-*b*-P[O(Ox)$_{13}$MA], and (b) PMMA-*b*-P[O(Ox)$_9$MA] thin films as a function of sin φ_e. The blue solid lines of the panels (a, b) are the best-fit results on a basis of model composition profiles of nitrogen atomic fraction (n_N) as shown in panels (c, d).

5.3.2. Film stability and surface hydrophilicity in water

To examine surface hydrophilicity of the films and their stability and in water, the air bubble contact angle measurement against film surface was conducted as a function of immersion time. Panel (a) of

Fig. 5-5 shows the time dependence of θ_as for the (a) PMMA-*b*-P[O(Ox)$_{13}$MA] thin films which were thermally annealed under high vacuum or annealed under water vapor condition. In 2 min of immersion time in water, the θ_a was increase to 129.4 ± 2.5 and 138.4 ± 1.3° for 13T and 13V, respectively. Taking into account that the theoretical values of $\theta_{a(t=0\ h)}$ were 114.0 ± 0.4 and 122.7 ± 0.7° for 13T and 13V, the surface structure started to reorganize rapidly after contacting with water. After then, during 24 h, the θ_a values were unchanged within experimental error, meaning that, the films were stable in water at least 24 h. Also, the $\theta_{a(t=24\ h)}$ for the 13V was 138.4 ± 1.3°, and this was were much bigger over 10° than the values of 127.6 ± 0.6° for the 13T. This might because, the extent of segregation of the P[O(Ox)$_{13}$MA] toward the film surfaces was larger on 13V than that on 13T. In a similar manner, θ_a for the PMMA-*b*-P[O(Ox)$_9$MA] thin films drastically increased in the short time, and then, the values were keep sustained around $\theta_{a(t=24\ h)}$s of 131.8 ± 0.5 for 9T, and 136.1 ± 0.9° for 9V as shown in panel (b) of Fig. 5-5 for 24 h. In addition, the θ_as for the 9V were larger than that for 9T, however, the differences were relatively small within 5°.

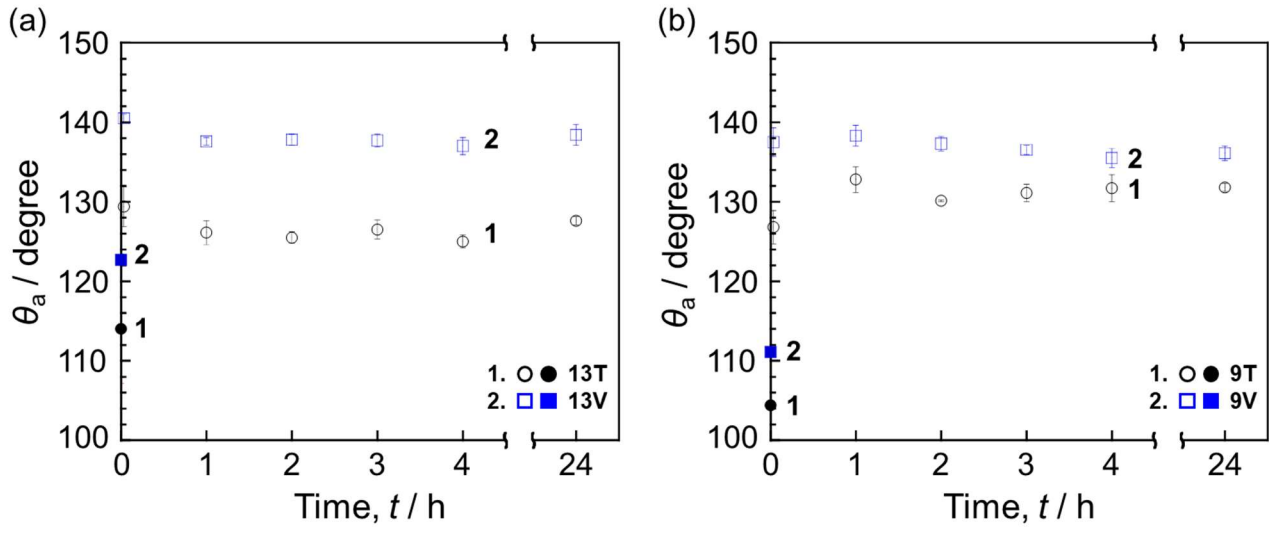

Fig. 5-5. The θ_a for the thin film of (a) PMMA-*b*-P[O(Ox)$_{13}$MA] and (a) PMMA-*b*-P[O(Ox)$_9$MA], which were thermal annealed under high vacuum or water vapor condition, as a function of immersion time in water. Closed shapes at $t = 0$ are the theoretical value ($\theta_{a(t=0\ h)}$), obtained by 180 − θ_w.

5.3.3. Formation of diffused layer at water interface

Fig. 5-6 shows AFM (a-d) topological, and (e-h) phase images for the block copolymer films which were immersed in water for 24 h. The R_{RMS} for the (a) 13T, (b) 13V, (c) 9T, and (d) 9V were 1.29 nm, 0.77 nm, 0.57 nm, and 0.57 nm, respectively. Except the 13T, the other film surfaces were reorganized to smoother interfaces facing with water. Also, in the phase images for the (f) 13V, (g) 9T, and (h) 9V, there were featureless, meaning that, the homogeneous interfaces were formed at the interface. On the other hand, in the case of 13T shown in panels (a, e) of Fig. 5-6, the observed film surface was relatively rough and there was strong contrast in the phase image. Considering the relatively lower surface hydrophilicity of the 13T in water, this seemed to be due to insufficient formation of the P[O(Ox)$_{13}$MA] diffusion layer at the interface.

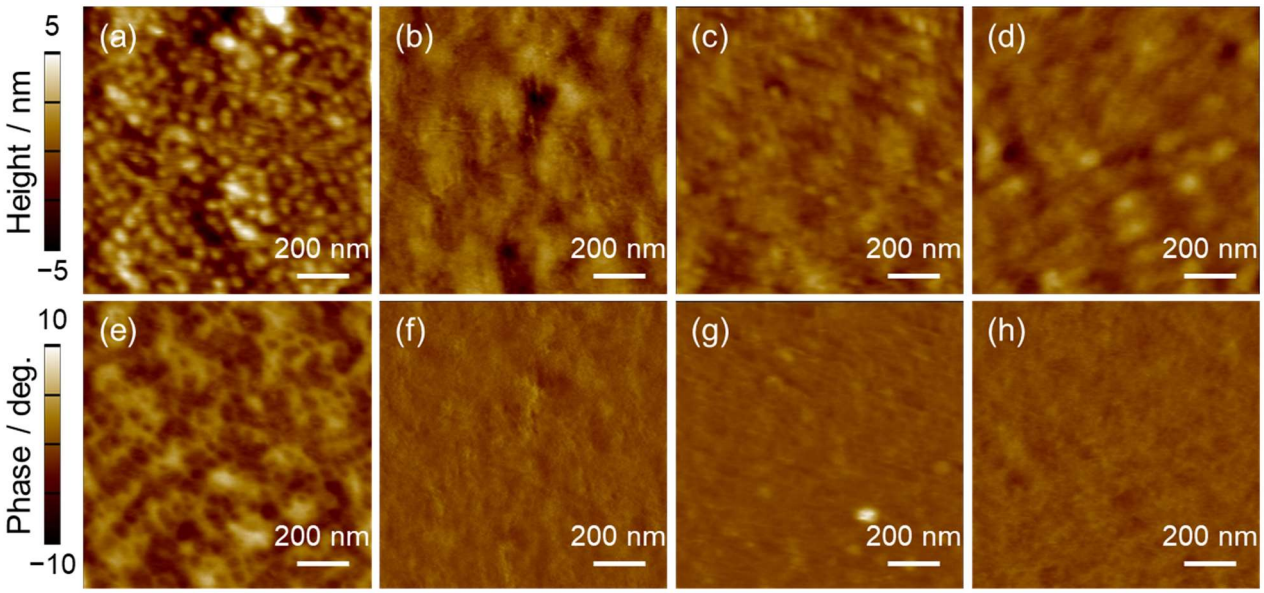

Fig. 5-6. AFM (a-d) topographic, and (e-h) phase images for the thin films of (a, e) 13T, (b, f) 13V, (c, g) 9T, (d, h) 9V.

In Chapter 3, it was revealed that the surface region of the PMMA-*b*-P[O(Ox)$_9$MA] film was swell and formed a certain degree of diffusion layer against water phase.[5-9] And, it was also known that the

mechanical properties was decrease at the diffusion layer comparing with that for the bulk.[5-20,21] From the knowledge, the *F-d* curve measurement was conducted to detect the quality of the interfacial diffusion layer on the various films.[5-22] Panel (a) of Fig. 5-7 shows the *F-d* curves acquired for the 13V and 13T in water. The zero position of the indentation depth was selected as the position where *F* started to increase. Also, the depth position where the *F* started to diverse was considered as the thickness of the diffused layer. In the both of the film surfaces, the *F* increased with increasing the indentation depth. However, the position where *F* started to diverge, was located relatively deeper region for the 13V than 13T. The same trends were also observed for the 9V and 9T as shown in panel (b) of Fig. 5-7. These results strongly suggested that the films annealed under water vapor condition was resulted in the formation of the thicker diffusion layer at water interface.

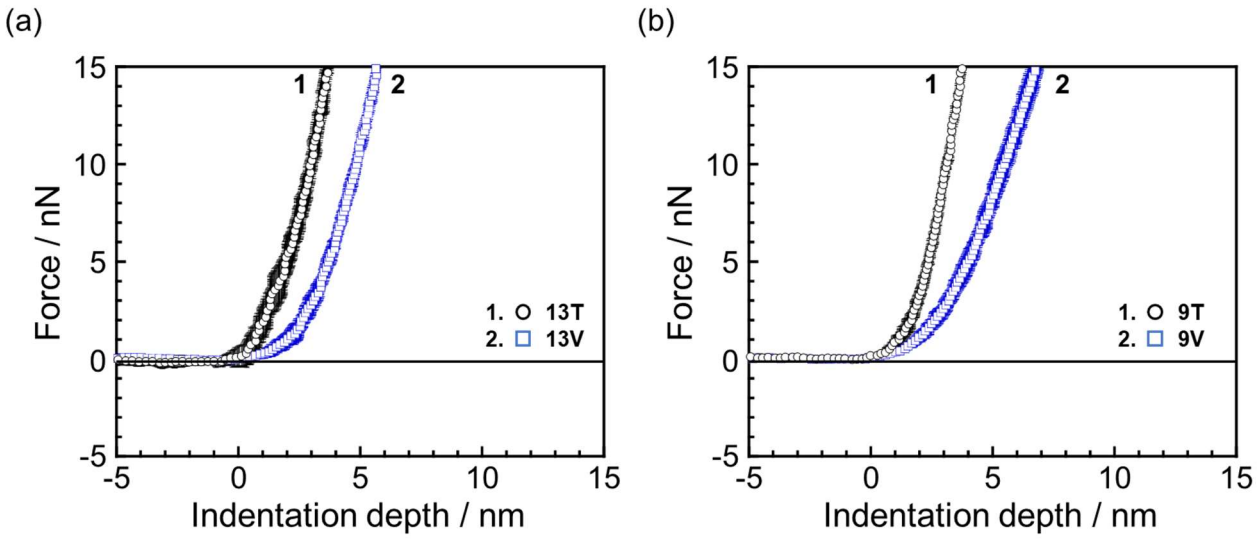

Fig. 5-7. *F-d* curve for the thin films of (a) PMMA-*b*-P[O(Ox)$_{13}$MA], and (b) PMMA-*b*-P[O(Ox)$_{9}$MA], which were thermal annealed under high vacuum or water vapor condition, evaluated by contact mode of AFM.

5.4. Summary

The purpose of this chapter is to increase the surface aggregation states and thereby to construct the developed diffusion layer at the water interface by annealing the thin films under water vapor conditions. To explore the effects of the annealing methods on surface aggregation states, the thin films thermal annealed under water vapor or high vacuum and the thin films sequentially annealed under the high vacuum and water vapor were prepared. Surface aggregation states of the thin film of PMMA-*b*-P[O(Ox)$_n$MA] under air were examined by using AFM, AD-XPS. Once the films were annealed under water vapor, the P[O(Ox)$_n$MA] block were preferentially segregate toward the near surface region, however, the extent of the segregation could be restricted by the quality of the PMMA wetting layer on the films. In addition, it was also confirmed that the films annealed under water vapor environment had more hydrophilic and diffused interfacial layer than the films annealed under high vacuum, in water. From this study, it became convinced that the surface aggregation states and formation of the diffused interfacial layer can be enhanced by the annealing methodology.

5.5. References

5-1) Stein, G. E.; Laws, T. S.; Verduzco, R. Tailoring the Attraction of Polymer toward Surfaces. *Macromolecules*, **2019**, *52*, 4787.

5-2) Ikada Y. Surface Modification of Polymers for Medical Applications. *Biomaterials*, **1994**, *15*, 725.

5-3) Tibbitt, M. W.; Rodell, C. B.; Burdick, J. A.; Anseth K. S. Progress in Material Design for Biomedical Applications. *Proc. Natl. Acad. Sci. USA*, **2015**, *112*, 14444.

5-4) Wei, Q.; Becherer, T.; Angioletti-Uberti, S.; Dzubiella, J. Wischke, C.; Neffe, A. T.; Lendlein, A.; Ballauff, M.; Haag, R. Protein Interactions with Polymer Coatings and Biomaterials. *Angew. Chem. Int. Ed.*, **2014**, *54*, 8004.

5-5) Bhatia, Q. S.; Pan, D. H.; Koberstein, J. T. Preferential Surface Adsorption in Miscible Bends of Polystyrene and Poly(vinyl methyl ether). *Macromolecules*, **1988**, *21*, 2166.

5-6) Matsuno, H.; Totani, M.; Yamamoto, A.; Haraguchi, M.; Ozawa, M.; Tanaka, K. Water-Induced Surface Reorganization of Bioscaffolds Composed of an Amphiphilic Hyperbranched Polymer. *Polym. J.*, **2019**, *51*, 1045.

5-7) Teng, C. Y.; Sheng, Y. J.; Tsao, H. K. Surface Segregation and Bulk Aggregation in an Athermal Thin Film of Polymer-Nanoparticle Blends: Strategies of Controlling Phase Behavior. *Langmuir*, **2017**, *33*, 2639.

5-8) Hester, J. F.; Banerjee, P.; Mayes, A. M. Preparation of Protein-Resistant Surfaces on Poly(vinylidene fluoride) Membranes via Surface Segregation. *Macromolecules*, **1999**, *32*, 1643.

5-9) Hong, J. H.; Totani, M.; Kawaguchi, D.; Masunaga, H.; Yamada, N. L.; Matsuno, H.; Tanaka, K. Design of a Bioinert Interface Using an Amphiphilic Block Copolymer Containing a Bottlebrush Unit of Oligo(oxazoline). *ACS Appl. Bio Mater.*, **2020**, *3*, 7363.

5-10) Ma, W.; Rajabzadeh, S.; Shaikh, A. R.; Kakihana, Y.; Sun, Y.; Matsuyama, H. Effect of Type of

Poly(ethylene glycol) (PEG) Based Amphiphilic Copolymer on Antifouling Properties of Copolymer/Poly(vinylidene fluoride) (PVDF) Blend Membranes. *J. Membr. Sci.*, **2016**, *514*, 429.

5-11) Irvine, D. J.; Griffith, L. G.; Mayas, A. M. Nanoscale Clustering of RGB Peptides at Surfaces Using Comb Polymers. 1. Synthesis and Characterization of Comb Thin Films. *Biomacromolecules*, **2001**, *2*, 85.

5-12) Guillen, G. R.; Pan, Y.; Li, M.; Hoek, E. M. V. Preparation and Characterization of Membranes Formed by Nonsolvent Induced Phase Separation: A Review. *Ind. Eng. Chem. Res.*, **2011**, *50*, 3798.

5-13) Wang, D. M.; Lai, J. Y. Recent Advances in Preparation and Morphology Control of Polymeric Membranes Formed by Nonsolvent Induced Phase Separation. *Curr. Opin. Chem. Eng.*, **2013**, *2*, 229.

5-14) Wang, H. H.; Jung, J. T.; Kim, J. F.; Kim, S.; Drioli, E.; Lee, Y. M. A Novel Green Solvent Alternative for Polymeric Membrane Preparation via Nonsolvent-Induced Phase Separation (NIPS). *J. Membr. Sci.*, **2019**, *574*, 44.

5-15) Chavis, M. A.; Smilgies, D. M.; Wiesner, U. B.; Ober, C. K. Widely Tunable Morphologies in Block Copolymer Thin Films Through Solvent Vapor Annealing Using Mixtures of Selective Solvents. *Adv. Funct. Mater.*, **2015**, *25*, 3075.

5-16) Yip, Y.; McHugh, A. J. Modeling and Simulation of Nonsolvent Vapor-Induced Phase Separation. *J. Membr. Sci.*, **2006**, *271*, 163.

5-17) Gu, X.; Gunkel, I.; Hexemer, A.; Gu, W.; Russel, T. P. An In Situ Grazing Incidence X-Ray Scattering Study of Block Copolymer Thin Films During Solvent Vapor Annealing. *Adv. Mater.*, **2014**, *26*, 273.

5-18) Atarashi, H.; Hirai, T.; Hori, K.; Hino, M.; Morita, H.; Serizawa, T.; Tanaka, K. Uptake of Water in As-Spun Poly(methyl methacrylate) Thin Films. *RSC Adv.*, **2013**, *3*, 3516.

5-19) Greenspan, L. Humidity Fixed Points of Binary Saturated Aqueous Solutions. *J. Res. Natl. Bur.*

Stand. Sect. A, **1977**, *81*, 89.

5-20) Itagaki, N.; Oda, Y.; Hirata, T.; Nguyen, H. K.; Kawaguchi, D.; Matsuno, H.; Tanaka, K. Surface Characterization and Platelet Adhesion on Thin Hydrogel Films of Poly(vinyl ether). *Langmuir*, **2017**, *33*, 14332.

5-21) Tanaka, K.; Fujii, Y.; Atarashi, H.; Akabori, K.; Hino, M.; Nagamura, T. Nonsolvents Cause Swelling at the Interface with Poly(methyl methacrylate) Films. *Langmuir*, **2008**, *24*, 296.

5-22) Oda, Y. Construction of hydrophilic surface with poly(vinyl ether)s and their interfacial properties in water. *Polym. J.*, **2019**, *51*, 955.

Chapter 6. Conclusions

6.1. Summary of this study

The purpose of this study is to understand aggregation states of PEtOx at the water interface on a basis of polymeric structure and processing, and then, to evaluate the effects of interfacial aggregation states on its physical properties and the bio-inert functionality.

For the purpose;

In chapter 1, the background knowledge of these studies were summarized; polymer biomaterials, surface aggregation behavior of polymers and its contribution factors, and relationship between the surface aggregation states, physical properties and bio-inert properties.

In chapter 2, well-defined amphiphilic type PEtOx derivatives are planned to be synthesized. Because PEtOx is soluble in water, the end group functionalized PEtOx subsequently connected to PMMA segments, which is water insoluble polymer structure. As a synthetic strategy to obtain the amphiphilic block copolymer, O(Ox)$_n$MA macromonomers having different *n* were synthesized by LCROP. Subsequently, a series of well-defined PMMA-*b*-P[O(Ox)$_n$MA] were successfully polymerized by ATRP using the O(Ox)$_n$MA macromonomer and PMMA macroinitiator. Also, bottlebrush P[O(Ox)$_n$MA] homopolymers were also polymerized in a similar manner.

In chapter 3, as a first step to establish why PEtOx shows outstanding bio-inert properties, well-defined PEtOx/water interface was aimed to be formed. Thin film of amphiphilic PMMA-*b*-P[O(Ox)MA], which was stable in water, was prepared on solid substrates by spin-coating and following thermal annealing at (T_g+20) K for 12 h. In addition, aggregation states on the thin film was evaluated by using AFM, contact angle, AD-XPS, and NR measurements. After the film preparation, the film surface was covered by around 5 nm of PMMA wetting layer. However, once the film was

immersed in water, the P[O(Ox)MA] successfully segregated toward water interface, and then formed P[O(Ox)MA]-rich layer at the water interface. Then, it was also confirmed that the P[O(Ox)MA]/water interfacial layer was well diffused. Subsequently, the diffused interfacial layer strongly restricted the NIH3T3 cell and FBS protein adhesion behavior.

In chapter 4, to explore bottlebrush structural effects on surface aggregation states, bottlebrush P[O(Ox)$_n$MA]s, having different oligometric side chain length, were applied to the PMMA films to estimate segregation behavior of P[O(Ox)$_n$MA]s. At first, in the mixture film after thermal annealing at 423 K, both P[O(Ox)$_n$MA] aggregated interior of the bulk region of the mixture films. However, after the mixture films contacted with water, both P[O(Ox)$_n$MA] were migrated toward water interface. Especially, P[O(Ox)$_7$MA], which have relatively short oxazoline side chains, strongly aggregated and successfully formed the thicker diffusion layer at the mixture film/water interface. Subsequently, the P[O(Ox)$_7$MA]/water interfacial layer shows most enhanced bio-inert properties. The results strongly suggested that the extent of the surface aggregation states and the diffused interfacial layer was tuned by architecture of P[O(Ox)$_n$MA]. In addition, it also showed that the bio-inert properties were significantly improved at the water interface where the thicker diffusion layer with the high density of P[O(Ox)$_n$MA] was formed near the water phase.

In chapter 5, to examine the effect of annealing methods on surface aggregation states and formation of the interfacial diffusion layer, the various annealing methods, which were conducted under water vapor or under vacuum or combination of them, was applied to the thin films of the PMMA-*b*-P[O(Ox)$_n$MA]s. When the as cast films were annealed under water vapor, the P[O(Ox)$_n$MA] block well dispersed on the film. However, if the films were once thermal annealed under high vacuum condition, the P[O(Ox)$_n$MA] block was hided interior bulk region, that is, PMMA wetting layers were formed. After that, when thermal annealing was performed under water vapor condition again, it was confirmed that the P[O(Ox)$_n$MA] block tends to segregated toward the surface, however, the extent of the segregation was suppressed with increasing the quality of the PMMA wetting layer. In addition, it

was also confirmed that the films annealed under water vapor formed more hydrophilic and diffused interfacial layer in water.

6.2. Prospective of this study

In this study, I prepared stable and homogeneous PEtOx/water interface on a basis of the segregation. To control the extent of surface aggregation states and the following formation of the PEtOx/water interface, the effects of PEtOx architecture, annealing process in the polymer alloys on the aggregation states were explored. As the results, it was confirmed that the aggregation states and its physical properties successfully tuned by the effects. Also, the increasing aggregation states of the PEtOx at the outermost surface leaded to form diffused and soft layer at the water interface, and the interface shows enhanced bioinert properties. These results in this study convince us that this simple surface modification method based on segregation will contribute to the development of an increasing number biomedical devices requiring bioinert functionalization.

Acknowledgement

First of all, I would like to express my special gratitude to Professor Keiji Tanaka (Department of Applied Chemistry, Kyushu University) for the consistent supports for carrying out the studies in the past 3 years.

I would like to appreciate to Professor Atsushi Takahara (Institute for Materials Chemistry and Engineering, Kyushu University) and Professor Masaru Tanaka (Institute for Materials Chemistry and Engineering, Kyushu University) for giving valuable advices to complete this graduation thesis.

I would like to express my thanks to Associate Professor Hisao Matsuno (Department of Applied Chemistry, Kyushu University) for giving many of continuous guidance and advices to conduct all of the experiments.

Likewise, I would like to appreciate to Associate Professor Daisuke Kawaguchi (Department of Applied Chemistry, Kyushu University) and Research Assistant Professor Masayasu Totani (Department of Applied Chemistry, Kyushu University) for providing continuous assistance for many experiments and data analysis.

Also, I would like to appreciate to Professor Satoru Yamamoto (Center for Polymer Interface and Molecular Adhesion Science, Kyushu University), Associate Professor Atsuomi Shundo (Department of Automotive Science, Kyushu University), Assistant Professor Yukari Oda (Department of Applied Chemistry, Kyushu University), Doctor Aoki, Doctor Yuma Morimitsu, and Doctor Nguyen Kim Hung for giving helpful comments and interests in my studies.

I would like to express my thanks to Doctor Hiroyasu Masunaga (Japan Synchrotron Radiation Research Institute) for the support to conduct the small-angle X-ray scattering (SAXS) measurement at the BL03XU in SPring-8 (Hyogo, Japan), thanks to Assistant Professor Norifumi L. Yamada (High Energy Accelerator Research Organization) for the supports to measure and analyze the neutron reflectivity (NR) at the Materials and Life Science Experimental Facility (MLF), Japan Proton

Accelerator Research Complex (J-PARC, Ibaraki), and also thanks to Doctor Takashi Yamamoto (Tokyo Instruments, Incorporated), Doctor Samir Manmadov (SPECS Surface Nano Analysis GmbH), and Doctor Andreas Thissen (SPECS Surface Nano Analysis GmbH) for the supports to measure the near ambient pressure X-ray photoelectron spectroscopy (NAP-XPS).

Finally, I would like to appreciate to Ms. Minami Yamaguchi and all the students of Tanaka Laboratory for helping me a lot regarding not only for experiments but for the school lives.